Joule

CellPress

Review

Review of modification strategies in emerging inorganic solid-state electrolytes for lithium, sodium, and potassium batteries

Xuyong Feng,[1,4] Hong Fang,[2,4] Nan Wu,[1] Pengcheng Liu,[1] Puru Jena,[2] Jagjit Nanda,[3,*] and David Mitlin[1,*]

SUMMARY

The design of solid-state electrolyte (SSE) entails controlling not only its bulk structure but also the internal (e.g., grain boundary and pore) and heterophase (e.g., anode-SSE reaction layer) interfaces. Moreover, defects are integral for establishing both the initial all-solid-state battery (ASSB) cell performance and its ultimate cycling lifetime. This topical review discusses 5 highly promising inorganic lithium-, sodium-, and potassium-based SSEs, providing case studies of strategies to enhance ionic conductivity, tune the internal and heterophase interfaces, and prevent dendrites and deleterious side reactions. The primary focus is on garnet LLZO ($Li_7La_3Zr_2O_{12}$), argyrodite (Li_6AS_5X, A = P, Sb and X = Cl, Br, I), Na_3AB_4 (A = P, Sb, As and B = S, Se), and NASICON-type electrolytes, with several exploratory potassium systems being presented as well. The article begins with a discussion of the superionic conduction mechanisms, which is assisted by defects, topology, correlation, and disorder. The discussion then shifts to the thermodynamic or kinetic phase stability of metastable SSEs, followed by the SSE internal interfaces (pores and grain boundaries), and finally the complex microstructure associated with the reactive boundaries between the SSE and the metal anode and the SSE and the high-voltage ceramic cathode. This review explores why SSE systems with highly promising bulk ionic conductivity values do not demonstrate comparable performance in full cells. A major cause is the cycling-induced formation of ionically insulating but electrically conducting new phases at both the anode and the cathode. For the SSEs that do not rapidly decompose when contacting the anode, site-specific variations in ionic conductivity/electrical resistivity lead to growth of metal dendrites. In each electrolyte class, creative fabrication strategies have been employed to minimize, but not fully eliminate, new phase formation and dendrites, creating ample opportunities for additional analytical and synthesis-focused research. The emphasis of the discussion is on the bulk doping strategies for SSEs, emerging simulation and characterization findings in relation to SSE performance and cell failure, and new synthesis approaches and cell architectures to improve cycling stability. Throughout the article, outstanding scientific questions are identified, and future research directions are proposed.

Context & scale

One of the greatest challenges facing humanity is climate change, which is brought about mainly by the increasing amount of CO_2 in the Earth's atmosphere. To mitigate this problem, the world must transit from fossil fuels to clean, renewable, and sustainable energy sources. This also requires finding efficient and cost-effective means of storing energy. Batteries are an integral part of clean and sustainable energy solution to meet the global mandate for net carbon zero economy by 2050 and the United States' goal for reducing greenhouse gas emission by 50% by 2030. General Motor's declaration to convert all its vehicles to electric mode by 2035 further underscores this challenge. Lithium-ion batteries (LIBs) have undoubtedly brought one of the greatest benefits to mankind by enabling the development of miniaturized and portable electronics and opening the gateway toward a fossil-fuel-free economy. Significant strides have been achieved in the past 2 decades in the development of LIBs with reduced cost and increased energy density to address the growing demands for electrochemical energy storage. Most recently, sodium- and potassium-ion batteries (SIBs and KIBs) have also attracted great

MOTIVATION FOR SOLID-STATE BATTERIES (SSBs)

In the past two decades, lithium-ion batteries (LIBs) have made significant strides in reducing cost, increasing energy density, and ramping up global production to address the growing demands for electrochemical energy storage.[1,2] For example, the cost at the Li-ion pack level has come down from approximately $1,000 per kWh in 2009 to $180 per kWh in 2020, with a concomitant increase in gravimetric energy from 125 Wh/kg to 250 Wh/kg.[3,4] Although the specific energy of LIBs has grown incrementally at 7% per year, the recurring safety concerns associated with the liquid organic-based electrolytes have remained and even intensified with the application of higher-voltage higher-capacity cathodes.[5,6] The next-generation "beyond lithium" electrochemical energy storage technologies should provide greater specific and volumetric energy, power, as well as long-term cyclability. Reducing the cost of the battery systems is a key enabler for a much wider application of renewable energy conversion based on solar and wind energies.[2,7–9] Optimizing the performance and improving the safety can bolster greater consumer confidence in batteries.[3,10–12] In addition, the ideal storage systems should have the flexibility to provide energy and power on demand, be scalable, and preferably based on earth-abundant materials to counter the supply chain and other market constraints.[13]

Lithium metal-based batteries (LMBs) employ a Li metal anode coupled with a conventional high-voltage ceramic or low-voltage sulfur-based cathode. The configuration can achieve cell-level specific energies exceeding 500 Wh/kg,[14] potentially nearly doubling the range of electric vehicles (EVs) on a single charge.[15,16] However, the use of the reactive Li metal anode, versus a conventional ion-insertion anode based on graphite, creates substantial issues in battery safety and longevity. Hence, there is a persistent effort in the research community to develop safe LMBs and, more recently, sodium metal batteries (SMBs) and potassium metal batteries (KMBs).[17–20] The specific capacities of Li, Na, and K metal anodes are 3,861, 1,165, and 678 mAh/g, all far surpassing the capacity of graphite with Li at 372 mAh/g and of carbon with K and Na at 250–350 mAh/g.[3–6] The higher capacity combined with wider voltage window results in over 50% increase in the gravimetric energy versus conventional ion-insertion anodes. For example, a key state-of-the-art LMB architecture is based on a high-voltage 811 $LiNi_{0.8}Co_{0.1}Mn_{0.1}O_2$ (NMC) cathode with an energy surpassing 500 Wh/kg.[3] However, due to the safety concerns of combining a metal anode with a flammable liquid electrolyte, all commercial LMBs remain to be based on the far less energetic graphite or Si-carbon nanocomposites.[21–24] Likewise, the emerging room temperature sodium- and potassium-based secondary batteries employ carbon-based anodes instead.

Achieving long-term stable and safe metal anode plating/stripping performance remains a key impediment for successful metal batteries, with conventional liquid organic electrolytes remaining out of reach due to their reactivity with the metal anode and the associated lifetime and safety concerns.[25,26] Employing solid-state electrolytes (SSEs) rather than liquid organic electrolytes is a possible path toward greater battery safety since most inorganic SSEs are non-flammable.[27,28] Recently, there has been significant progress related to a number of successful solid-state battery chemistries showing reasonable cycle life and capacity retention using traditional LMB cathodes and metal anodes.[29,30] The success of this technology hinges on developing practical superionic conducting SSEs with robust electrochemical stability within the voltage window of an operating cell.[31–35]The future of solid-state batteries is not limited to Li metal batteries only.[36–45] The progress in Na and K metal anodes and related solid-state ionic conductors[46–48] provide a potential path for safe SMBs and, possibly, KMBs. However, SSEs still have the propensity to develop

attention due to their high abundance and uniform distribution in the earth's crust. Although LIBs, SIBs, and KIBs represent a key part for the future of battery technologies, there are still many challenges in their development. These include the large volume change of the host material during insertion/extraction of the metal-ions, low ionic diffusivity in solid electrodes, and side reactions leading to the consumption of electrolytes and dendrite growth. Developing practical ion-conducting solid-state electrolytes (SSEs) with robust electrochemical stability against Li/Na/K metal anodes is the key to meet these challenges and to overcome the energy density gap.

In this review, we focus on the most promising SSEs emerging from the recent research in the field. We cover their ion-conduction mechanisms, experimental synthesis, microstructure optimizations, and, especially, their interfacial properties with electrodes. This review can serve as a useful introduction to the hot topics on SSEs and their successful implementation into battery systems.

[1]Materials Science and Engineering Program & Texas Materials Institute (TMI), The University of Texas at Austin, Austin, TX 78712-1591, USA

[2]Department of Physics, Virginia Commonwealth University, Richmond, VA 23284, USA

[3]Chemical Sciences Division, Oak Ridge National Laboratory, Oak Ridge, TN 37830, USA

[4]These authors contributed equally

*Correspondence: nandaj@ornl.gov (J.N.), david.mitlin@austin.utexas.edu (D.M.)

https://doi.org/10.1016/j.joule.2022.01.015

unstable interfaces with both the anode and at the cathode, [25,26,28] in some cases, with a greater severity than that for organic electrolytes.[49] Although inorganic SSE's will not ignite under normal operating conditions, the systems based on sulfur and selenium can release H_2S and H_2Se when exposed to moisture, leading to safety concerns.[50–53]

This review should serve as useful tutorial not only for people entering but also for those who are already active in the field and looking for promising microstructure-related research directions on "hot" SSEs topics. We focus on a few of the most promising SSE systems (Garnet $Li_7La_3Zr_2O_{12}$, Li-argyrodite, Na_3AB_4, and NASICON) that have commercial possibility in larger format cells based on their bulk ionic conductivity values. These SSE systems include typical oxides and sulfides for both Li and Na, which are involved in most fundamental researches about Li/Na all-solid-state batteries (ASSBs). The discussion and summary about these SSEs would help understand the main issues in most of the ASSBs. General experimental and theoretical considerations and approaches toward SSEs are introduced along with useful case studies. There are numerous solid-state ionic conductors,[54–76] for example, lithium phosphorus oxynitrides (LiPON), which are straightforward deposit and relatively inexpensive.[77] However, because of the low ionic conductivity, these systems are not suitable for large battery systems in automotive applications.[26] Such ionic conductors have been widely covered in previous reviews[8,32–34,78–92] and, therefore, will not be discussed here. This review does not appreciably discuss mechano-electrochemical effects as related to large format cells and ultimately to commercial-scale systems. Mechano-electrochemical effects have been an explicit focus of an excellent recent (2021) perspective review article by Dasgupta, Sakamoto, and co-workers.[93] Readers are urged to consult it for unique insights regarding the role of stress and fracture in establishing the ultimate feasibility of automotive SSE-based batteries. For garnet $Li_7La_3Zr_2O_{12}$, Guo and co-workers have recently (2020) given an overview of the current progress, especially on how to improve ionic conductivity and build high-performance all-solid-state batteries.[94] Sun et al. summarized the recent (2021) progress on Li-argyrodites regarding the synthesis, chemical structures, lithium-ion transport mechanism, strategies to improve ionic conductivity, and chemical and electrochemical stabilities toward cathode and anode.[95] More details about garnet $Li_7La_3Zr_2O_{12}$ and Li-argyrodites can be found in these reviews.

OVERVIEW OF SUPERIONIC CONDUCTORS

Ionic diffusion in superionic conductors

Superionic conductors (fast-ion conductors) or SSEs are solids containing some ions with extraordinary mobility, allowing them to hop between crystallographic sites and even act like fluid phase in a crystalline matrix formed by the other ions.[91,96,97] The classical picture of the ion transport in crystal states is depicted in Figure 1A, where a mobile ion jumps from one site to another.[8] The basic hopping patterns include: (1) The ion migrates from one site to a neighboring vacant site; (2) The ion migrates via an interstitial site between occupied sites; (3) The ion migrates to a neighboring vacant site closely followed by the occupation of its site by another neighboring ion.[8] Composed by these individual hopping steps, the transport of a collection of mobile ions can be measured by the "area" they explore in the structure within certain amount of time at a specified temperature.[98] This characteristic "area" is defined by the so-called mean squared displacement (MSD), which is connected to the ionic diffusivity (D) according to

$$D = \lim_{t\to\infty} \frac{1}{2dt} \frac{1}{N} \sum_{i=1}^{N} \langle [\boldsymbol{r}_i(t) - \boldsymbol{r}_i(0)]^2 \rangle, \qquad \text{(Equation 1)}$$

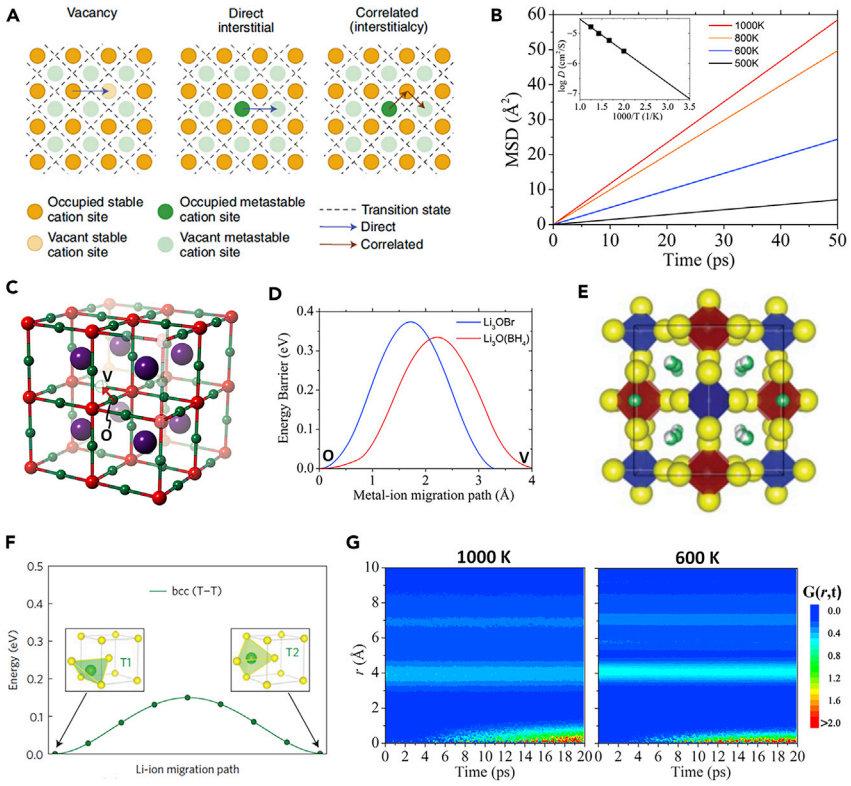

Figure 1. Demonstration of the fast-ion conduction mechanisms

(A) A classical picture of basic hopping modes in ionic conductors. Reprinted from Famprikis et al.,[8] with permission. Copyright 2019, Nature Publishing Group.

(B) Calculated linear mean squared displacement (MSD) at four different temperatures for a lithium argyrodite. The inset shows the computed diffusivities from the MSD by Equation 1 at the corresponding temperatures and fitted by the Arrhenius relationship in Equation 2.

(C) Metal-vacancy-assisted ion migration in alkali antiperovskite superionic conductors, A_3HO (A = Alkali; H = halogen), where the alkali-ion (in green) at an occupied (O) site migrates to its neighboring vacancy (V) site (open sphere) along the edge of the A_6O octahedron centered by oxygen (in red).

(D) Calculated energy barriers corresponding to the type of migration in (C) for two typical lithium antiperovskite superionic conductors, Li_3OCl and $Li_3O(BH_4)$. Due to the orientational disorder of the polyanion BH_4 in $Li_3O(BH_4)$, it exhibits reduced migration barrier compared with that of Li_3OCl.

(E) The crystal structure of $Li_{10}GeP_2S_{12}$. Sulfur atoms are in yellow, fully occupied lithium in green, partially occupied lithium in green-white, $(Ge_{0.5}P_{0.5})S_4$ tetrahedra in red, and PS_4 tetrahedra in blue. Reprinted from Ong et al.,[99] with permission. Copyright 2013, The Royal Society of Chemistry.

(F) The Li-ion (in green) migration pathway in a body-centered cubic sublattice of sulfur (in yellow) found in $Li_{10}GeP_2S_{12}$. Reprinted from Wang et al.[31] with permission. Copyright 2015, Nature Publishing Group.

(G) Calculated van Hove correlation functions, as in Equation 5, for a sodium antiperovskite superionic conductor at two different simulation temperatures. Compared with the conspicuous stripes at 600 K, the broadened and relatively fuzzy stripes at 1,000 K are due to severe thermal disturbances on the correlational motion of Na-ions. (B) (C), (D), and (G): F.H., N.J., and D.M., unpublished data.

where $[\boldsymbol{r}_i(t) - \boldsymbol{r}_i(0)]$ is the displacement vector of the mobile ion at time t.

Figure 1B shows the calculated linear Li-ion MSD in a lithium argyrodite SSE (which will be discussed in the following section) at different temperatures. Clearly, according to Equation 1, the Li-ion diffusivity measured by the slope of the MSD increases with elevated temperature. It is found that diffusivity versus temperature follows the Arrhenius relationship,

$$D = A\,exp(-E_a / k_B T) \quad \text{(Equation 2)}$$

which is routinely used to fit to the diffusivity data points at a few temperatures to extrapolate the diffusivities at other temperatures, as shown by the inset in Figure 1B. Both the pre-factor A and an energy term E_a, called the activation energy, are treated as the fitting parameters. Because the ionic transport is a collective thermally excited phenomenon, Equation 2 is featured by a Boltzmann factor seen in statistical physics, and E_a serves as a characteristic energy to measure the ease with which ions can hop in a system. The ionic conductivity of the ionic conductor can then be obtained from the Nernst-Einstein relation

$$\sigma = D\left(Ne^2 / k_B T\right) \quad \text{(Equation 3)}$$

where N is the number of the mobile ions per cm^3. Other symbols have their customary meanings.

Several ionic conduction mechanisms have been found in the known Li/Na/K SSEs. The first is defect- (e.g., vacancy, interstitial, etc.) assisted conduction. This is exemplified by the alkali antiperovskite superionic conductors[100] A_3HO (A = Alkali; H = halogen) whose fast-ion diffusions disappear in perfect lattice.[101] As shown in Figure 1C, ionic transport in these materials involves the direct hopping of the alkali-ion to its neighboring vacant site along the A_6O octahedral edges in the structure. The energy barrier for such hopping, as shown in Figure 1D, corresponds to the activation energy of the material.

The second type of ionic conduction is topology-assisted diffusion. This is exemplified by the lithium sulfide $Li_{10}GeP_2S_{12}$, as shown in Figure 1E, which exhibits a very high room temperature ionic conductivity of 12 mS/cm.[99] It is found that $Li_{10}GeP_2S_{12}$ is featured by a body-centered cubic sublattice of sulfur, allowing the tetrahedrally coordinated Li-ion by sulfur to hop between the neighboring sites via a large transport channel,[31] as shown in Figure 1F. On the other hand, lithium sulfide with a face-centered cubic (fcc) or hexagonal closed packed (hcp) sulfur sublattice exhibits a much lower ionic conductivity.[31] Other examples include the mixed-anion antiperovskites, such as $Li_3OCl_{0.5}Br_{0.5}$[100] and $Na_3SCl_{0.5}(BCl_4)_{0.5}$.[102] Due to the different sizes between the halogens (Cl versus Br) or the halogen and big polyanion (Cl versus BCl_4), the accommodation of the bigger anion in the lattice creates additional channel space around the smaller anion for metal-ions to transport, thus enhancing the ionic conductivity of the material.[102]

The third type of ionic conduction is correlated collective motion of the metal-ions. If there is strong interaction between the neighboring metal-ions, such as found in $Li_{10}GeP_2S_{12}$ (LGPS), cubic $Li_7La_3Zr_2O_{12}$ (LLZO), and $Li_{1.3}Al_{0.3}Ti_{1.7}(PO_4)_3$ (LATP),[103] multiple meta-ions would migrate collectively, effectively flattening the energy barrier. One way to measure the correlated motion is to calculate the diffusion (D_c) of the charge center of all the metal-ions in Equation 4 against the diffusion (D) of individual metal-ions in Equation 1:

$$D_c = \lim_{t\to\infty} \frac{1}{2dt} \left\langle \left[\frac{1}{N}\sum_{i=1}^{N} \boldsymbol{r}_i(t) - \frac{1}{N}\sum_{i=1}^{N} \boldsymbol{r}_i(0) \right]^2 \right\rangle. \quad \text{(Equation 4)}$$

The Haven ratio is defined as $D/(ND_c)$, and its inverse, called the correlation factor, measures the average number of metal-ions moving together in the system. The way to quantitatively evaluate the collective modes is to study the distinct van Hove time correlation function defined as

$$G_d(\mathbf{r},t) = \frac{1}{N}\left\langle \sum_{i\neq j}^{N} \delta\left[\mathbf{r} + \mathbf{r}_j(0) - \mathbf{r}_i(t)\right]\right\rangle \quad \text{(Equation 5)}$$

which measures the probability of finding, at time t, another ion at distance $\mathbf{r}_i$ given the fact that the first ion at $\mathbf{r}_j$ at $t = 0$. $G_d(\mathbf{r}, t = 0)$ is the pair distribution function of the structure. $G_d(\mathbf{r} = 0, t)$ measures the probability of one ion being replaced by another in time t. An example of the calculated van Hove time correlation function for a sodium antiperovskite superionic conductor is given in Figure 1G, where significant values of G_d are found at $\mathbf{r} = 0$ and around 4 Å. The former suggests that one Na-ion will quickly fill the vacant site left by another in a timescale of 1 ps. The latter suggests that the neighboring Na-ions (with distances in 3.5–4.5 Å) are likely to move together in the system. There is also some correlational motion between the Na-ion and its second nearest neighbors, as indicated by the narrow stripe around 7 Å in G_d.

The fourth type of ionic conduction is disorder-assisted migration, such as phase amorphization, anion disorder, and orientational disorder of polyanions. It is found that promoting amorphous phases in some materials (e.g., Li_3PS_4) may lead to a degenerate ground state for the Li sublattice so that the Li ions can rearrange into different sites with relatively low energy cost.[104] Different anion species with similar ionic radii swapping their sites can also reduce the activation energy and enhance the ionic conductivity of a material, as found in alkali antiperovskite and argyrodite conductors. Other examples include the SSEs containing polyanions, such as BF_4^-, $B_{12}H_{12}^{2-}$, and PS_4^{3-} in Li_3SBF_4, $Li_2B_{12}H_{12}$, and Li_3PS_4, respectively. Upon thermal excitation, the polyanions can form an orientationally disordered rotor phase, which can create a number of energetically frustrated sites for metal-ions to explore, resulting in a reduced activation energy (as demonstrated in Figure 1D with $Li_3O(BH_4)$ versus Li_3OCl) and enhanced ionic conductivity of the material.[105–107]

Phase transitions in super ionic conductors

There is a wide range of solids with superionic phases, including the one as simple as AgI. However, most of the fast-ion conducting phases only exist at high temperatures, and the challenge is to discover or tailor the chemical compositions that provide superionic conduction at ambient conditions.[108] For practical solid-state battery applications, SSEs should have a room temperature ionic conductivity over 1 mS/cm and activation energy below 0.4 eV.[109] However, only a few classes of lithium conductors can satisfy the above criteria , and these are all metastable in their ground states due to the relatively weak interactions between the metal-ions and the anions in the system. Therefore, to access good Li/Na/K ionic conductor phases and enhance their properties under ambient conditions, techniques that can modify the thermodynamic or kinetic phase stability are important.

Heteroatom doping represents a path toward achieving modified thermodynamics, as long as the dopants are retained in their targeted occupancy sites. Consider the standard free energy relation: $\Delta G = \Delta H - T\Delta S$, where G is Gibbs free energy, H is the enthalpy, and S is the entropy. Therefore, it may be observed that at elevated temperatures, the entropy contribution due to various defects becomes important. Entropy will be increased with the introduction of heteroatoms into the lattice due to the corresponding vacancies generated by aliovalent substitutions. For aliovalent atom doping, the associated extra vacancies or interstitial ions would further increase the entropy. In addition, heteroatom doping will affect the lattice and the energy of the elevated-temperature structure. For crystals, the lattice energy is defined as the change in the energy of the system of atoms and molecules when a crystal is

Table 1. Summary of representative Li and Na superionic conductors with different structures and their transition temperature

Chemistry	Transition temperature (°C)	Low-temperature structure	High-temperature structure	Doping strategy
Li_7PS_6	210[115]	$Pna2_1$ (orthorhombic) a = 14.076 Å b = 6.917 c = 9.955[115]	$F\bar{4}3m$ (cubic) a = 9.9926 Å (230°C)[115]	Li_6PS_5X (X = Cl, Br, I)[116] $Li_{7.35}Si_{0.35}P_{0.65}S_6$[117] $Li_{7.3}Si_{0.3}P_{0.7}S_6$[117]
$Na_3Zr_2Si_2PO_{12}$	147[118]	C2/c (monoclinic) a = 15.586 b = 9.029 c = 9,209 β = 123.7°[124]	$R\bar{3}c$ (rhombohedral) a = 9.029 c = 22.974 (247°C)[124]	$Na_{3.4}Zr_2Si_{2.4}P_{0.6}O_{12}$[119] $NaZr_2P_3O_{12}$[120] $Na_{3.2}Y_{0.2}Zr_{1.8}Si_2PO_{12}$ (139.5°C)[121]
$LiBH_4$	110[122]	Pnma (orthorhombic) a = 7.141 b = 4.431 c = 6.748 (−48°C)[123]	$P6_3mc$ (hexagonal) a = 4.323 Å c = 7.037 Å (262°C)[123]	$3LiBH_4 \cdot LiCl$ (≈72°C)[122] $3LiBH_4 \cdot LiBr$ (≈68°C)[122] $3LiBH_4 \cdot LiI$[122]
Na_3PS_4	260[124]	$P\bar{4}2_1c$ (tetragonal) a = 6.952 c = 7.076[124]	$I\bar{4}3m$ (cubic) a = 7.070 Å (327°C)[125]	Na_3SbS_4 (100–120°C)[126] Na_3PSe_4[127]
Na_3PS_4	510[114]	$I\bar{4}3m$ (cubic) a = 7.070 (327°C)[125]	Fddd (orthorhombic) a = 6.606 Å b = 11.714 Å c = 20.738 Å (550°C)[114]	–
Li_2OHCl	60[128]	P4mm (tetragonal) a = 3.913 c = 3.919 (40°C)[128]	Pm3m (cubic) a = 3.917 Å (60°C)[128]	Li_3OCl[100] Li_3OBr[100]
$Li_7La_3Zr_2O_{12}$	177[129]	$I4_1/acd$ (tetragonal) a = 13.134 c = 12.663[130]	$Ia\bar{3}d$ (cubic) a = 13.03 Å (247°C)[129]	$Li_{6.75}La_3Zr_{1.75}Ta_{0.25}O_{12}$[129] $Li_{7-3x}Al_xLa_3Zr_2O_{12}$[131]
$Li_{10}GeP_2S_{12}$	100[135]	$P4_2/nmc$ (tetragonal) a = 8.718 c = 12.635[132]	$P4_2/nmc$ (tetragonal) (–)	–

formed from the free ionic forms of the components in the gas phase.[110] A change in valence and lattice parameters would affect the lattice energy, with larger-sized heteroatoms stabilizing the elevated-temperature phases. Conversely, heteroatom doping may further promote the instability of the elevated-temperature phase at lower temperatures.[111] Therefore, choosing appropriate doping ions and doping amount is a complex undertaking, requiring extensive experimental verification and guidance from theoretical simulation.

It is found that many superionic conductor phases are defect-enriched and/or possess ion disordering on the lattice sites. A defect-enriched structure is a key feature of $Li_{10}GeP_2S_{12}$ and $Li_{1+x}Al_xTi_{2-x}P_3O_{12}$ systems[99,112] and in cubic Na_3PS_4.[46,51] However, the generation of defects/disorder requires extra energy. Due to entropy consideration, the more disordered structure can be thermodynamically stable at only relatively high temperature. Although the stability at ambient temperature can be kinetic retained, the energetic preference is for these structures to decompose to other more stable-lower entropy structures. For example, the simulated phase stability of $Li_{10}GeP_2S_{12}$ shows that $Li_{10}GeP_2S_{12}$ will decompose to more stable Li_4GeS_4 and Li_3PS_4 at low temperatures.[99,113,114] Table 1 summarizes the structures of several representative Li- and Na-based superionic conductors and the associated structure transition temperatures. It may be observed that most of these "special" structures will transform into another more thermodynamically stable but less conductive structure at low temperatures. Therefore, it is easier to find fast-ion conducting structures at elevated temperatures. The challenge is then to stabilize the elevated-temperature structure at room temperature or even lower to retain the necessary ionic conductivity. For most achieved metastable superionic conductors, the phase transition temperature does not significantly exceed room temperature (e.g., 473 versus 300 K). Otherwise, there is too much of a driving force for decomposition, and the metastable phase does not survive.

There are several ways to fabricate metastable superionic conductors, in the process tuning the thermodynamic stability or extending the kinetic stability.[133] For example, nanostructuring increases the surface energy and thus the total free energy

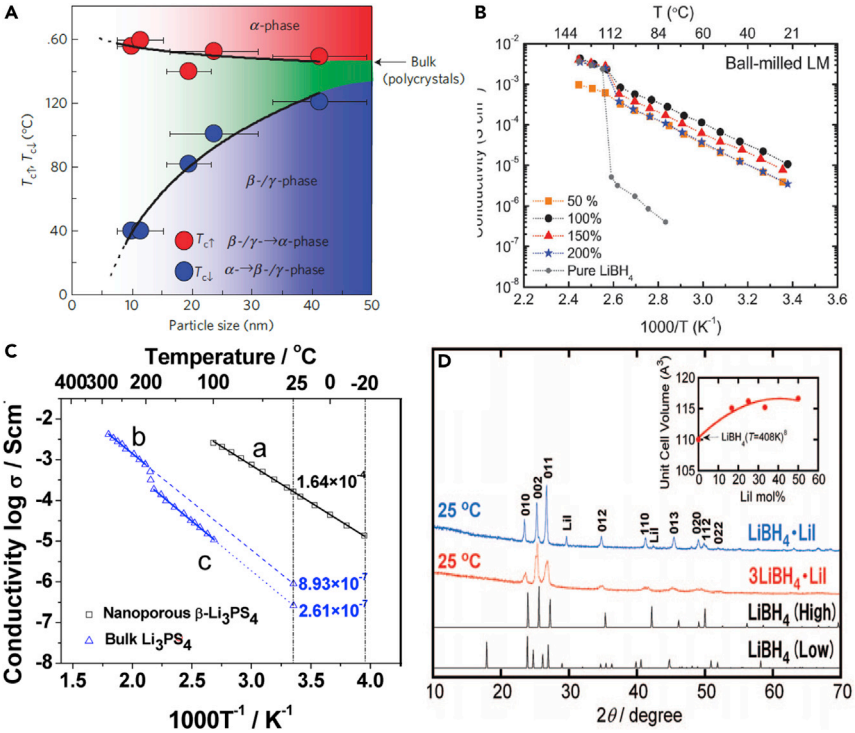

Figure 2. Phase transitions in superionic conductors

(A) Evolution of the phase transition temperature T_c with nanoparticle size. Reprinted from Makiura et al.[134] with permission. Copyright 2009, Nature Publishing Group.

(B) Arrhenius plots of the ionic conductivities of ball-milled $LiBH_4$-SiO_2 composites in different mixing ratios. Reprinted from Choi et al.[138] with permission. Copyright 2016, The Royal Society of Chemistry.

(C) Arrhenius plots for ionic conductivity of nanoporous β-Li_3PS_4 (line a), bulk β-Li_3PS_4 (line b), and bulk γ-Li_3PS_4 (line c), reprinted from Liu et al.[137] with permission. Copyright 2013, American Chemical Society.

(D) Indexed X-ray diffraction pattern of $LiBH_4$-LiI at 25°C, with the inset showing the change in unit cell volume as a function of mole fraction of LiI. Reprinted from Maekawa et al.[122] with permission. Copyright 2009, American Chemical Society.

of the material, opening the possibility of having the nanostructured elevated-temperature phase remain stable at ambient temperature.[134] In principle, as long as the nanoscale crystalline size is preserved, the disordered structure remains thermodynamically favored. This effect is lost if microstructural coarsening occurs during cycling or storage, which in itself is a thermodynamically favored phenomenon. Therefore, kinetic stabilization plays a key role, whether it is for preventing the decomposition of a metastable elevated-temperature phase or for preventing the nanostructured phase from coarsening. For example, Makiura et al. reported that for AgI, the transition temperature (T_c) from conductive α phase to β and γ polymorphs decreases with decreasing mean nanoparticle size, leading to a progressively enlarged thermal hysteresis when performing thermogravimetric stability (TGA) tests.[134] Per Figure 2A, the stabilization effect became pronounced when the particle size was reduced to 11 nm. As another example, authors reported that the $LiBH_4$ nanoconfined in mesoporous silica MCM-41 scaffolds (4 nm pores) delivered an impressive ionic conductivity of 0.1 mS/cm at 313 K, which is three orders of magnitude higher than that of the bulk $LiBH_4$ at the same temperature.[135] Solid-state ^{7}Li nuclear magnetic resonance (NMR) analysis on the nanostructured borohydride revealed an enhanced ionic mobility, similar to the elevated-temperature hexagonal

$P6_3/mmc$ superionic $LiBH_4$ phase.[135] The superionic borohydride was believed to be present at the SiO_2 interface because a significant portion of the structure transformed into the equilibrium low-temperature phase while the conductivity remained. The enhanced ionic conductivity may also be an interfacial effect. With only ball milling SiO_2 and $LiBH_4$, the ionic conductivity increases to 10^{-4} S/cm at room temperature (Figure 2B).[136] Liang et al. prepared nanoporous β-Li_3PS_4 with much more favorable ionic conductivity than that of the bulk Li_3PS_4. These results are shown in Figure 2C.[137] It is not obvious how nanoporosity could affect the bulk thermodynamic properties of this material, making it feasible that metastability and interfacial transport are responsible for the enhancement.

For example, $LiBH_4$ normally exists as an orthorhombic structure at room temperature and transforms into a hexagonal structure above 110°C.[122] The transition temperature is reduced with halides (I^-, Br^-, Cl^-) replacing BH_4^-. As shown in Figure 2D, a 25% replacement of BH_4^- by I^- ($3LiBH_4 \cdot LiI$) decreases the phase transition temperature to below room temperature, stabilizing the elevated-temperature superionic conductivity for ambient operation.[122] Heteroatoms with a larger size, e.g., I^- versus Br^- and Cl^-, are more effective in lowering the phase transition temperature. This has been attributed to expanded lattice with larger size anion doping. When the lattice is expanded by heating or ion doping, the low-temperature phase becomes less stable and will transform into the elevated-temperature phase. The role of substituting ions in the instability of the distorted lattice may be viewed as an application of the Goldschmidt's tolerance factor, which was originally employed for the doped perovskite structure. A summary of representative Li and Na superionic elevated and low-temperature structures is provided in Table 1; the table also shows the doping additives employed to reduce the transition temperature.

Holistic aspects of SSE performance in ASSB cells

There are other important transport parameters that are relevant to the performance of a SSE, in addition to the solid-state ionic diffusion activation energy and diffusivity. This is especially the case when the SSEs are implemented into complete ASSB, i.e., when system has to perform over many cycles. SSEs have the propensity to develop unstable interfaces at both the anode and at the cathode, in some cases, with a greater severity than that for organic electrolytes. Figure 3 provides a schematic of deleterious cycling-induced void formation and dendrite growth at the Li anode/SSE interface in an ASSB. Parallelly, the figure also illustrates the deleterious cycling-induced reaction of the ceramic cathode with the SSE, leading to SSE oxidation and the loss of transition metals from the cathode, degrading its structure. The volume changes of cathode also increase the interface resistance between active materials and solid electrolytes. On the anode side, the void formation during discharge reduces the interfacial contact area. This reduction in area focuses the ionic current upon charging, raising the local current density and facilitating solid electrolyte reduction and dendrite formation. Both issues remain as key material science challenges for the realization of ASSBs. The cathode reactions lead to rapid capacity and voltage decay in the battery, whereas the anode reactions lead to the same effect plus the possibility of electrical shorting.

The volume of both electrodes may change significantly during the charge/discharge cycle. A good SSE should be able to reversibly deform to accommodate such volume change and keep a close contact with the electrodes, which is essential to maintain the battery capacity and cycle performance.[102,139,140] This "pliability" of the SSE can be calculated from its elastic constants, assuming that there is negligible plastic deformation of the SSE during charging and discharging. For example, the

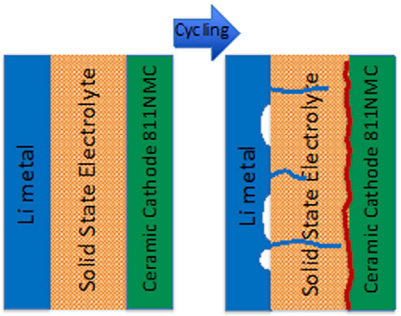

Figure 3. Interfacial problems of sulfide-based solid-state electrolytes in lithium ion all-solid-state battery

Overview of challenges for sulfide-based solid-state electrolytes (SSEs) in full high-voltage all-solid-state battery (ASSBs). Failure entails void formation and dendrite growth at the anode/solid electrolyte (SE) interface. It also entails the reaction of the SSE with the ceramic cathode, leading to one or a combination of SSE-cathode mechanical separation, formation of ionically insulating, electrically conductive reaction products, and the leaching of transition elements from the cathode.

elastic constants of a cubic material are proportional to the square of the slope of the acoustic branches along certain high-symmetry directions in the reciprocal space and can be extracted from the computed phonon dispersion relations.[102] If the SSE only exhibits very low-energy acoustic modes, the slope of its acoustic branches and, hence, its elastic constants are expected to be small. This can lead to low Young's modulus of the material, as seen in most soft sulfide SSEs with Young's moduli in the range of 18–25 GPa.[140] Besides a low Young's modulus, typical flexible materials often have a Poisson's ratios in the order of 0.1. SSEs with such metrices are likely to make better contact with the electrodes in a battery cell. Sulfides are also plastically soft, "flowing" around the harder ceramic cathode particles and leading to better contact both initially and after cycling-induced volumetric changes. Oxide-based SSEs are significantly more elastically stiff and plastically hard, creating interfacial contact problems during both fabrication of the ASSB and subsequent cycling. For a polycrystalline SSE, large grain size is favored for high ionic conductivity.[141] However a larger grain size in a thin SSE specimen (i.e., same order of magnitude dimensions) may lead to more profound stress concentrations at few grain boundaries, resulting in greater localized cracking. The high elastic modulus of oxides may help to physically block metal dendrites if they grow by penetrating the bulk structure.[142] However, as will be discussed, dendrites often grow along defect paths, such as internal pores and grain boundaries, where the localized electric fields thermodynamically favor metal nucleation. In this case, bulk SSE elastic properties would be less relevant for their propagation.

A hierarchy of models have been developed to evaluate the chemical and electrochemical reactions between the SSE and the anode/cathode. These include methods considering only the fast-ion diffusion of the alkali-ions, of multispecies equilibria at the interface, and of explicit interfacial simulation using *ab initio* molecular dynamics (AIMD).[143] The first two methods are computationally affordable and based on the assumption that the alkali-ions are the main diffusive species inside a SSE and at its interfaces. This assumption is reasonable because, unlike liquid electrolytes with both mobile alkali cations and counter-ions, SSEs only have mobile alkali-ions with an ion transference number >0.99. The SSE can be treated as an open system to the alkali-ion of interest. In this case, the phase equilibria at the electrode/electrolyte interfaces can be estimated using a grand potential phase diagram

construction.[143] When the battery is fully charged, the SSE is subject to the maximal electrochemical potential. The alkali metal anode at high chemical potential acts as an alkali source, and the cathode at low alkali chemical potential acts as an alkali sink. Based on this model, the alkali uptake against the cell voltage can be calculated using the available stable phases in the Materials Project database.[144] The predicted phase equilibria at different voltage regions can then show the intrinsic electrochemical stability window (ESW) of the SSE against the alkali metal. It is also found that the practical ESW of an SSE could be much higher than the calculated intrinsic values. If the interface decomposition product phases are good insulators with poor electric conductivity, they can effectively passivate the SSE leading to a high overpotential.[145] The third method of AIMD considers the kinetics of all compositional ions at the interfaces. However, it is computationally intensive because it involves the construction of a large structure model containing layers of electrode materials, SSE, and, possibly, buffer layers of the materials in between. The structure and chemical stabilities of the simulated interfaces after a reasonable simulation time (~ hundreds of picoseconds) can be evaluated by comparing the radial distribution functions of the interface with those of the possible decomposition phases in database.[143]

GARNET LLZO ($Li_7La_3Zr_2O_{12}$)

Structure and ionic conductivity of garnet LLZO

Garnet $Li_7La_3Zr_2O_{12}$ (LLZO) is a well-explored superionic conductor SSE due to its favorable ionic conductivity and kinetic (not thermodynamic) stability relative to Li metal and ceramic cathodes.[94,146–150] There are two crystal structures of LLZO, tetragonal phase (t-LLZO) and cubic phase (c-LLZO). These structures are illustrated in Figures 4A and 4B, respectively.[130,151] The space group of the tetragonal structure LLZO is $I4_1/acd$ with a lattice constant of a = 13.134(4) Å and c = 12.663(8) Å,[130] whereas the space group of cubic structure LLZO is $Ia\bar{3}d$ with a lattice constant of a = 13.03 Å (520 K).[129] In both t-LLZO and c-LLZO, Zr^{4+} occupies the ZrO_6 octahedral site and the larger diameter La^{3+} occupies 8-fold coordinated LaO_8 dodecahedra. The difference between these two structures is in the Li^+ sites, which is the primary reason for the difference in the ionic conductivity. In t-LLZO, all the three Li^+ positions (Li1 located at tetrahedral *8a*, Li2 located at octahedral *16f*, and Li3 at octahedral *32g*) are fully occupied,[151] whereas in c-LLZO, two kinds of Li^+ (Li1, tetrahedral *24d*, Li2, octahedral *96h*) are only partly occupied. For c-LLZO, positions of Li1 and Li2 are close to each other (1.602 Å). The repulsion between lithium ions with such short distance makes it impossible to fully occupy the adjunct sites. For example, the Li1 site is occupied with the two adjacent Li2 positions being vacant, and the lithium ions will migrate along this path (from Li1 site to the adjacent empty Li2 site or vice versa). Besides the enriched vacancies and the short jump distance, it has been found that the collective motion of strongly correlated Li ions in c-LLZO also contributes to its superionic conductivity.[103] According to high-resolution solid-state NMR, a third Li^+ located at *48g* octahedral site was identified in $Li_{7-2x-3y}Al_yLa_3Zr_{2-x}W_xO_{12}$ ($0 \leq x \leq 1$).[152] In addition, $^6Li-^6Li$ exchange spectra indicates a correlation between the octahedral (*96h*) and tetrahedral (*24d*) sites, which means that Li+ jumps between *96h* and *24d*. These results confirm the lithium migration pathway in LLZO, which is along 24d−96h−48g−96h−24d.[152]

The ionic conductivity of the c-LLZO is two orders of magnitude above that of the tetragonal phase, but the t-LLZO structure is more stable at room temperature. Employing density functional theory (DFT) simulations, the authors demonstrated that the phase stability of t-LLZO is determined by a simultaneous ordering of the Li

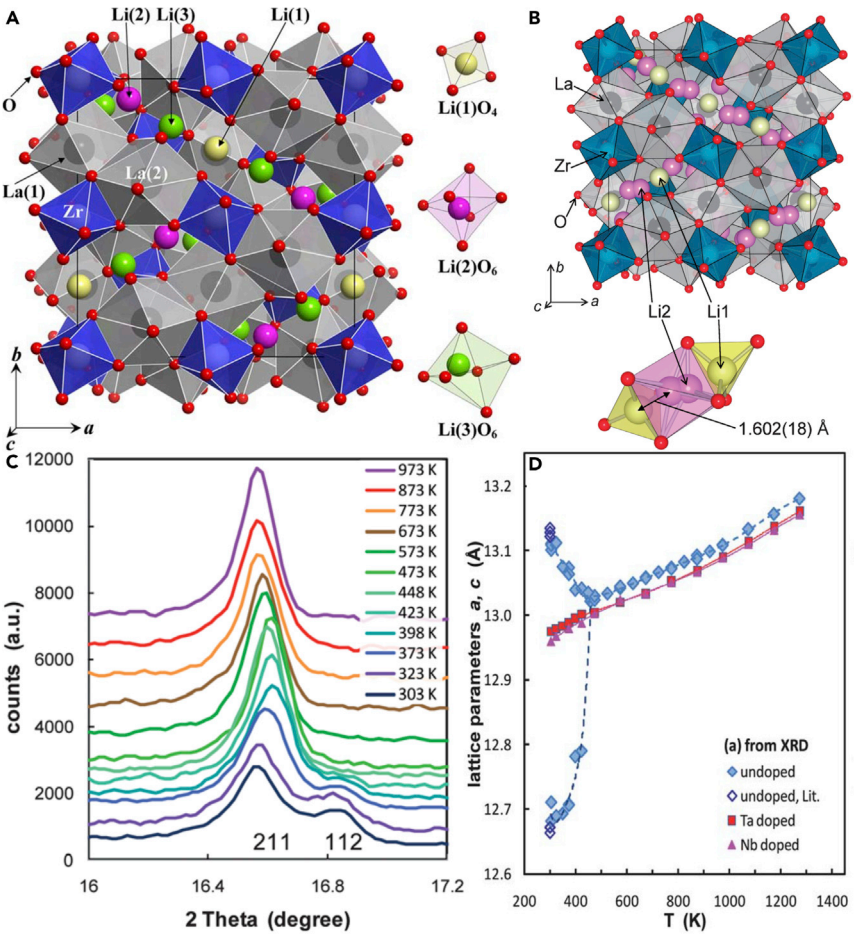

Figure 4. Structures and phase transitions in garnet $Li_7La_3Zr_2O_{12}$

(A) Crystal structure of tetragonal $Li_7La_3Zr_2O_{12}$ (LLZO). Reprinted from Awaka et al.[130] with permission. Copyright 2009, Elsevier Inc.

(B) Crystal structure of cubic LLZO. Reprinted from Awaka et al.[151] with permission. Copyright 2011, The Chemical Society of Japan.

(C) *In situ* X ray diffraction (XRD) analysis of $Li_7La_3Zr_2O_{12}$, showing the evolution of the structure with heating.

(D) Plot of undoped and Ta-, Nb-doped lattice parameters versus temperature, highlighting doping-induced stabilization of the cubic structure. Reprinted from Adams et al.[129] with permission. Copyright 2012, The Royal Society of Chemistry.

ions on the Li sublattice and a volume-preserving tetragonal distortion that relieves internal structural strain.[153] The authors also demonstrated that high-valent doping (Al^{3+} at Li^+ site[131] or Nb^{5+}/Ta^{5+} at Zr^{4+} site[129,154,155]) will introduce vacancies into the Li sublattice, which reduces the Li-ion population and Li-ion Coulombic repulsion in the framework and stabilizes the elevated-temperature cubic phase by reducing the free energy gain from ordering. The critical temperature for cubic phase stability is lowered as the Li vacancy concentration is increased, with the cubic structure being favored as the vacancy number per formula unit is increased to 0.5 and above.

The authors combined simulations and experimental analysis to examine the correlation between structure and ion mobility in $Li_{7-x}La_3(Zr_{2-x}M_x)O_{12}$ (x = 0, 0.25; M = Ta^{5+}, Nb^{5+}).[129] It was demonstrated that pentavalent doping enhances

ionic conductivity by increasing the vacancy concentration and reducing the Li ordering. Moreover, at elevated temperatures, the Li is gradually redistributed to the tetrahedral sites up to a site occupancy factor equaling 0.56. The *in situ* XRD analysis demonstrated that the tetragonal to cubic phase transition occurred above 177°C for $Li_7La_3Zr_2O_{12}$. These *in situ* XRD results and obtained lattice parameters are illustrated in Figures 4C and 4D. Above the phase transition temperature, the (211) and (112) peaks from t-LLZO merge together due to the higher symmetry of c-LLZO. High-valence Ta^{5+}/Nb^{5+} doping at the Zr^{4+} site successfully reduced the phase transition temperature, with no transition to tetragonal phase at room temperature. This is illustrated in Figure 4D, which demonstrates the effect of doping on the lattice parameters as a function of temperature.

Chemical stability of garnet LLZO

One disadvantage of LLZO is that it is known to degrade in humid air and form reaction layers when exposed to air.[154,156] The reaction between LLZO and moisture is conceptualized according to Equations 6 and 7:

$$Li_7La_3Zr_2O_{12} + x\ H_2O \rightarrow Li_{7-x}H_xLa_3Zr_2O_{12} + x\ LiOH \quad \text{(Equation 6)}$$

$$LiOH + 1/2\ CO_2 \rightarrow 1/2\ Li_2CO_3 + 1/2\ H_2O \quad \text{(Equation 7)}$$

The Li^+/H^+ exchange has a strong negative impact on the ionic conductivity of the LLZO.[154,156] In addition, the Li_2CO_3 formation layer blocks ion transfer at the interface,[157] leading to a major increase in the interface resistance.[158] First-principle calculations showed that the work of adhesion between Li and Li_2CO_3 (0.1 J/m^2) is less than that between Li and LLZO (0.67 J/m^2), leading to increased wetting contact angle (142° versus 62°) and interfacial resistance (400 versus 2 Ω/cm^2).[159] The Li_2CO_3 can be removed by wet polishing followed by heating at elevated temperature (>500°C), leading to a reduction of interfacial resistance from 400 to 2 Ω/cm^2.[159] Li_2CO_3 on the surface of LLZO also affects the ionic transport through the polyethylene oxide (PEO)-LiTFSI polymer and LLZO interface because the Li_2CO_3 layer acts as a barrier for charge transfer.[157,160] With Li_2CO_3 on the surface, the area-specific resistance (ASR) between LLZO and PEO can be up to 14.57 $k\Omega\cdot cm^2$, which can be reduced to only 0.20 $k\Omega\cdot cm^2$ after removing Li_2CO_3 at 700°C.[160]

Reaction between garnet LLZO and Li metal anode

Another issue with LLZO is its reactivity with the lithium metal anode. When in contact, excess Li^+ is able to occupy the Li sites in the cubic LLZO, according to the following equation:[32]

$$2Li_{(s)} + V_{\ddot{O}}(LLZO) \rightarrow 2Li_i^{\cdot}(LLZO) + V_{\ddot{O}}^{\times}(LLZO) \quad \text{(Equation 8)}$$

The back filling of Li^+ makes the cubic LLZO unstable at room temperature, making it gradually transform into a tetragonal LLZO. This conclusion is directly supported by electron energy loss spectroscopy (EELS) and the associated schematic shown in Figure 5A.[146] The evolution of the oxygen K-edges in the EELS spectra demonstrates this transformation, where ~ 6 nm interface layer of LLZO becomes tetragonal. Further decomposition to ZrO_y compounds at the LLZO/Li interface also occurs under such reducing conditions (0 V versus Li/Li^+). This conclusion is based on DFT simulations and separately on analysis of the X-ray photoelectron spectroscopy (XPS) spectra of the interface layer.[161,162] As a positive attribute, however, the interphase layer derived from the reaction between LLZO and Li is kinetically stable,

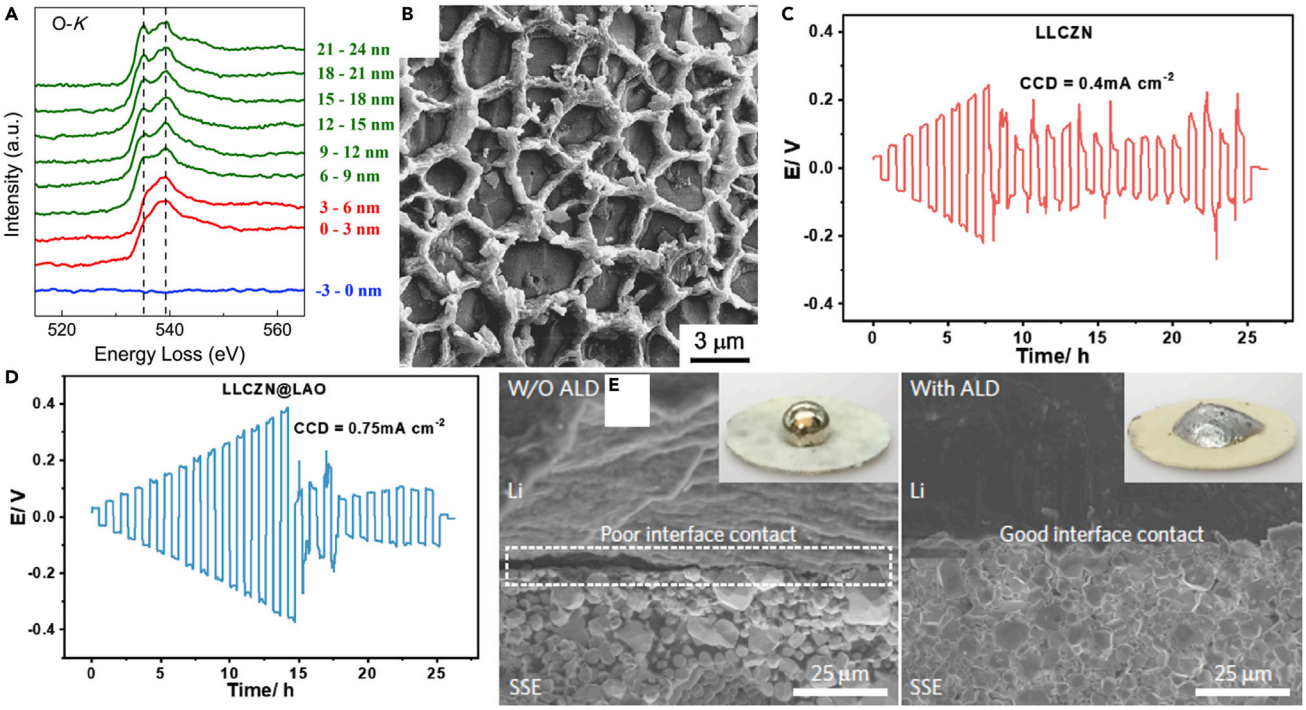

Figure 5. Stability of garnet $Li_7La_3Zr_2O_{12}$ against Li metal

(A) Oxygen K-edge EELS line scan data of c-LLZO-Li interfacial layer as a function of distance in nm. Reprinted from Ma et al.[146] with permission. Copyright 2016, American Chemical Society.

(B) SEM image of dendritic Li metal nucleated at the grain boundaries of LLZO. Reprinted from Cheng et al.[163] with permission. Copyright 2016, Elsevier Ltd.

(C and D) Lithium platting/stripping performance of LLCZN and LLCZN@LAO in Li symmetric cells at different current densities. Reprinted from Song et al.[164] with permission. Copyright 2019, WILEY-VCH Verlag GmbH & Co. KGaA, Weinheim.

(E) SEM image of the contact of a garnet surface with molten Li. Reprinted from Han et al.[165] with permission. Copyright 2017, Nature Publishing Group.

ensuring that the bulk c-LLZO material remains unchanged even after extended contact with Li metal.[146]

Dendrite growth with garnet LLZO

A major secondary problem for LLZO in contact with Li is dendrite formation and growth, which can lead to battery short circuits during extended cycling.[166] During ongoing charging-discharging, the Li^+ ions migrate between the anode and cathode through the solid electrolyte.[167] With a fully homogeneous solid electrolyte having a constant ion diffusion resistance, the reduction of voltage would be linear from the cathode to the anode.[168] The voltage away from the anode would always be larger than 0 V versus Li/Li^+, making it thermodynamically impossible to form Li dendrites inside the solid electrolyte. However, the lower ionic conductivity at grain boundaries and pores leads to an enriched Li^+ concentration and a cathodic overpotential sufficient for metal nucleation.[165,169–171] There is also an additional ionic resistance-enhanced electrical conductivity due to the reaction layer(s) formed at the anode-SEE interface. This would further exacerbate the non-uniform field distribution and drive metal nucleation away from the anode. Parallelly, there may be enough electrical conductivity around such sites to allow for the local reduction of Li^+ to form the dendrites. Due to this combination of process-enhanced cathodic overpotentials and localized electrical conductivity, the metal dendrite formation on LLZO is a major impediment toward its utilization on full battery cells. Cheng et al. have directly

observed that Li metal propagated along the interconnected grain boundaries in the polycrystalline $Li_{6.25}Al_{0.25}La_3Zr_2O_{12}$ ceramic electrolyte.[163] Figure 5B illustrates this phenomenon, with the SEM images showing the Li metal decorating the grain boundaries. Qi et al. developed a phase-field model to examine the impact of excess surface electrons on the Li dendrite growth morphology in polycrystalline LLZO.[172] The model successfully explained the experimentally observed dendrite intergranular growth and revealed that the trapped electrons may produce isolated Li metal nucleation, leading to a sudden increase of Li-dendrite penetration depth.

The local overpotential is affected by site-specific ion diffusion limitations (space-charge-layer effects,[173] defect relaxation, and resistance polarization) and localized current density variations.[32,174] Solid electrolyte defects, such as grain boundaries, pore surfaces, and other interfaces, typically possess lower ion diffusivity than the bulk crystal,[175] leading to site-specific concentration polarization.[32] Parallelly, SSEs may possess an increased electrical conductivity than the bulk crystal, still being low but now sufficient to allow the reduction of Li ions to Li metal.[176] In fact, Wang et al. revealed that electrical conductivity is one important condition for the formation of dendrites.[26] Once electrically shorted, there is a mixed electron-ionic conduction, leading the charge-discharge curve of a symmetric Li/SSE/Li cell to be relatively flat with minimum polarization.[25] An increasing charging current density would favor both effects, promoting a greater localized cathodic overpotential due to diffusional limitations and increasing localized electron current density. Dendritic lithium has been observed in LLZO solid electrolytes, which has a relatively high electrical conductivity of 5.5×10^{-8} S/cm at 30°C.[26] By contrast, the electrical conductivity of LiPON is measured to be in the 10^{-15} to 10^{-12} S/cm range.[177] This helps to explain why Li dendrites have not been reported in the LiPON electrolyte.

It should be pointed out that dendrite formation in SSE electrolytes is a complex process that is not fully understood.[174] Lithium growth and penetration through solid electrolytes is fundamentally different from the conventional dendrite growth in liquid electrolytes.[32] According to the Monroe and Newman model, dendrite growth can be suppressed if the shear modulus of SSE or separator is twice the shear modulus of lithium (4.8 GPa at 298 K).[142] Several SSEs are reported to possess relatively high elastic modulus, such as garnet-type $Li_7La_3Zr_2O_{12}$ (LLZO) ($\approx$100 GPa),[178] β-Li_3PS_4 (10–12 GPa).[179] However, Li dendrite can still form and propagate in these high-strength solid-electrolyte (SE)-based batteries.[159] It is likely that the interface kinetics are non-uniform, depending on the localized variations in surface chemistry, reaction layers that may be present, grain boundary orientation, pores, impurities, etc.[32,174] This creates major challenges in predicting or controlling the dendrites in experimentally synthesized SSE materials, which are naturally full of defects such as pores and grain boundaries and contain voids at the anode-SSE interface. Based on such understanding of dendrite formation, targeted strategies can improve the operating current density and cycle life of ASSBs.[25,32] These include reducing the levels of porosity and grain boundary area, which minimizes the grain boundary ionic resistance. Akimoto et al. successfully fabricated large size garnet-type $Li_{7-x}La_3Zr_{2-x}Nb_xO_{12}$ single crystals without grain boundaries and voids using flotation zone method.[180] As a result, this single-crystal $Li_{7-x}La_3Zr_{2-x}Nb_xO_{12}$ delivered a total ion conductivity of 10^{-3} S/cm at room temperature and a critical current density (CCD, the largest current density allowed without shorting) of 0.5 mA/cm^2; both values are considered quite favorable.

Decreasing the electrical conductivity is another effective way to suppress dendrite formation, especially at interfaces, grain boundaries, and pores, where dendrites are

most likely to form.[163,181,172] Qi et al. simulated the performance of surface modified LLZO with an insulating layer of Li_2PO_2N, showing that this approach is effective in suppressing dendrite formation.[176] Pan et al. reported that a 5 nm layer of $LiAlO_2$ (LAO) coated onto the grain surfaces of LLZO prior to sintering results in an improved CCD for the onset of dendrite growth from 0.4 to 0.75 mA/cm^2. These findings are illustrated in Figures 4C and 4D.[166] It was found that when the external voltage was less than 0.4 V, the electrical conductivity was constant. However, as the voltage was increased to over 0.5 V, the electrical conductivity of the SSEs also gradually increased.[164] The change in conductivity was $\approx 1.25 \times 10^{-8}$ S/cm at 0.3 V to 3.59×10^{-8} S/cm at 1 V (LLZO) and $\approx 5.2 \times 10^{-9}$ S/cm at 0.3 V to 1.01×10^{-8} S/cm at 1 V (LAO-coated LLZO). It was argued that the increased electrical conductivity originated from the grain boundaries because the polarization voltage was sufficiently large (around 0.5 V in total) to make them electrically conductive. After coating a 5 nm thin insulating buffer layer of $LiAlO_2$ (LAO) at the grain boundary, the electrical conductivity was effectively reduced, leading to an increased CCD. As Figures 2D and 4C indicate, the measured CCD was 0.75 mA/cm^2, whereas for the baseline pristine LLCZN, this value was 0.4 mA/cm^2.

Hu et al. reported that atomic layer deposition (ALD) grew 5–6 nm layer of Al_2O_3 on the surface of LLZO, leading to a significant decrease of interfacial impedance, from 1,710 to 1 Ω cm^2.[165] Experimental and computational results reveal that Al_2O_3 coating enables the wetting of metallic lithium in contact with the garnet electrolyte surface. The lithiated alumina interface allowed for a more effective Li-ion transport between the lithium metal anode and garnet electrolyte, as illustrated in Figure 5E. With the significantly reduced interfacial resistance after the ALD Al_2O_3 modification, the symmetric Li/SE/Li cell was cyclable at a current density of 0.2 mA/cm^2 for tens of cycles. By contrast, the baseline specimen without the ALD modification short circuited at only 0.1 mA/cm^2.[165]

Reaction between garnet LLZO and the cathode

The electrochemical window of LLZO based on first-principle simulations indicates that LLZO is unstable above 2.91 V versus Li/Li$^+$.[162,182] However, the cyclic voltammetry of Li/LLZO/LLZO+C/Pt cell indicates that LLZO starts to be oxidized at 4 V. The increased voltage compared with theoretical predictions can be explained by kinetic impediments toward decomposition, leading to a large overpotential. XPS results indicate that the molar ratio of O to Zr decreases from 7.6 to 4.9 when charging to 4.5 V, which confirms that O_2 was released during charging.[162] However, this oxidization was kinetically sluggish, especially after the passivation layer of zirconium and lanthanum oxides formed.[162] According to the cyclic voltammetry of Li/LLZO/LLZO+C/Pt cell, the oxidization of LLZO with releasing O_2 was suppressed after the first cycle, with less than 1 μA peak current versus 5 μA for the first charge process.[162] ASSB with LLZO electrolyte and LCO cathode can still cycle for over 100 cycles with high-capacity retention (98%).[183] Other cathodes such as $LiFePO_4$ ($\approx$3.4 V) and S ($\approx$2.2 V) with lower potential versus Li/Li$^+$ are also compatible with LLZO electrolyte.[184] ASSB of $LiFePO_4$/LLZO/Li retains over 130 mAh/g capacity after 50 cycles (65°C, 200 μA/cm^2), whereas for S/LLZO/Li battery, 800 mAh/g capacity can be retained after 60 cycles (65°C, 200 μA/cm^2).[185]

Employing LLZO for fabricating high-power all-solid-state batteries remains a challenge, even with an ionic conductivity close to 1 mS/cm. As shown in Table 2, an ASSB with Li metal anode, LLZO solid electrolyte, and $LiCoO_2$ cathode obtains a capacity of 0.274 mAh/g at a low current density of 2 μA/cm^2.[184] The key impediment to faster rate performance is the resistance of the cathode-LLZO interface, as

Table 2. All-solid-state batteries (ASSBs) based on LLZO solid electrolytes (LLZO represents $Li_7La_3Zr_2O_{12}$, LCO represents $LiCoO_2$, LLZNO represents Nb-doped LLZO, LLZTO represents Ta-doped LLZO, NCA represents Ni and Al co-doped LCO, LLCZN represents Ca and Nb co-doped LLZO, LALZWO represents Al and W co-doped LLZO, and NCM represents Ni and Mn co-doped LCO)

Electrolyte	Cathode	Anode	Temperature and current	Loading (mg/cm^2)	Capacity (mAh/g)	Cycles	Ref.
LLZO	LCO	Li	RT, 2 $\mu A/cm^2$	–	0.274	3	[186]
LLZNO	LCO (PLD)	Li	25°C, 3.5 $\mu A/cm^2$	0.27	127	100	[189]
LLZO	LCO@Li_2CO_3 + $Li_{2.3}C_{0.7}B_{0.3}O_3$ + LLZO@Li_2CO_3	Li	25°C, 0.05 C	1	94	100	[147]
LLZTO	$LiFePO_4$ + C + CPEO + LiTFSI	Li	65°C, 0.1 C	2–3	141.5	200	[184]
LLZTO	NCA + PEO + LiTFSI	Cu	60°C, 0.1 C	3	0.5 mAh/cm^2	50	[190]
LLCZN	S soaked with 1 M LiTFSI in DME/DOL (1:1 by volume)	Li	22°C, 0.2 mA/cm^2	7.5	470	32	[191]
LLCZN with Al coating	$LiFePO_4$ soaked with 1 M LiTFSI in EC/DEC (1:1 by volume)	Li	20°C, 0.1 mA/cm^2	–	120	100	[183]
LLCZN with Si coating	V_2O_5 + CNT	Li	100°C, 50 mA/g	0.2	125	27	[192]
LLCZN with Ge coating	$LiFePO_4$ + Gel electrolyte	Li	25°C, 1C	–	138	100	[185]
LALZWO with graphite coating	NCM + Super P + LiTFSI in PY14TFSI	Li	RT, 0.5C	2	128	500	[193]
LLZTO with HCl treating	$LiFePO_4$ + Super P + ionic liquid	Li	30°C, 0.1C	2	120	150	[194]

reported by Yoshida et al.[184] The authors employed $LiCoO_2$/LLZO pellet/Li metal architecture, measuring the total impedance of the cell to be 1 MΩ.[184] The excessive interfacial resistance, in turn, may be attributed to one or a combination of several factors, including poor physical contact, (electro)chemical instability, stress, and space-charge layer.[147] Directly depositing the cathode onto the LLZO,[186] high-temperature sintering,[187] or filling the gap between the cathode and the LLZO with secondary soft and ionically conductive electrolytes (PEO polymer electrolyte, $Li_{2.3}C_{0.7}B_{0.3}O_3$ glass electrolyte etc.) can reduce the interfacial resistance.[149,50,182] For example, Ohta et al. deposited $LiCoO_2$ on the surface of LLZNO by pulsed laser deposition (PLD). The total resistance of this Li/LLZNO/$LiCoO_2$ battery was reduced to only 700 Ω versus the typical 1 MΩ (Table 2).[184,186] However, the areal capacity remained relatively low (3.5 $\mu Ah/cm^2$ versus typical 3 mAh/cm^2 of 18650 cell[188]) due to the mass loading of the cathode (0.27 mg/cm^2 versus typical 20 mg/cm^2 of 18650 cell[188]).

Sintering at high temperature can improve the contact between LLZO and cathodes, but most cathodes would react with LLZO at high temperatures and form an interface layer between them. Chiang et al.[189] used X-ray photoelectron spectroscopy, secondary ion mass spectroscopy, and energy-dispersive X-ray spectroscopy to track the reaction between LLZO and $LiCoO_2$. Results indicate significant cation interdiffusion and structural changes when heating above 300°C. $La_2Zr_2O_7$, Li_2CO_3, and $LaCoO_3$ are identified as decomposition products with synchrotron X-ray diffraction and X-ray absorption spectroscopy. This interface layer between LLZO and $LiCoO_2$ contributed to an 8-fold increase in interfacial resistance.[189]

Wang et al. incorporated glass electrolyte ($Li_{2.3}C_{0.7}B_{0.3}O_3$) into the cathode layer, which reduced the interfacial resistance between LLZO and $LiCoO_2$ (LCO), achieving the favorable performance listed in Table 2.[147] LCO, LLZO, and $Li_{2.3}C_{0.7}B_{0.3}O_3$ glass electrolyte with weight ratio of 58: 30: 12 were mixed with ethyl cellulose as a binder and a-terpineol as the solvent to prepare the electrode slurry. The slurry was then coated on the surface of LLZO pellet and then vacuum-heated at 100°C to remove the solvent. The LLZO-supported cathode composite was then heated at 700°C to improve the contact of solids. The total resistance was reduced to 300 $\Omega \cdot cm^2$ through this approach. The button cell was cycled at 25°C and a current density of

0.05 C, with 1 mg/cm^2 mass loading and 94 mAh/g capacity retained after 100 cycles. Another strategy is to incorporate polymer electrolytes into the cathode layer.[184] The mechanical softness of polymers gives the composite electrode an improved physical contact with LLZO, with the total resistance being reduced to 95 Ω at 65°C.[184] However, the low ionic conductivity of polymer electrolytes restricts the operating temperature to above ambient, allowing for cycling at 65°C.[184] A battery with $LiFePO_4$ + C + CPEO + LiTFSI composite cathode (2–3 mg/cm^2 $LiFePO_4$), 300 μm LLZTO solid electrolyte, and Li metal anode was cycled at 65°C and 0.1 C. It delivered a reversible capacity of 142 mAh/g after 200 cycles, as shown in Table 2.[184] Wachsman and Hu tuned the garnet solid electrolyte and the Li metal by forming an intermediary Li metal alloy that dramatically improved the wettability of the garnet surface and reduced the interface resistance by more than an order of magnitude.[185] For the baseline $Li_7La_{2.75}Ca_{0.25}Zr_{1.75}Nb_{0.25}O_{12}$ (LLCZN) /Li, the ionic resistance was 950 Ω cm^2, whereas for surface-engineered garnet/Li, the resistance was 75 Ω cm^2. That seminal study provided new paths to address the garnet SSE wetting issue against Li and, as a result, obtained a more stable cell performance.[183] The same two authors demonstrated a flexible ceramic textile based on the garnet-type conductor $Li_7La_3Zr_2O_{12}$.[195] The unique highly flexible SSE showed a number of advantageous properties, including a lithium-ion conducting cubic structure, low density with multi-scale porosity, and a high surface area to volume ratio.

Outlook for garnet LLZO

The superionic conductivity (~ 1 mS/cm) at 25°C, and the wide (kinetic) electrochemical window of LLZO makes it a promising solid electrolyte. Significant work has been done to improve the ionic conductivity and reduce the interfacial resistance between LLZO and various electrode materials. However, the CCD for most LLZO electrolytes is less than 1 mA/cm^2, which is only C/3 for a typical areal capacity of 18650 cell (3 mAh/cm^2).[164,196] In addition, several other issues also restrict a broader utilization of LLZO for solid-state batteries. These include the following issues. The interface resistance between cathode and LLZO is still as high as hundreds of ohms at room temperature, which strongly limits the power density of the ASSB. The maximum room temperature charging rate achieved with an LLZO SSE in a full battery has been reported as 0.05 C, with only 1 mg/cm^2 mass loading and 94 mAh/g capacity.[147] The thickness of LLZO pellet is still over hundreds of micrometers, which needs to be reduced to gain a higher energy density. For most ASSBs with LLZO pellet, the thickness of LLZO is at least 200 μm to guarantee its strength.[147,184,186,189,190] Tape casting followed by sintering is a salable way to prepare ceramic films from several millimeters to less than 100 μm.[197,198] Doeff et al. fabricated LLZO film with a thickness of 25–44 μm with tape casting.[197] The precursors of LLZO, Li_2CO_3, polyvinyl butyral, and benzyl butyl phthalate were added to alcohol and acetone solvents, subsequently ball-milled for 48 h to homogenize the suspension, and then tape cast onto a Mylar sheet. After drying, the green tape was peeled from Mylar and punched to 22 mm disks. The tape was then placed between graphite foils, which were in turn placed between two alumina plates for mechanical support. The entire stack was heated at 1,070–1,090°C for 1–2 h under Ar for densification. Sintered samples were reheated at 840°C under zero grade air to remove carbon. With this thin film, Li/LLZO/Li symmetric cell showed a total resistance of only 35 Ω·cm^2. However, a short circuit occurred when the current density was increased to 0.2 mA/cm^2.[197] Due to the fragility of the thin ceramic samples, applying pressure may have caused cracks and thus led to the short circuit.

In addition, the highly reactive Li metal anode would bring major difficulties in handling and manufacturing, leading to high fabrication cost. In principle, a Li metal

anode may be unnecessary for Li-containing cathodes. Such "anode-less" or "anode-free" configuration would also reduce the total volume and mass of a solid-state battery. Compared with cells with graphite anode, anode-less cells will save about 50% volume, effectively doubling the cell's specific energy. Even compared with thin Li metal, the cell volume is still reduced by 23% when going anode-less.[190] Therefore, anode-less ASSB architectures in which the Li anode is formed *in situ* during the first charging step are technologically favored.[174,190] Sakamoto et al. designed an ASSB with Cu foil current collector, Ta-doped LLZO (LLZTO) solid electrolyte, and Ni, Al co-doped $LiCoO_2$ (NCA) cathode.[190] The LLZTO with a thickness of 2 mm was polished with 1200 grit sandpaper and then Cu current collector was attached to the LLZTO. The Cu was laminated to LLZTO under a pressure of 3–6 MPa and heated at 700°C in Ar for 5 min. NCA with 3 mAh/cm^2 capacity and about 35% porosity was casted on the other side of LLZTO as the cathode. Then, PEO-LiTFSI electrolyte was infiltrated into the cathode porosity by heating and pressing the PEO under 4.2 MPa and 80°C. With enhanced contact between Cu and LLZTO under pressure of 3–6 MPa and heated at 700°C, Li from NCA cathode would deposit between LLZTO and Cu. The ASSB cell was cycled with current of 0.1 C at 60°C, with 0.5 mAh/cm^2 capacity being retained after 50 cycles (Table 2).[190] The relatively low capacity of 0.5 mAh/cm^2 for the ASSB versus 3 mAh/cm^2 for the cathode is likely due to the instability of PEO and the associated interfaces: The total resistance increased from 90 $\Omega\cdot$cm^2 on the first cycle to 200 $\Omega\cdot$cm^2 after 50 cycles. A cell based on Cu/LLZO/Li was cycled at 0.05 mA/cm^2 (0.85 mAh/cm^2) without a discernable increase in cell impedance.[190] This indicates that an anode-less ASSB based on LLZO should be viable. Table 2 provides examples of the ASSBs that have been achieved using LLZO and related SSEs.

LI-ARGYRODITE (Li_6AS_5X)

Structure and ionic conductivity of Li-argyrodite (Li_6AS_5X)

Unlike rigid oxide-based SSEs, soft sulfide-based electrolytes show better compatibility with electrodes, which can operate at room temperature in ASSBs. Among those sulfides, Li-argyrodite (Li_6AS_5X, A = P, Sb, X = Cl, Br, I) is attracting substantial attention due to its ionic conductivity of over 10 mS/cm and improved stability over the sulfide-based superionic solid electrolytes, such as $Li_{10}GeP_2S_{12}$.[116,95,199–203] There are two different structures of argyrodite-type Li_7PS_6. The orthorhombic ($Pna2_1$) phase illustrated in Figure 6A is stable at room temperature. The face-centered cubic ($F\bar{4}3m$) phase illustrated in Figure 6B is stable above 210°C.[117,204] In both elevated-temperature and low-temperature structures, P^{5+} is located in the tetrahedral site surrounded by four S^{2-} (PS_4). However, the Li^+ ions take different sites in the two structures. In the low-temperature structure, Li^+ ions are fully occupied in seven different sites, namely five tetrahedral, one trigonal, and one linear, being ordered and frozen at these sites.[115] In the elevated-temperature phase, there are two different Li^+ ions with high mobility partially located in 24*g* and 48*h*. Figure 6C illustrates the ionic conductivity of Li_7PS_6 at variable temperatures, also illustrating the phase transition occurring between 450 and 500 K. The activation energy changes from 0.16 eV at low temperature to 0.35 eV at elevated temperature.

The elevated-temperature cubic phase can be stabilized by cation doping at the P^{5+} site with Si^{4+}/Ge^{4+}[117] or anion doping at S^{2-} site with halides.[116,199–201] Four types of cations with different valence and radius were considered to replace P^{5+}.[117] Experimental results indicate that more than 10% of Si^{4+} or Ge^{4+} doping can stabilize the high-temperature (HT) phase, whereas B^{3+} and Al^{3+} cannot.[117] This should be attributed to the radius and valence of doping ions, B^{3+} (0.11 Å) and Al^{3+}

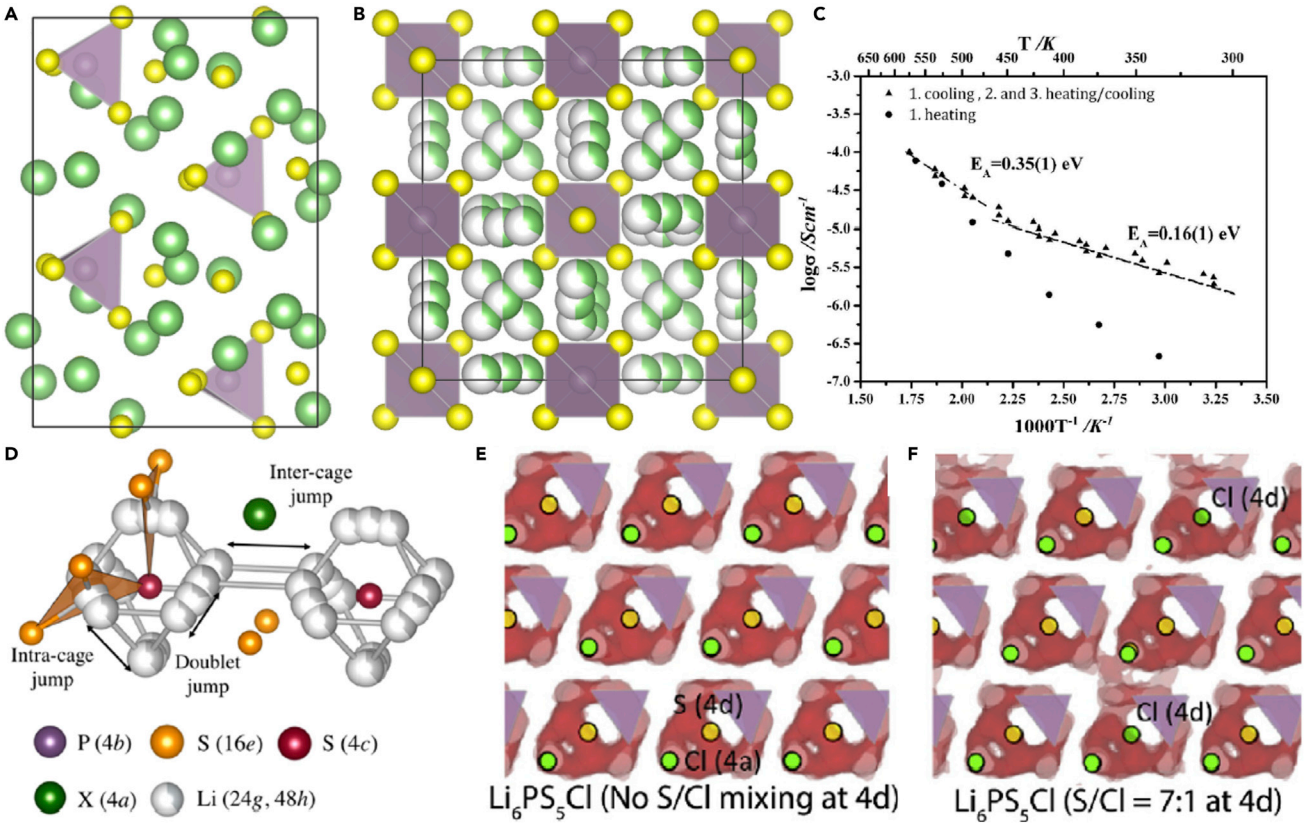

Figure 6. Structures and phase transitions in Li-argyrodite

(A–C) (A) Low-temperature (LT) structure of Li_7PS_6, (B) high-temperature (HT) structure of Li_7PS_6, and (C) Arrhenius plot demonstrating different temperature dependencies of the conductivity corresponding to the HT-LT phase transition of Li_7PS_6, reprinted from Deiseroth et al.[204] with permission. Copyright 2011, WILEY-VCH Verlag GmbH & Co. KGaA, Weinheim.

(D) Schematic illustration of the jumps between the lithium positions; doublet jump (48*h*–24*g*–48*h*), intra-cage jump (48*h*–48*h*), and inter-cage jump (48*h*-48*h*), reprinted from Kraft et al.[205] with permission. Copyright 2017, American Chemical Society.

(E and F) *ab initio* molecular dynamics (AIMD) simulation of Li-ion probability densities of Li_6PS_5Cl without S^{2-}/Cl^- mixing at 4*d* sites, and with S^{2-}/Cl^- mixing 7:1 at 4*d* sites. Reprinted from Feng et al.[199] with permission. Copyright 2020, Elsevier Inc.

(0.39 Å). A large difference in radius and valence versus P^{5+} (0.17 Å) makes doping more difficult. DFT calculations indicate that the energy difference between the elevated-temperature phase and the low-temperature phase ($\Delta E = E_{HT} - E_{LT}$) becomes negative with Si^{4+} or Ge^{4+} doping but remains positive with B^{3+} and Al^{3+} doping. This means that the elevated-temperature phase should be stable at room temperature with Si^{4+} and Ge^{4+} doping.[117] Certain amount of anion (Cl^-, Br^-, or I^-) or cation (Si^{4+}or Ge^{4+}) insertion into the Li_7PS_6 lattice can increase the disorder and reduce the phase transition temperature to below room temperature.

In the cubic ($F\bar{4}3m$), two Li^+ positions at *24g* and *48h* were identified by neutron diffraction and NMR, which are both partially occupied.[116,199] Isotope exchange (^6Li–^7Li), combined with $^{6,7}Li$ NMR experiments, indicate that Li^+ at both *24g* and *48h* contribute to the ion conduction.[199] When applying current on $^6Li||Li_6PS_5Cl||^6Li$ symmetric cell, ^6Li from Li metal is forced to diffuse through Li_6PS_5Cl and ^7Li in Li_6PS_5Cl is replaced by ^6Li. The Li^+ ion transport path can be determined by checking changes of $^{6,7}Li$ signals from different Li^+ sites. For Li_6PS_5Cl, ^6Li at both *24g* and *48h* get enhanced, whereas ^7Li is reduced, which means Li^+ ions diffuse through both *24g* and *48h*.[199] As shown in Figure 6D, there are three types of Li^+ jump modes

in the cubic phase; 48*h*-24*g*-48*h* doublet jump, 48*h*-48*h* intra-cage jump, and 48*h*-48*h* inter-cage jump.[206] The inter-cage jump is the most important jump mode, which contributes to the long-range ion diffusion. However, the inter-cage jump distance is the longest among these three, which makes it less likely to happen, limiting the ionic conductivity.[206] A factor that can promote the inter-cage jump is the disorder between S at *4d* site and halide at *4a* site. For example, S at *4d* site and I at *4a* sites in Li_6PS_5I are fully ordered due to the difference in ion radii (2.2 Å for I^- and 1.84 Å for S^{2-}). Marvin et al. found that introducing Ge at the P site ($Li_{6+x}Ge_xP_{1-x}S_5I$) will induce anion disorder at *4d* and *4a* sites (3% anion disordering with x = 0.6), improving the ionic conductivity from 10^{-6} S/cm for Li_6PS_5I to 5.4 mS/cm for $Li_{6.6}P_{0.4}Ge_{0.6}S_5I$.[201] The role of anion disorder was also confirmed by AIMD simulations of Li_6PS_5Cl.[199] Figures 5E and 5F show the probability densities of Li^+ ions obtained from AIMD simulations. The simulations confirm that in ordered Li_6PS_5Cl, ionic diffusion is mostly isolated surrounding the S site (*4d*) but becomes nonlocalized with partial occupancy of Cl^- at free S^{2-} site.[199] Furthermore, Nazar et al. found that Li^+ cation site disorder in $Li_{6+x}M_xSb_{1-x}S_5I$ (M = Si, Ge, Sn) is also important for ion conduction.[202] In the $Li_6Si_{0.7}Sb_{0.3}S_5I$ sample, two more Li^+ ion positions (second 48h and 4d site) were detected. The additional delocalized Li-ion provides intermediate interstitial positions (local minima) for Li^+ diffusion and activates concerted ion migration, leading to a low activation energy of 0.25 eV and ultra-high ionic conductivity up to 24 mS/cm after sintering ($Li_{6.6}Si_{0.6}Sb_{0.4}S_5I$).[202]

Temperature-dependent ^7Li spin-lattice relaxation rate (SLR, $1/T_1$) measurements were used to quantify the intrinsic Li-ion jump frequency of Li_6PS_5Cl.[207] The jump frequency is given by $1/\tau$, where τ is the average residence time for the subsequent jumps. When $1/T_1$ reaches a maximum as a function of temperature, $\tau \cdot \omega_o$ equals 1 and the jump frequency of Li_6PS_5Cl was calculated to be 9.80×10^8 s^{-1}.[208] With the same jump frequency at a maximum SLR, the sample requiring lower temperature has higher ionic mobility.[208] Based on the Bloembergen-Purcell-Pound (BPP) model in the fast-motion region ($\tau \cdot \omega_o \ll 1$), $Li_{6-x}PS_{5-x}Cl_{1+x}$ samples with larger T_1 relaxation time suggest faster Li^+ ion motion.[199,209]

Reactions between Li-argyrodite (Li_6AS_5X) and Li metal anode

Unfortunately, argyrodite also suffers from electrochemical instability both in full and symmetric cells. Figure 7A shows the X-ray diffraction patterns of Li_6PS_5Cl after plating and stripping until short circuit.[210] A symmetric cell of Li/Li_6PS_5Cl/Li was cycled with a current density of 75 $\mu A/cm^2$ and pressure of 25 MPa for about 20 cycles (40 h in total), resulting in a short circuit. The X-ray diffraction patterns shown in Figure 7A highlights the decompositions of Li_6PS_5Cl after reaction with Li metal, with LiCl, Li_2SP_4, and Li_3P_7 phases being observed.[210] These phases are Li^+ ion conductors but electrical insulators, kinetically suppressing further decomposition of Li_6PS_5Cl. However, the relative stability of this interface does not prevent the growth of dendrites and may in fact accelerate the process by making the Li_6PS_5Cl/Li interface highly heterogeneous in terms of geometry, ionic diffusivity, and mechanical properties. It also does not prevent the formation of interfacial voids. At low rates, however, the Li_6PS_5Cl/Li interface remains relatively stable.

Dendrite growth with Li-argyrodite (Li_6AS_5X)

Bruce et al. reported that the symmetric cells based on Li/Li_6PS_5Cl/Li cycled at current less than the critical current for stripping (CCS) without void formation and with stable polarization.[25] Here, CCS is defined as the current density above which Li is stripped faster than it is replenished at the Li/SE interface, resulting in void formation. Cell resistance was maintained at around 14 $\Omega \cdot cm^2$ after 100 cycles with a

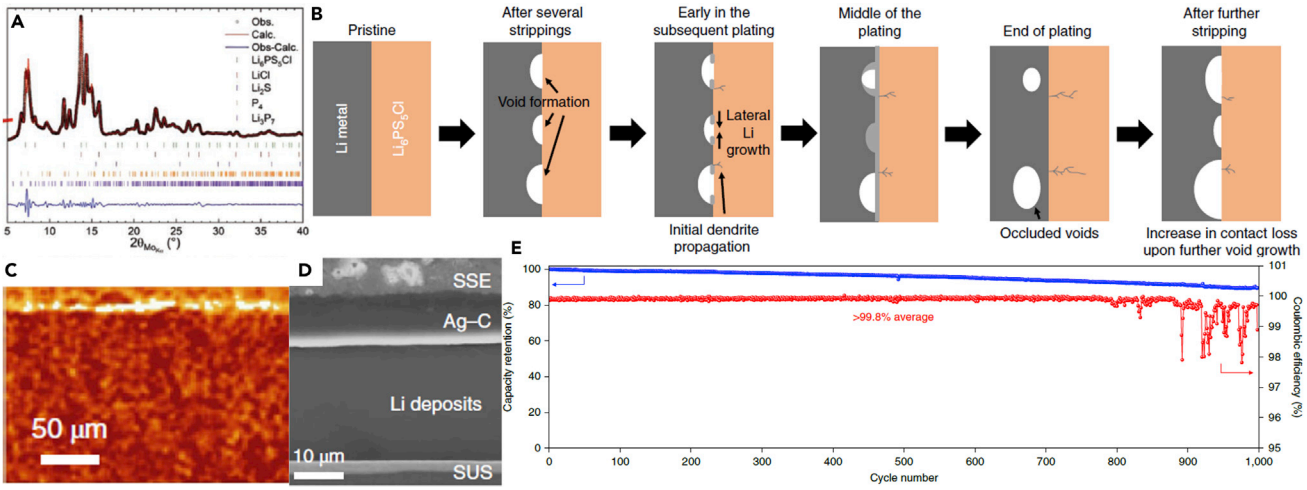

Figure 7. Stability and battery performances of Li-argyrodite

(A) X-ray diffraction pattern of Li_6PS_5Cl of post-cycled (and shorted) Li/Li_6PS_5Cl/Li symmetric cell, under a stack pressure of 25 MPa, reprinted from Doux et al.[210] with permission. Copyright 2019, WILEY-VCH Verlag GmbH & Co. KGaA, Weinheim.

(B) Schematic of the Li metal/Li_6PS_5Cl interface cycled at a current density above the critical current for stripping, reprinted from Kasemchainan et al.[25] with permission.

Copyright 2019, Nature Publishing Group.

(C) *In situ* X-ray computed tomography image of the Li metal-Li_6PS_5Cl interface after 5 cycles at 1.0 mA/cm^2, with a stack pressure of 3MPa.[25]

(D) Cross-sectional SEM image of the same architecture but with a Ag–C nanocomposite layer between the Li and the Li_6PS_5Cl, reprinted from Lee et al.[30] with permission. Copyright 2020, Nature Publishing Group.

(E) Cycling performance and Coulombic efficiency (CE) of the Ag–C|Li_6PS_5Cl|NMC prototype pouch cell, tested at 3.4 mA cm^{-2} between 2.5 and 4.25 V versus Li^+/Li at 60°C.[30]

pressure of 7 MPa and a current density of 1 mA/cm^2.[25] In that study, the increase in cell resistance was attributed to the formation of voids at the interface, leading to a reduced contact area. This mechanism is illustrated in Figure 7B.[25] When the stripping current density removes Li from the interface faster than it can be replenished, voids are formed. Such voids would accumulate during cycling, resulting in a continuously increasing interfacial resistance. Figure 7C shows the *in situ* X-ray computed tomography images of cycled Li metal/Li_6PS_5Cl interface, which confirms the formation of voids at the interface with a current density of 1 mA/cm^2[25] and pressure of 3 MPa. The strong pressure dependence indicates that void filling is a creep process, although it is not known whether dislocation motion is involved or whether it is diffusional creep only. Void formation is also associated with dendrite formation and resulting short circuit from the latter. When voids form at the Li_6PS_5Cl/Li interface, local current density is increased, leading to dendrite formation and growth upon repeated plating. This occurs even when the overall current density is considerably below the threshold for dendrite formation on plating. The role of external pressure was also investigated, and the results indicate that the applied pressure to cells during cycling is a key factor governing CCS.[25] Voids form at a stripping current of 1 mA/cm^2 and dendrites form after several cycles with a pressure of 3 MPa but cycles very stable with higher pressure of 7 MPa. Considerable pressure may be required to achieve high current densities in solid-state cells. Further possible factors, such as surface chemistry, microstructure, adhesion, and mechanical properties of both Li metal and solid electrolyte, may warrant an investigation as they impact the CCD on stripping.

Dendritic formation can be minimized by regulating Li deposition on the current collector and the associated metal wetting behavior.[30] As the baseline, Li metal poorly

Table 3. Examples of all-solid-state batteries based on argyrodite solid electrolytes (NCM represents to Ni, Mn co-doped $LiCoO_2$, LTO represents to $Li_4Ti_5O_{12}$, NBR represents to nitrile butadiene rubber)

Electrolyte	Cathode	Anode	Temperature and current	Loading (mg/cm^2)	Capacity (mAh/g)	Cycles	Ref
$Li_{6.6}P_{0.4}Ge_{0.6}S_5I$	NCM + SE	LTO + SE	60°C and 0.05 C	34	99.3	50	201
$Li_{5.7}PS_{4.7}Cl_{1.3}$	NCM@$LiNbO_3$+ SE	In	RT and 0.75 mA/cm^2	7	15.3	100	212
$Li_{7.25}Si_{0.25}P_{0.75}S_6$	TiS_2 + SE	Li	RT and 0.1 C	–	150	10	117
Li_6PS_5Cl	NCA@$LiNbO_3$ + C +SE	Li	RT and 0.1 C	3.55	120	229	210
Li_6PS_5Cl + acrylate-type binder	NCM@LZO + SE + C + PTFE	Ag + C + PVDF	60°C and 0.5 C	32	130	1,000	30
Li_6PS_5Cl	Li_2S + SE + Super P	In	RT and 0.568 mA/cm^2	6	310	37	213
Li_6PS_5Cl	S + C + SE	Li-In	RT and 0.064 mA/cm^2	3.4	450	50	214
$Li_6PS_5Cl_{0.3}F_{0.7}$	LCO@$LiNbO_3$ + C +SE	Li	RT and 0.13 mA/cm^2	–	90	50	215
$Li_{6.25}PS_{5.25}Cl_{0.75}$	LCO@$LiNbO_3$ + C +SE	Li	60°C and 0.15 C	–	102	50	216
$Li_{5.7}PS_{4.7}Cl_{1.3}$	NCM@ $LiNbO_3$ +SE	In	RT and 0.2 mA/cm^2	10	100	86	217
$Li_{6.7}Si_{0.7}Sb_{0.3}S_5I$	TiS_2 + C + SE	Li-In	RT and C/5	5–6	240	130	202
$Li_6PS_5Cl_{0.5}Br_{0.5}$-infiltrated polyimide	NCM + C + NBR and infiltrated with SE	Graphite + NBR and infiltrated with SE	30°C and 0.1 C	8.5	128	100	218
Li_6PS_5Cl	NCM@$LiNbO_3$+ C + SE + Binder	Li	30°C and 0.05 C	4	100	100	219

wets the stainless steel (SUS) collector, leading to dendritic Li deposition.[30] In the presence of the Ag–C nanocomposite layer (5 μm), dense and uniform Li deposits (25 μm) are formed between the Ag-C layer and SUS substrate, per Figure 7D. The authors proposed that that the Ag improves the ionic conductivity and lowers the nucleation energy of Li metal by forming Ag-Li alloy, which results in the uniform Li deposition.

Reactions between Li-argyrodite (Li_6AS_5X) and the cathode

Dedryvere et al. analyzed the decompositions of Li_6PS_5Cl in the $LiCoO_2/Li_6PS_5Cl$ composite cathode layer.[211] The authors employed XPS depth profiles starting from the cathode layer to the solid electrolyte. It was observed that Li_6PS_5Cl is oxidized into elemental sulfur, lithium polysulfides, P_2S_x ($x \geq 5$), phosphates, and LiCl when charged to over 4 V versus Li/Li^+. Moreover, the decomposition of Li_6PS_5Cl at the cathode varied with depth from the current collector to the solid electrolyte, depending on the two kinetically limiting factors. If the ionic transport within the electrode is the limiting factor, the electrochemical reaction closer to the solid electrolyte is faster than to the current collector. If electron conductivity is the limiting factor, the electrochemical reaction is faster near the current collector. In the $LiCoO_2/Li_6PS_5Cl$/Li-In half cell with 90 μm cathode layer, 570 μm electrolyte layer, and 130 μm anode layer, the maximum decomposition of Li_6PS_5Cl was observed 10 μm from the current collector and 80 μm from the solid electrolyte. This indicated that electron conductivity was the main limiting factor for the decomposition of Li_6PS_5Cl.[211]

Without the addition of carbon additives, the decomposition of $Li_{6.6}P_{0.4}Ge_{0.6}S_5I$ in an ASSB with Ni, Mn co-doped $LiCoO_2$ (NCM) cathode can be suppressed.[201] The cell with a 160 μm NCM + SE composite cathode, a 450 μm $Li_{6.6}P_{0.4}Ge_{0.6}S_5I$ solid electrolyte, and 340 μm $Li_4Ti_5O_{12}$ (LTO) + SE composite anode was able to cycle at 0.25C for 50 cycles at 60°C. The capacity increased from 88.8 mAh/g at the onset to about 100 mAh/g after about 5 cycles and remained at 99.3 mAh/g after 50 cycles. This result is illustrated in Table 3. The total resistance after 50 cycles was only about 15 Ω, making it state-of-the-art from that perspective.[201] Sun et al. also fabricated

ASSB without carbon in the cathode while employing In as the anode (NMC+SE/$Li_{5.7}PS_{4.7}Cl_{1.3}$/In).[212] The capacity decayed to 15.3 mAh/g after 100 cycles when employing a current density of 0.75 mA/cm^2 (Table 3). The impedance increased from the initial 50 Ω to 150 Ω after 100 cycles. An effective way to stabilize argyrodite electrolytes is surface modification of cathode by ion conductors but electron insulators, such as Li_2ZrO_3 and $LiNbO_3$.[29,30,132,205] For example, Lee et al. coated NMC cathodes by sol-gel method with a uniform 5 nm Li_2ZrO_3 coating layer.[30] This significantly reduced the decomposition of Li_6PS_5Cl at the cathode side. A battery based on Li_2ZrO_3-coated NMC cathode, Li_6PS_5Cl solid electrolyte, and Ag/C anode was able to cycle 1,000 times at 0.5C within a voltage window of 2.5–4.25 V versus Li^+/Li at 60°C, with 89% capacity retention, per Figure 7E.[30]

A key advantage of sulfide-based solid electrolytes is the superior mechanical processability compared with oxide-based electrolytes. The softness of sulfides makes it possible to fabricate the solid electrolyte layer by cold pressing, as shown in Table 3. For laboratory evaluation, bulk-type ASSB based on sulfides can be fabricated by cold pressing two electrodes on both sides of the electrolyte.[147] A full ASSB based on sheet-type sulfide solid electrolyte can be prepared and would provide higher energy density than bulk-type batteries.[30] With proper binder and solvent, the argyrodite layer can be made as thin as 30 μm.[30] This is achieved through a casting method analogous to electrode film processing. To minimize the influence of the solvent on the electrolyte and obtain a higher conductivity, the solvent is generally non-polar,[220,207] such as toluene[221] and xylene,[30] with the binder being soluble in the solvent. Different binders have been used in preparing thin solid electrolyte layers, such as oppanol[221] or acrylate-type binder.[30] For example, Lee et al. added 1 wt % acrylate-type binder to Li_6PS_5Cl with xylene solvent to prepare 30 μm thin Li_6PS_5Cl electrolyte layer.[30] Combining a 100 μm Li_2ZrO_3-coated NMC cathode and 5–10 μm Ag–C thin layer anode, the ASSB achieved an energy of 998 Wh/L and a lifetime of 1,000 cycles with only 11% capacity loss (Table 3).[30] These exciting results pointed to the feasibility of achieving practical ASSBs, namely, combining high ionic conductivity sheet-type solid electrolyte with a high-voltage, high-capacity ceramic cathode in an anode-less/anode-free configuration not requiring secondary Li metal.

Coating cathodes with solid electrolytes from solution is one way to improve the contact between cathode and solid electrolyte. Jung et al. prepared a composite LCO film by infiltrating solution-processable Li_6PS_5Cl into conventional LCO film (LCO + carbon + PVDF binder).[222] Argyrodite Li_6PS_5Cl was dissolved in anhydrous ethanol as the solid electrolyte precursor. Conventional LCO film was dipped into the Li_6PS_5Cl solution, followed by drying in an Ar-filled dry box and subsequent heat treatment at 180°C under vacuum. Then, this composite cathode film was cold pressed under 770 MPa.[222] The ASSB using this composite cathode, Li_3PS_4 solid electrolyte, and Li-In alloy anode delivers a capacity of 141 mAh/g (30°C) compared with 118 mAh/g for the LCO composite electrode prepared by dry mixing LCO, carbon, and SE in the same ASSB.[222] The higher capacity for the infiltrated composite cathode is attributed to more intimate contact between LCO and Li_6PS_5Cl, enabled by the solution processing.[222] To date, argyrodite's electrochemical performance at temperatures below ambient remains unsatisfactory for practical applications. This is normally associated with bulk and interfacial ionic diffusion resistance at low temperatures, as the electrical conductivity through carbon etc. should be relatively unaffected. For example, the interfacial resistance of Ag/C/Li_6PS_5Cl/NCM ASSB at 25°C after charging to 4.2 V is 50 Ω·cm^2, whereas it is only 5 Ω·cm^2

at 60°C.[30] More research in this area would be highly desirable, with interfacial modification methods likely being the best path forward.

Wagemaker et al.[223] reported two-dimensional lithium-ion exchange NMR to access the spontaneous lithium-ion transport and provide insight into the influence of electrode preparation and battery cycling on the lithium-ion transport over the interface between an argyrodite solid electrolyte and a sulfide electrode. Interfacial resistance is shown to depend strongly on the preparation method and demonstrated to drop dramatically after a few electrochemical (dis)charge cycles due to both losses in interfacial contact and increased diffusional barriers. According to the 2D NMR results, increasing the contact area between the electrode and electrolyte is helpful to reduce the interfacial resistance for ion transfer, such as reducing the particle sizes and annealing at HT.[223] Further research with 2D NMR demonstrates the important role of space-charge layers at the cathode-solid electrolyte interface.[173] The activation energy of cathode-solid electrolyte interface is only 0.315 eV when it is space-charge free and increases to 0.515 eV with a space-charge layer. Also, this work points out an important strategy to mitigate the space-charge layer effects by reducing the local chemical potential difference at the cathode-solid electrolyte interface.[173] In addition, space-charge layer would cause lithium-ion accumulation at the electrode/electrolyte interface, which is directly observed with *in situ* differential phase contrast scanning transmission electron microscopy (DPC-STEM) technique.[217]

Na_3AB_4 (A = P, SB, AND AS AND B = S, SE)

Structures and phase transitions of Na_3AB_4

When changing from Li to Na, the bigger size of Na^+ affects the distribution sites in SSEs and favorable diffusion paths. Moreover, the stabilities and challenges for Na ASSBs are not the same. Here, the well-studied Na_3AB_4 and NASICON-type SSEs are selected as the representatives of sodium-ion SSEs to illustrate the characteristics and main problems in sodium ASSBs. Na_3AB_4 (A = P, Sb, and As and B = S, Se) is a promising sodium solid electrolyte with high ionic conductivity up to 10^{-2} S/cm at room temperature.[47,48,114,127,224–228] Figures 7A–7C show three different structures of Na_3PS_4 as being stable at different temperatures. Na_3PS_4 is tetragonal ($P\bar{4}2_1c$) up to 261°C, cubic ($I\bar{4}3m$) from 261°C up to 510°C, and orthorhombic (Fddd) above 510°C.[114,124] In the tetragonal phase, two kinds of Na^+ ions occupy *4d* (brown) and *2a* (pink) sites, respectively, with both sites being fully occupied. The cubic phase is believed to be almost ordered, with Na^+ ions fully occupying *6b* sites. However, according to the molecular dynamics (MD) simulations, the Na^+ in the cubic phase are mobile and may move off its stable site toward the neighboring Na sites.[125] This is illustrated in Figure 8B. The orthorhombic phase is disordered with 5 partly occupied Na^+ sites, per Figure 8C. Figure 8D shows the *in situ* synchrotron XRD analysis of Na_3PS_4 at temperatures ranging from room temperature up to 550°C. This description highlights the temperature-dependent transitions between the three different phases.[114] The ionic conductivity of tetragonal phase at 250°C is 0.77 mS/cm, with the activation energy being 0.42 eV. After heating to 450°C and stabilizing the cubic phase, the ionic conductivity increases to 15.5 mS/cm, whereas the activation energy decreases to 0.40 eV.[124] When heated up to 510°C, the structure transforms into orthorhombic structure. The associated ionic conductivity changes from 40 mS/cm to 400 mS/cm, whereas the activation energy decreases to 0.11 eV (Figure 8E).[114]

Sodium vacancies as well as concerted motion of Na^+ play important roles in the ionic conduction of the Na_3AB_4 (A = P, Sb, As and B = S, Se) system.[126,229] Both cubic

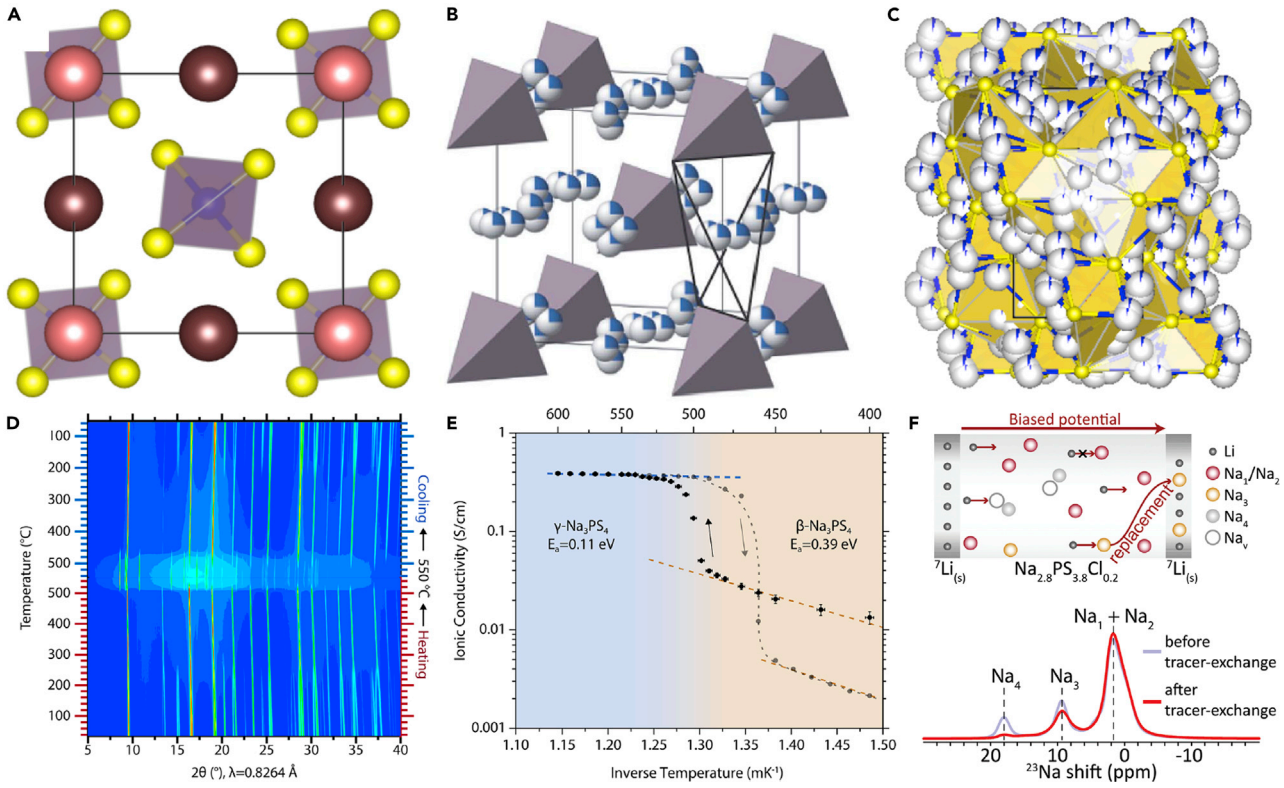

Figure 8. Structures and phase transitions in Na_3PS_4

(A–F) Structure of Na_3PS_4 (A) tetragonal structure (X.F., N.J., and D.M., unpublished data), (B) cubic structure, reprinted from Nishimura et al.[125] with permission. Copyright 2017, The Royal Society of Chemistry, and (C) orthorhombic structure, reprinted from Famprikis et al.[113,4] with permission. Copyright 2019, American Chemical Society. (D) Temperature-controlled synchrotron X-ray diffraction of Na_3PS_4, logarithmic contour plot of diffractograms in the range of 30–550°C upon heating and cooling,[114] (E) Arrhenius conductivity plots of Na_3PS_4 in the range of 400–600°C,[114] (F) Identification of functional defects with tracer-exchange NMR and ^{23}Na solid-state MAS NMR. Reprinted from Feng et al.[225] with permission. Copyright 2019, WILEY-VCH Verlag GmbH & Co. KGaA, Weinheim.

and tetragonal phases display a significant enhancement in the ionic conductivity due to the incorporation of Na vacancies.[47,224,230,231,232] For example, 6.25% Cl^- doping at the S^{2-} site in tetragonal $Na_{3-x}PS_{4-x}Cl_x$ leads to Na vacancy formation. This causes the ionic conductivity to improve from 0.05 mS/cm (tetragonal Na_3PS_4) to 1.14 mS/cm (tetragonal $Na_{2.9375}PS_{3.9375}Cl_{0.0625}$).[111] Further research revealed the influence of two kinds of defects caused by Cl^- doping in Na_3PS_4 ($Cl_S^{\cdot}$ and $V_{Na}^{'}$) on Na-ion transport.[225] Figure 8F shows ^{23}Na solid-state NMR of t-$Na_{2.8}PS_{3.8}Cl_{0.2}$ before and after the tracer exchange of Na with Li, which reveals the importance of the Na vacancies in tetragonal Na_3PS_4.[225] The solid electrolyte was sandwiched between two pieces of ^7Li metal. The Li^+ ions are driven by a voltage to diffuse through the solid electrolyte and replace active Na^+ ions on the diffusion path. Both Na^+ close to Na vacancies (Na4) and Cl^- (Na3) decreased in signal. This was interpreted as Na vacancies and Na^+ ions bonded to Cl^- being replaced by Li^+. It was argued that Na^+ vacancies, as well as Cl^- with lower valence than S^{2-}, enhances the mobility of Na^+ ions.[225] Topological analyses using open-source software Zeo^{++} indicated that the introduction of Cl^- dopant leads to larger Na channel volumes, whereas Na vacancies lead to smaller Na channels. For example, the channel volume of $Na_{2.9375}PS_{3.9375}Cl_{0.0625}$, $Na_{2.9375}PS_{3.875}Cl_{0.125}$, and $Na_{2.875}PS_{3.875}Cl_{0.125}$ was calculated to be 924, 948, and 932 Å^3, respectively.[225] Thus, excessive Na vacancy was actually harmful to Na conduction. Experimental

results indicate that a small amount (<2%) of Na vacancy from thermal defect is sufficient for improved conduction.[225] By adjusting $Cl_S^{\cdot}$ and $V_{Na}^{'}$, the highest ionic conductivity reaches 1.96 mS/cm at 25°C ($Na_{3-\delta}PS_{3.8}Cl_{0.2}$).

Interstitial Na with Si^{4+} replacing P^{5+} ($Na_{3+x}Si_xP_{1-x}S_4$) will also enhance the ionic conductivity.[233] Ong et al. explained how the interstitial Na improves ionic conduction, employing MD simulation.[234] The simulation results indicate that the channel volume and correlation in Na^+ motion play important roles in enhancing the Na^+ conductivity in this structure. With Si^{4+} doping, the channel volume increases from 863 to 879 $Å^3$ ($Na_{3.125}Si_{0.125}P_{0.875}S_4$). Excess Na^+ with partially occupied interstitial sites induce Na disorder in c-Na_3PS_4, which enhances Na^+ motion and thus ionic conductivity.[234] In 2012, Tatsumisago et al. prepared cubic Na_3PS_4 by heating the glass precursor to 260°C, obtaining a high ionic conductivity of up to 0.2 mS/cm at room temperature.[228] From the differential scanning calorimetry (DSC) results, it was found that this cubic Na_3PS_4 transformed into the stable tetragonal phase at 350°C. Local structure analysis employing synchrotron pair distribution function (PDF) confirmed the metastability of the cubic Na_3PS_4 at room temperature.[235]

Doping Na_3PSe_4 with larger size Se^{2-} is another approach to lower the phase transition temperature so as to obtain a cubic crystal structure at room temperature. Such an approach has yielded electrolytes with an ionic conductivity of 1.2 mS/cm.[127] Cation doping with larger Ca^{2+} at Na^+ site can also stabilize c-Na_3PS_4, yielding cubic $Na_{2.73}Ca_{0.135}PS_4$.[224] A strong Coulombic repulsion would repel neighboring Na^+ from Ca^{2+}. Thus, Na vacancies readily formed and trapped Ca^{2+}, resulting in a high migration barrier.[224] Cation doping with larger size Sb^{5+} (Na_3SbS_4) decreases the phase transition temperature to 120°C.[126,236] More importantly, Cubic Na_3SbS_4 delivers a uniquely high diffusion coefficient (2.077×10^{-10} m^2/S) and low activation energy (0.036 eV). This is due to a shorter jump distance (2.85 Å), as demonstrated by *in situ* quasi-elastic neutron scattering.[68] DFT calculations indicate the energy difference between t-Na_3SbS_4 and c-Na_3SbS_4 to be only 4.3 meV/atom, making it easier to stabilize c-Na_3SbS_4 at room temperature.[236] The t-Na_3SbS_4 is more stable when the volume is less than 375 $Å^3$, whereas c-Na_3SbS_4 becomes more stable with larger volume.[236] Doping W^{6+} at Sb^{5+} site can further lower the phase transition temperature and stabilize the cubic phase at room temperature.[47,48] W^{6+}-doped Na_3SbS_4 was prepared by quenching from over 500°C ($Na_{2.88}W_{0.12}Sb_{0.88}S_4$)[35] or by heating at low temperature (275°C, $Na_{2.9}W_{0.1}Sb_{0.9}S_4$),[47] achieving an activation energy of 0.18 eV in both cases. The ionic conductivity of $Na_{3-x}W_xSb_{1-x}S_4$ reached over 30 mS/cm.[47,48]

Reactions between Na_3AB_4 and Na metal anode

Unfortunately the interface between Na_3PS_4 (Na_3SbS_4) and Na metal is highly reactive and not self-passivating.[237] The Na/Na_3PS_4/Na cells fail due to the high interface resistance rather than by short circuiting, and the sodium dendrites in Na_3PS_4 have not been reported.[238] Figure 9A shows the XPS spectra of the electrolyte-metal interface after cycling Na_3PS_4 and 6.25% and 12.5% NaCl-doped Na_3PS_4.[237] It is evident that P^{5+} in Na_3PS_4 converts to Na_3P, P, and other compounds. The Na_3P or Na_3Sb phases have a low band gap (0.4 and 0.68 eV) and are able to conduct electrons, making the reacted interface a mixed electron-ion conductor and hence not self-terminating in growth.[237] At cathodic voltages, Na_3PS_4 is also unstable. According to DFT calculations, the equilibrium electrochemical window for Na_3PS_4 is actually quite limited, being 1.55–2.25 V versus Na/Na^+.[239] Upon charging to above 2.25 V, the Na_3PS_4 structure will decompose to Na_2PS_3, $NaPS_3$, P_2S_7, and S. To evaluate the electrochemical stability of Na_3PS_4, a liquid cell with Na_3PS_4 + C + binder,

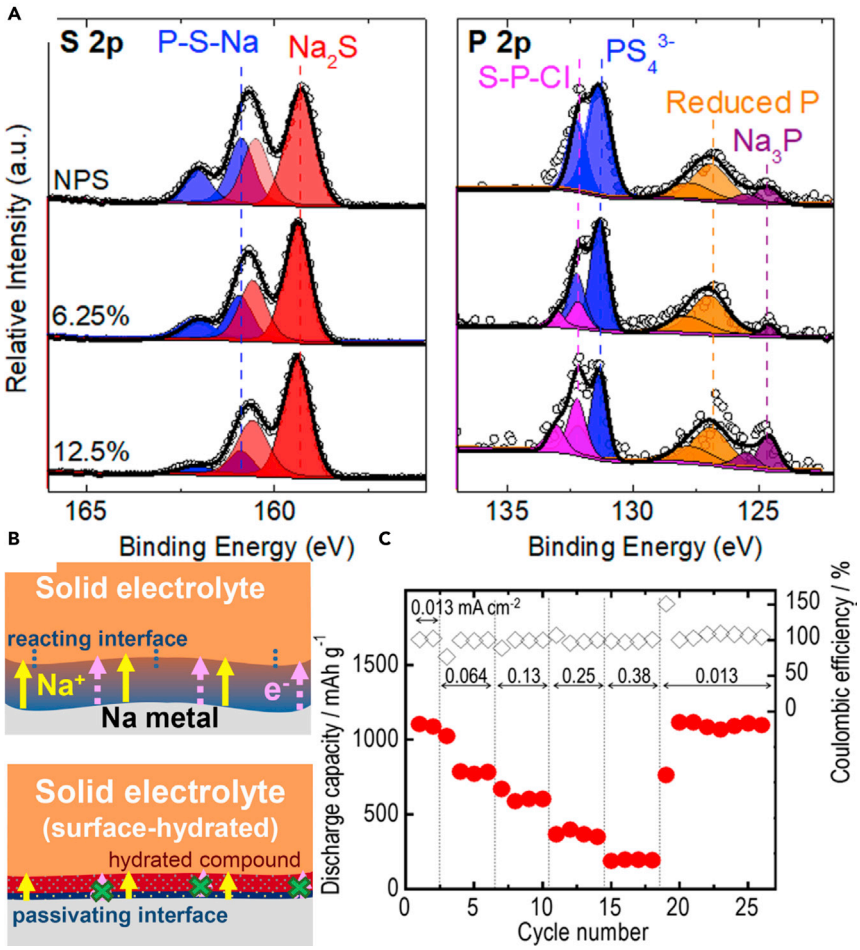

Figure 9. Stability and battery performances of Na_3PS_4

(A) XPS of interface layer after cycling of Na_3PS_4, 6.25% and 12.5% NaCl-doped Na_3PS_4, reprinted from Wu et al.[237] with permission. Copyright 2018, American Chemical Society.

(B) Schematic illustration of stabilizing solid electrolyte-Na metal interface with hydrated Na_3SbS_4, reprinted from Tian et al.[240] with permission. Copyright 2019, Elsevier Inc.

(C) Rate performance of S/Na_3PS_4/$Na_{15}Sn_4$ battery, reprinted from Tanibata et al.[241] with permission. Copyright 2017, American Chemical Society.

separator + liquid electrolyte, and Na anode was charged. An oxidation reaction began at 2.5 V, corresponding to a total capacity of 300 mAh/g.[239] This high-capacity indicated a nearly complete extraction of Na^+ ions from Na_3PS_4 (theoretical capacity 352 mAh/g). Dendrites may grow at the Na metal Na_3PS_4 interface. However, the poor electrochemical stability of Na_3AB_4 results in such a rapid decay that there is likely not enough accumulated capacity for dendrites to form. This point should be investigated further because there is little evidence in either direction.

Due to the instability of Na_3AB_4 against Na metal, the batteries with Na_3AB_4 solid electrolyte and Na anode rapidly lose capacity. Methods to stabilize the interface include suppressing electron conductivity so as to minimize the extent of Na_3P and Na_3Sb formation. The *in situ* hydrated $Na_3SbS_4 \cdot 8H_2O$ plays a positive role in stabilizing the interface between Na_3SbS_4 and Na. As illustrated in Figure 9B, the stabilization mechanism is the growth of electrically insulating NaH (Na_2O) at the interface due to the reaction with Na metal.[240] Sun et al. coated 50 nm Alucone

Table 4. Summary of all-solid-state batteries based on Na_3AB_4 solid electrolytes (NVP represents $Na_3V_2(PO_4)_3$)

Electrolyte	Cathode	Anode	Temperature and current	Loading (mg/cm^2)	Capacity (mAh/g)	Cycles	Ref
Na_3SbS_4	TiS_2 + SE	Na	RT and 0.11 mA/cm^2	8.92	0	30	242
Na_3SbS_4	TiS_2 + SE	Na@Alucone	RT and 0.11 mA/cm^2	8.92	140	30	242
Na_3PS_4	S + SE + C	$Na_{15}Sn_4$ + C	RT and 0.013 mA/cm^2	–	>1,000	25	241
Na_3SbS_4	$NaCrO_2$ + SE + C	$Na_{15}Sn_4$ + C	RT and 0.13 mA/cm^2	5.3	130	20	236
Na_3SbS_4	$Se_{0.8}S_{7.2}$@PAN@SE + C	$Na_{15}Sn_4$ + C	RT and 0.36 mA/cm^2	1.23	280	150	243
Na_3PS_4/PEO/$NaClO_4$ composite	SnS_2 + SE + Super P	Na	RT and 20 mA/g	–	220	40	244
Na_3PS_4	TiS_2 + SE	$Na_{15}Sn_4$	RT and C/15	–	140	19	245
$Na_{3-\delta}PS_{4.8}Cl_{0.2}$	NVP + SE	Na	RT and 10 mA/g	10	80	10	225
$Na_3P_{0.62}As_{0.38}S_4$	TiS_2 + SE	Na-Sn alloy	80°C and 4.8 mA/g	–	110	9	226
$Na_{2.9375}PS_{3.9375}Cl_{0.0625}$	TiS_2 + SE	Na	RT and 0.149 mA/cm^2	4	80	10	111

on Na metal using ALD, resulting in a marked reduction in the decomposition of Na_3SbS_4.[242] With this protection layer, the interface resistance between Na and Na_3SbS_4 increased only slightly, going from 700 Ω to about 800 Ω after 24 h of contact. The baseline specimen without the Alucone had its interface resistance increase from 650 to 1,250 Ω within the same exposure time. The baseline cell with TiS_2 + SE as cathode, Na_3SbS_4 as solid electrolyte, and bare Na as anode can only cycle for about 15 cycles at 0.11 mA/cm^2.[242] Due to this relatively short cycling regiment, the capacity cell decayed to effectively nil (Table 4).[242] The coating layer of Alucone on Na improves the cycle performance for which the battery capacity retains 140 mAh/g after 30 cycles.[242] Replacing Na metal by Na-Sn alloy suppresses the formation of Na_3P, improving the interfacial stability.[111,241] Tin is an alloying anode with Na, forming a series of intermetallics with increasing Na content up to $Na_{15}Sn_4$. A stable anode-electrolyte interface can be obtained with $Na_2Sn|Na_3PS_4|Na_2Sn$ symmetric cell.[239] The overall thermodynamic stability of these intermediate and terminal phases prevents the decomposition of the solid electrolyte and is a well-known strategy for stabilizing a range of SSEs. The issue, of course, is the marked reduction in cell energy when an ion anode rather than a metal anode or an anode-less configuration is employed.

Reactions between Na_3AB_4 and the cathode

Employing a high-voltage cathode against Na_3AB_4 also significantly limits the cycling performance. For example, Zhang et al. employed an ASSB based on a $NaCrO_2$ cathode with Na_3SbS_4 solid electrolyte and an $Na_{15}Sn_4$ anode.[236] Starting with an initial capacity of over 250 mAh/g, only 130 mAh/g was retained after 20 cycles at 0.13 mA/cm^2. As illustrated in Table 4, due to the thermodynamic instability of Na_3AB_4 with a high-voltage ceramic cathode, the majority of Na_3PS_4/Na_3SbS_4 solid electrolytes employ S or sulfides as cathodes. Likewise, due to the thermodynamic instability of Na_3PS_4/Na_3SbS_4 with Na metal, a Na-Sn alloy anode is normally employed.[111,237,242] Tatsumisago et al. fabricated Na/S ASSBs with S + SE + C as cathode, Na_3PS_4 as solid electrolyte, and $Na_{15}Sn_4$ as anode. The cell delivered a capacity of 1,100 mAh/g based on the weight of S, when tested at a current density of 13 μA/cm^2.[241] The cycling performance of this cell was quite favorable, with the capacity remaining at over 1,000 mAh/g after 25 cycles. These results are illustrated in Figure 9C. Zhang et al. prepared a composite $Se_{0.8}S_{7.2}$@PAN cathode with a Na_3SbS_4 solid electrolyte.[243] The fabricated $Se_{0.8}S_{7.2}$@PAN cathode was dispersed in Na_3SbS_4 aqueous solution and then vacuum dried at 60°C for 24 h. The ASSB with $Se_{0.8}S_{7.2}$@PAN@SE cathode, Na_3SbS_4 solid electrolyte, and $Na_{15}Sn_4$ anode

delivered reversible capacities of 712, 585, 491, 415, and 314 mAh/g at current densities of 73, 146, 292, 438, and 583 mA/g, respectively. By contrast, the capacity of the same cathode prepared by ball milling $Se_{0.8}S_{7.2}$@PAN and SE was below 400 mAh/g at 73mA/g and below 100 mAh/g at 292 mA/g. The difference in performance of the nominally same anode-SSE-cathode architecture has significant implications for understanding the battery design based on Na_3BS_4.

Composite electrolytes hold promise as a method to improve the overall performance. For example, Ci et al. prepared Na_3PS_4-PEO composite electrolyte with improved electrochemical stability against Na metal.[244] The ASSB with TiS_2 + SE cathode, Na_3PS_4-PEO composite electrolyte, and Na anode was cycled 40 times at 20 mA/g and room temperature, retaining 230 mAh/g. In addition to the intrinsic failure modes based on the thermodynamic instability of the SSE at the anode and cathode voltages, capacity loss may also be driven by extrinsic factors such as the quality of the contacts made at the two interfaces. More research on other capacity fade mechanisms for sulfide-based SSEs is important. How much of the observed capacity fade and resistance increase is actually due to contact area loss, etc.? Interfacial modification strategies for improving the cycling stability should be the priority for Na_3AB_4. This system is markedly unstable at both interfaces, and despite its outstanding ionic conductivity, it will have difficulty realizing sustainable high-rate performance in a full battery.

NASICON-TYPE NA SOLID-STATE ELECTROLYTES

Structures and ionic conductivities of NASICON

The stability against Na metal and high-voltage cathodes limits the application of sulfide-based SSEs in high energy density ASSBs. NASICON-type SSEs are more stable than sulfides but display a significantly lower ionic conductivity, thereby limiting the fast-charge performance of ASSB cells. NASICON-type $Na_{1+x}Zr_2P_{3-x}Si_xO_{12}$ ($0 \leq x \leq 3$) was reported as a sodium-ion conductor by Goodenough in 1976.[120] At most compositions, the structure is rhombohedral, except in the range of $1.8 \leq x \leq 2.2$, where a distorted monoclinic space group exists at room temperature. Figures 10A and 10B illustrate the structure of the monoclinic and rhombohedral NASICON, respectively.[246] In both structures, Si^{4+} and P^{5+} occupy the tetrahedral site surrounded by 4 O^{2-} ions, whereas Zr^{4+} takes the octahedral site (6 O^{2-} ions).[247] Figure 10B shows the rhombohedral phase, which contains two Na sites, Na1 at *6b* and Na2 at *18e*.[246] For monoclinic phase, two Na sites would split to three, with Na1 at *4d*, Na2 at *4e*, and Na3 at *8f* (Figure 10A).[246] In both structures, the Na sites are partly occupied, with variable Na concentration.[248] ^{23}Na NMR experiments indicate that the long-range diffusion pathways in NASICON are three-dimensional, whereas the local atomic-scale Na^+ ion motion is two-dimensional.[249] The fitting of ^{23}Na NMR spin-lattice relaxation times (T_1) with a BPP model (3D diffusion) works at a low-temperature region but is poor at HT region. On the other hand, a 2D diffusion model fitting is in good agreement with NMR data, indicating a 2D local ion motion and 3D diffusion path for NASICON.[249] Figure 10C shows the XRD pattern of $Na_3Zr_2PSi_2O_{12}$ at variable temperatures, highlighting the phase transition from monoclinic to rhombohedral structure at about 150°C.[118,246] Impedance measurements also highlight a reversible change in the activation energy from 0.35 eV at room temperature to 0.21 eV at above 150°C, which is associated with the phase transition.[118]

The rhombohedral phase can be stabilized at room temperature by adjusting the Na content, with $x < 1.8$ or $x > 2.2$ in $Na_{1+x}Zr_2P_{3-x}Si_xO_{12}$.[128] Colomban et al.

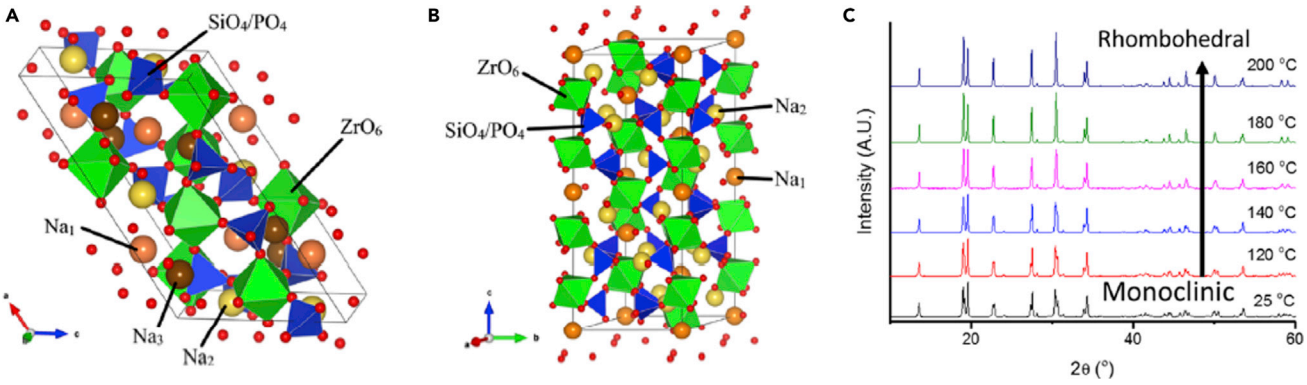

Figure 10. Structures and phase transitions in $Na_3Zr_2Si_2PO_{12}$

(A and B) (A) Low-temperature monoclinic (C2/c) and (B) High-temperature rhombohedral (R-3c) structure of $Na_3Zr_2Si_2PO_{12}$, reprinted from Oh et al.[246] with permission. Copyright 2019, American Chemical Society.

(C) *In-situ*-generated XRD patterns of $Na_3Zr_2Si_2PO_{12}$ up to 200°C.[245]

investigated the lattice change of rhombohedral $Na_{1+x}Zr_2P_{3-x}Si_xO_{12}$ ($0 < x < 3$) at 170°C.[250] Its was observed that with x going from 0 to 3, there is a continuous increase in *a*, going from 8.8 Å to 9.2 Å, whereas *c* increases from 22.8 Å (x = 0) to 23.0 Å (x = 2) and then decreases to 22.3 Å (x = 3). The stability of the rhombohedral phase was then related to the lattice parameter *c*. As *c* approaches 23.0 Å, the distortion along its direction induces the conversion to the monoclinic phase.[250] Cation doping at the Zr^{4+} site also affects the phase transition temperature, such as $Na_{3.2}Y_{0.2}Zr_{1.8}Si_2PO_{12}$ (T_c = 139.5°C) and $Na_{3.2}Co_{0.2}Zr_{1.8}Si_2PO_{12}$ (T_c = 148°C).[121] When the x in $Na_{1+x}Zr_2P_{3-x}Si_xO_{12}$ is equal to 2.4, the structure becomes rhombohedral and the bulk ionic conductivity reaches 15 mS/cm at room temperature. This is comparable with liquid electrolytes. Even with the contribution to grain boundary resistance, the total ionic conductivity can reach 5 mS/cm.[119]

Similar to LLZO solid electrolyte, NASICON solid electrolytes also display a high grain boundary ionic resistance, typically in the 10^3 Ω range.[251] Pores and otherwise poor physical contact between the SSE particles are an important reason for this, with single crystals eliminating the issue.[180] High ionic resistivity also originates from the low purity of the grain boundaries, with single crystals eliminating this issue also. Secondary phases at the grain boundary will significantly affect the grain boundary resistance, in some cases, leading to an improvement in the total ionic conductivity. Luo et al.[252] introduced a secondary phase of Mg-doped $Na_{2.5}Mg_{0.25}PO_4$ with high ionic conductivity of 0.047 mS/cm (300 K) into the grain boundaries of NASICON. As a result, the grain boundary resistance was reduced from 2,000 to 500 Ω. As discussed previously, the side reaction between LLZO and $LiCoO_2$ at high temperatures, and the associated formation of an intermediate reaction layer, dramatically increases the interfacial resistance.[187] In addition, impurities and second phases at grain boundaries may also lead to a higher charge transfer resistance. When sintering at high temperatures, oxide-based SSEs can partially decompose, forming Li_2O in LLZO and Li_3PO_4 in NASICON. For sulfides, it is more feasible to reduce the various ionic resistances through external pressure and a more complete densification.[253]

Reactions of NASICON with Na metal anode

Ab initio simulation indicates that the thermodynamic window of $Na_3Zr_2Si_2PO_{12}$ is from 1.1 to 3.6 V versus Na/Na.[254] This means that any achieved practical stability

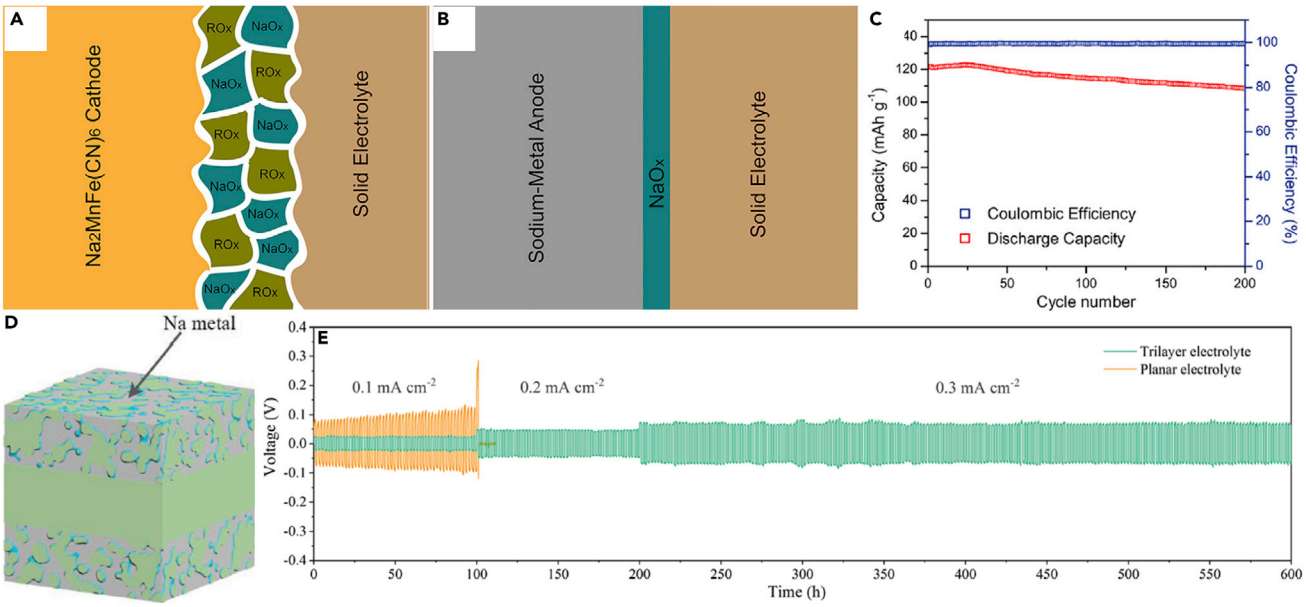

Figure 11. Stability and battery performances of $Na_3Zr_2Si_2PO_{12}$

(A) Schematic illustration of the interfacial reaction products at the $Na_2MnFe(CN)_6$ cathode interface, reprinted from Gao et al.[255] with permission. Copyright 2018, Elsevier Inc.

(B–D) (B) Schematic illustration of the interfacial reaction products at the metal anode interface,[255] (C) Cycling performance of the $Na_2MnFe(CN)_6$/$Na_3Zr_2Si_2PO_{12}$/Na cell at 0.5C rate,[255] (D) Schematic illustration a $Na_3Zr_2Si_2PO_{12}$-based trilayer electrolyte. Reprinted from Lu et al.[249] with permission. Copyright 2019, WILEY-VCH Verlag GmbH & Co. KGaA, Weinheim.

(E) Cycling voltage profiles of the $Na_3Zr_2Si_2PO_{12}$-based trilayer electrolyte, as well as of the baseline conventional $Na_3Zr_2Si_2PO_{12}$-based stack.[230]

against Na metal or ceramic cathodes is a kinetic effect, one that may be enhanced through interfacial modification. Figures 10A and 10B show the decompositions of $Na_{1+x}Zr_2P_{3-x}Si_xO_{12}$ at the Na metal interface and the cathode interface. In both cases the primary constituent is NaO_x, as determined by depth profiling of time-of-flight secondary ion mass spectrometry (TOF-SIMS).[255] The fact that this phase is formed at both anodic and the cathodic voltage indicates that, at least in part, the process is chemically rather than electrochemically driven. The electrical insulator NaO_x suppresses further reaction between NASICON and the electrodes, making the interface relatively stable.[255] At elevated temperatures, $Na_{1+x}Zr_2P_{3-x}Si_xO_{12}$ (x = 2 and 2.2) is more reactive with Na and degrades faster than at ambient temperature.[247] However, extended stability at elevated temperatures is possible. As illustrated in Figure 11C, a solid-state battery based on $Na_2MnFe(CN)_6$/$Na_3Zr_2Si_2PO_{12}$/Na cycled over 200 times at 0.5C at 60°C retained 89.2% of the initial capacity (110 mAh/g).

The interfacial resistance between NASICON and both the Na metal and the cathode is high, being over 1,000 Ω.[230,251,256] In fact, the interfacial resistance between NASICON and Na metal can be more than 10,000 $\Omega \cdot cm^2$.[230] To reduce the interfacial resistance, SnO_2 was coated on the surface of NASCICON by impregnating it with 0.5 M $SnCl_4$ solution and calcining at 500°C in air for 1 h. With the SnO_2 interfacial layer, the wettability of molten Na metal was improved and the interfacial resistance was reduced to 270 $\Omega \cdot cm^2$.[230] Goodenough et al. heat-treated NASICON at 380°C to improve the wettability of the Na metal, resulting in the reduction of interfacial resistance.[256] Without the heat treatment, liquid Na metal remained on the NASICON pellet surface as a nonwetted bead. After heating at 380°C for 3 min, a

black layer on the surface of NASICON was formed. The sodium metal then spread out over the surface of the NASICON pellet, indicating that the black interlayer promotes wetting. XPS analysis combined with XRD indicated that the black layer was an amorphous phase, with Zr^{4+}, P^{5+}, and Si^{4+} reduced by Na metal.[256] After the heat treatment, the total resistance of Na/NASICON/Na symmetric cell decreased from 4,000 Ω to about 350 Ω.[256] Interestingly, when there is an increase in the Si^{4+} content ($Na_{3.4}Zr_2Si_{2.4}P_{0.6}O_{12}$), the interfacial resistance between Na and NASICON is quite low (4.1 $\Omega \cdot cm^2$), which may be due to the wettability effect as well.[119]

Metal dendrite growth with NASICON

The formation of Na metal dendrites in $Na_{1+x}Zr_2P_{3-x}Si_xO_{12}$ has been examined in some detail.[119,230] Similar to LLZO, the grain boundary resistance and interfacial resistance between Na and NASICON plays an important role in dendritic formation. However, with this electrolyte, the dendrite issue seems to be less severe. With a relatively high ionic conductivity of up to 5 mS/cm and low interfacial resistance of 4.1 $\Omega \cdot cm^2$, a symmetrical cell of Na/$Na_{3.4}Zr_2Si_{2.4}P_{0.6}O_{12}$/Na can cycle at a current density of 0.6 mA/cm^2 and total capacity of 1.8 mAh/cm^2 for 300 h, without short circuit and apparent polarization.[119] Figure 11D illustrates the schematic of the trilayer Ca-doped $Na_3Zr_2Si_2PO_{12}$ solid electrolyte, with Na metal infiltrated into the pores.[230] The trilayer solid electrolyte pellets were prepared by a simple compressing method. Corn starch was homogeneously mixed with the NASICON powder with a weight ratio of 60:40 as precursor for the porous layer. The mixture was co-pressed on both sides of the pure NASICON at 120 MPa and then sintered at 1,230°C for 5 h. With SnO_2 coating and improved wettability, Na metal was melted and infiltrated into the porous framework. The porous electrolyte with increased surface area lowered the local current of the plating Na metal on the solid electrolyte and increased the total CCD. Per Figure 11E, the baseline trilayer based on the bulk-type electrolyte will short circuit at 0.1 mA/cm^2 after about 50 cycles. By contrast, the porous electrolyte will survive 300 cycles at 0.3 mA/cm^2 without short circuit.

Reactions of NASICON with the cathode

The interfacial resistance of $Na_3V_2(PO_4)_3$/NASICON/$Na_3V_2(PO_4)_3$ symmetric cell was measured to be about 10,000 Ω.[251] A composite electrode of $Na_3V_2(PO_4)_3$ was prepared by ball milling 49 wt % $Na_3V_2(PO_4)_3$, 49 wt % NASICON, and 2 wt % acetylene black at 200 rpm for 2 h. Polyvinyl alkyl acetate alcohol and 2, 2, 4-trimethyl-2, 4-pentanediol mono isobutyrate binder were added to form an electrode slurry, which was then screen-printed on both sides of NASICON solid electrolyte. Finally, the symmetric cells were sintered by hot pressing at 700°C for 5 h at 65 MPa.[251] As shown in Table 5, the discharge capacity (based on positive electrode) is 60 mAh/g after 2 cycles at 10 μA/cm^2.[251] To reduce the interfacial resistance at the positive electrode, polymer electrolytes may be added, resulting in composite architecture.[255,256] For example, researchers mixed CPMEA/NaTFSI polymer electrolyte with $NaTi_2(PO_4)_3$ cathode.[256] This composite cathode was combined with NASICON and a Na metal anode to create a trilayer. The cell underwent 25 cycles at 65°C, retaining 110 mAh/g. When the current density increased to 1 C, the capacity decreased to 75 mAh/g. The capacity recovered back to 95 mAh/g when the current switched to 0.5 C. A PEO/$NaClO_4$ polymer electrolyte was also added to $Na_2MnFe(CN)_6$ cathode to make a composite cathode layer.[255] Combining with $Na_3Zr_2PSi_2O_{12}$ solid electrolyte and Na anode, this cell demonstrated a favorable discharge capacity of 121 mAh/g at 60°C under 0.5 C for the first cycle, whereas maintaining 108 mAh/g after 200 cycles.[255] The $Na_2MnFe(CN)_6$ cathode cycled in liquid electrolyte (1 M $NaClO_4$ in propylene carbonate (PC): fluoroethylene carbonate (FEC) = 95: 5 volume ratio) delivers a discharge capacity of only 119 mAh/g at the

Table 5. All-solid-state batteries based on NASICON solid electrolytes (NVP represents $Na_3V_2(PO_4)_3$, NVCP represents Cr doped NVP, EC represents ethylene carbonate, DEC represents diethyl carbonate)

Electrolyte	Cathode	Anode	Temperature and current	Loading (mg/cm^2)	Capacity (mAh/g)	Cycles	Ref.
$Na_3Zr_2PSi_2O_{12}$	NVP + SE + C	$Na_3V_2(PO_4)_3$ + SE + C	25°C and 1.2 μA/cm^2	–	60	2	251
$Na_3Zr_2PSi_2O_{12}$	$NaTi_2(PO_4)_3$ + CPMEA + NaTFSI	Na	65°C and 1C	2	75	60	256
$Na_3Zr_2PSi_2O_{12}$	$Na_2MnFe(CN)_6$ + C + PEO + $NaClO_4$	Na	60°C and 0.5 C	3	108	200	255
$Na_{3.2}Ca_{0.1}Zr_{1.9}PSi_2O_{12}$	NVP + C + PEO + SCN + $NaClO_4$	Na in SnO_2 modified porous SE	RT and 1C	8.92	95	500	230
$Na_{3.4}Zr_2P_{0.6}Si_{2.4}O_{12}$	NVP + SE + C and sintered at 750°C	NVP + SE + C and sintered at 750°C	28°C and 0.25 C	0.14–1.4	90	10	119
$Na_3Zr_2PSi_2O_{12}$/PEO-$NaClO_4$ composite	$Na_2MnFe(CN)_6$ + C + PEO-$NaClO_4$	Na	60°C and 0.5 C	3	90	300	257
$Na_3Zr_2PSi_2O_{12}/Na_2B_4O_7$	NVCP + C + PVDF + SCN + $NaClO_4$	Na	RT and 100 mA/g	2–3	75	200	258
$Na_3Zr_2PSi_2O_{12}$	NVP soaked with 1 M $NaClO_4$ in EC/DEC (1:1)	Na	80°C and 0.5 C	–	76	100	259
$Na_{3.4}Zr_{1.9}Zn_{0.1}Si_{2.2}P_{0.8}O_{12}$@poly dopamine	FeS_2 + SE + C	Na	60°C and 0.5C	1	133	300	260

first cycle and decays to only 35 mAh/g after 200 cycles (room temperature and 0.5 C).

Sun et al. mixed $Na_3V_2(PO_4)_3$ and PEO/$NaClO_4$ polymer electrolyte, and extra succinonitrile (SCN) additive.[230] The SCN additive with low melting point (57°C) improves the ion diffusion between electrodes and solid electrolytes, making the ASSB able to cycle at room temperature and high rate of 1 C. The capacity retains 94.9 mAh/g after 500 cycles (Table 5).[230] The above results are presented in Table 5. In general, the advantages and disadvantages of NASICON is similar to LLZO. Both possess high ionic conductivity and good kinetic electrochemical stability. Therefore, future materials design aspects for NASICON research includes interfacial methods to increase the CCD with increasing electrical resistance and ionic conductivity at interfaces and grain boundaries.

Potassium solid-state electrolytes: Direct comparison with sodium and lithium

Due to its large ionic size (1.38 Å), potassium has difficulty migrating in solids. This leads to less possible structures for K solid electrolytes, as shown in Table 6. For Li conductors, the small size of Li^+ ions (0.76 Å) makes for a facile migration through small triangular O_3 metastable sites, which are common in oxides materials.[261] For Na conductors, the larger size of Na^+ (1.02 Å) makes it difficult to diffuse through triangular O_3 metastable sites but possible through quadrangular O_4 sites (β-Al_2O_3,[238] $Na_2Zn_2TeO_6$).[262] Similarly, for K conductors, the K^+ has difficulty in migrating through the quadrangular O_4 sites but may diffuse through hexagonal O_6, e.g., $K_2Fe_4O_7$,[46] or octagonal O_8 sites, e.g., hollandite.[263] These two paths are illustrated in Figures 11B and 12A. The O_6 or O_8 sites, however, are not common in solid oxides and only exist in some special structures. In addition, the O_6 or O_8 sites normally exist in only one or two directions, leading to 1D or 2D conductors. Figure 12C shows the K^+ ion conductivity along *a* axis and *c* axis at variable temperatures.[262] At 350°C, the conductivity along *a* axis is 10^2 S/cm, whereas it is only 10^0 S/cm along *c* axis.[46] In both hollandite and $K_2Fe_4O_7$, adjacent K^+ sites are very close to each other, being 1.14 Å in $K_2Fe_4O_7$ and 2.97 Å in hollandite. The short distance leads to two effects: one is that the adjacent positions cannot be occupied completely, and the other is that ion migration is relatively easier. The ionic conductivity of polycrystalline $K_2Fe_4O_7$ is 50 mS/cm at room temperature.

Table 6. Comparation of Li, Na and K inorganic solid-state electrolytes

Charge carrier	Ion radius	Coordination numbers	Diffusion path	Energy cost for Li/Na stripping (eV/atom)
Li^+	0.76 Å	3 or 4 in sulfides, 4 or 6 in oxides	Triangle	0.259 (001), 0.192 (110), 0.106 (111)
Na^+	1.02 Å	6, 7 or 8	Quadrangle	0.139 (001), 0.183 (110), 0.106 (111)
K^+	1.38 Å	8, 9 or 12	Hexagon	–

The ionic conductivity reaches 350 S/cm along the a axis in a single crystal, with an activation energy of 0.08 eV. Figure 12D illustrates the cyclic voltammetry results of a $K/K_2Fe_4O_7/Pt$ cell, which only shows one pair peak centered at −0.77 and 0.78 V, corresponding to potassium plating and stripping. This indicates that $K_2Fe_4O_7$ is stable at a broad window from 0 V up to 5 V versus K^+/K. Superionic conductivity and good electrochemical stability makes the full cell of $KFeFe(CN)_6/K_2Fe_4O_7/K$ able to cycle at high rates up to 250°C, as illustrated in Figure 12E.

The larger size of Na^+ and K^+ limits the possibilities of oxide-based SSEs. However, the cations with large size and expanded lattice are helpful for obtaining 3D superionic conductors. For Li-NASICON-type SSEs, the cation A in $LiA_2(PO_4)_3$ are Ge^{4+} (0.53 Å) and Ti^{4+} (0.605 Å) with small size, whereas in Na-NASICON, the transition metals change to Zr^{4+} (0.72 Å). This expands the lattice parameter from 8.495 to 9.029 Å (a) and 20.814 to 22.974 Å (c) with the same rhombohedral structure.[112,118] Meanwhile, partly replacing P^{5+} (0.17 Å) by Si^{4+} (0.26 Å) helps to optimize the ionic conductivity in Na-NASICON.[119] The expanded lattice makes it possible for Na^+ to diffuse through triangular O_3 metastable sites. On the other hand, larger size anions or anion clusters would help in the design of superionic conductors for Na^+ and K^+. $LiBH_4$ with BH_4^- anions can form a superionic conductor above 110°C, and this structure can be stabilized at room temperature with 25% LiI doping.[122] However, for $NaBH_4$, no such superionic transition happens before melting.[265] For Na compounds, $Na_2B_{10}H_{10}$ or $Na_2B_{12}H_{12}$ with larger polyanions also show a phase transition at about 100°C. This is illustrated in Figure 12F. The superionic conductivity phase can be stabilized by mixing $B_{12}H_{12}^{2-}$ and $B_{10}H_{10}^{2-}$ ($Na_2(B_{10}H_{10})_{0.5}(B_{12}H_{12})_{0.5}$).[264,266] Similar superionic structure forms when the size of cation and anion are matched, with r_{cation}/r_{anion} approximating to 0.3. Thus, K compounds with larger polyanions, such as $K_2B_nH_n$ ($n > 10$), may exhibit a superionic conductive phase at high temperatures, which could potentially be stabilized at ambient. This remains a highly fruitful but unexplored topic for future research. In addition to larger size, paddle wheel effect with polyanions also promotes fast-ion conduction, which also helps to create fast diffusion path.[106,267]

The requirement for Li, Na, and K SSEs to develop high-performance ASSBs should be similar, such as high ionic conductivity, good chemical/electrochemical stability, and good compatibility to electrode materials. However, most single SSEs do not meet the requirements of high-performance ASSBs. Tailoring SSEs to meet different requirements in various systems is an important way to develop high-performance ASSBs. These include the incorporation of polymer phases to improve the compatibility between oxide SSEs and electrodes; coating oxide ion conductors on cathodes to enhance the electrochemical stability of sulfide SSEs; and SSEs with similar local chemical potential to the cathodes to further decrease the interface electronic resistance. It is well recognized that the larger volume changes associated with Na and K cathodes and the greater reactivity of the Na and K metal anodes both bring about faster cycling-induced failure. For example, Wang et al.[268] calculated and

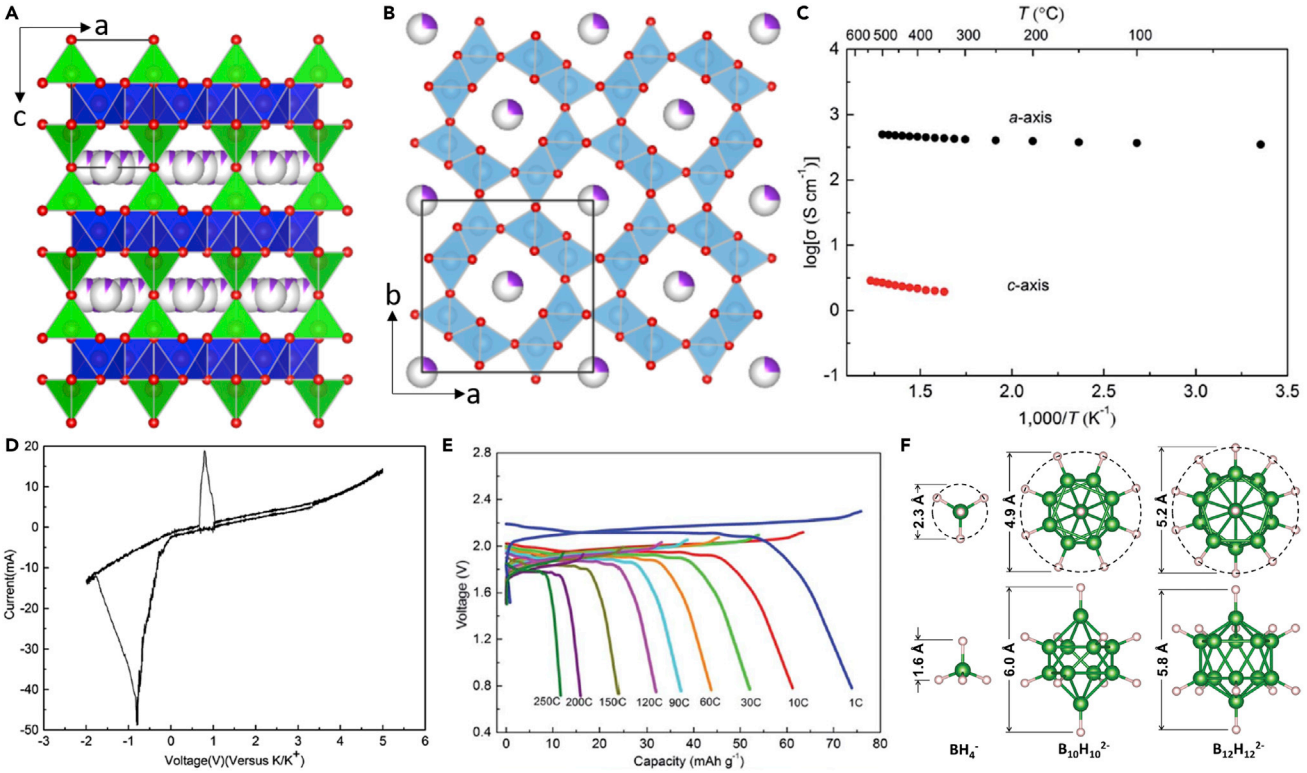

Figure 12. Potassium SSEs and their performance in ASSBs

(A) Structure of $K_2Fe_4O_7$ solid-state electrolyte, reprinted from Yuan et al.,[46] with permission. Copyright 2018, The Royal Society of Chemistry.
(B) Structure of hollandite ($K_xTi_8O_{16}$), reprinted from Feng et al.,[263] with permission.
Copyright 2019, The American Ceramic Society.
(C–F) (C) Arrhenius conductivity plots of $K_2Fe_4O_7$ along the crystallographic a and c axis,[46] (D) cyclic voltammetry curve of the $K/K_2Fe_4O_7$/Pt cell,[46] (E) galvanostatic charge and discharge curves of the $KFe_2(CN)_6/K_2Fe_4O_7$/K cell at different rates,[46] (F) Geometries and approximate relative sizes of BH_4^-, $B_{10}H_{10}^{2-}$, and $B_{12}H_{12}^{2-}$ anions, each shown from top and side views, reprinted from Udovic et al.,[264] with permission. Copyright 2014, WILEY-VCH Verlag GmbH & Co. KGaA, Weinheim.

compared the energy for Li/Na stripping (Table 6). The relatively low energy for Na stripping suggests an easier removal of Na atoms at local spots. This would promote the formation of pinholes during fast discharging, leading to the deterioration of the metal-SSE interface. In general, the Na-based and K-based ASSBs are nowhere near as mature as Li-based ASSBs. Although there are less interfacial modification strategies that are currently available, there is more room for new innovative solutions, some of which may be directly burrowed from the lithium literature.

Future outlook and outstanding research questions

Several key outstanding research questions and potential future research directions are evident. None of the SSEs are thermodynamically stable within the full metal anode-ceramic cathode voltage range. As this review emphasized, the kinetic control of interfaces is of key importance in advancing all SSEs. A parallel key challenge is to quantify the structure and composition of these interfaces for both the anode and cathode, including at the lower voltage S-based cathodes that still react. One general research thrust is to further investigate the structure of the metal dendrites and the associated solid electrolyte interface (SEI). Specifically, it would be fruitful to understand the metal dendrite in SSE growth dynamics as a function of a broader range of electrochemical test parameters than what has been analyzed to date. For example, what are the mechanisms of Li, Na, and potentially K dendrite growth in SSEs at industrially relevant high

current densities, such as 3–5 mA cm^{-2}? It is likely that the fast-charging metal nucleation and growth mechanisms are substantially different than what is obtained at, for example, 0.5 mA cm^{-2}. Moreover, how do the SSE-anode and SSE-cathode interfacial decomposition products evolve with the total plated capacity, extended cycling, test temperature, static aging at open circuit potential (OCP), etc.? The role of anode-SSE and cathode-SSE interfacial modification at this broad range of electrochemical conditions should be further examined as well. It is conceivable that the reaction products at low charging rate, wetting behavior and mechanical integrity of SSE-electrode, metal nucleation dynamics, etc. are modified by high current densities.

The details about the SSE-anode and SSE-cathode structure may be obtained by a combination of post-mortem analysis of the cycled and subsequently disassembled cells, and *in situ*/*operando* methods with dedicated transparent (light optical, conventional and high-energy X-rays, neutrons, etc.) cell architectures. Globally averaged interface structure and chemistry can be obtained by methods such as XPS and TOF-SIMS, whereas local structure can be obtained by site-specific methods such as cryo-stage TEM. Advanced analytical techniques would be useful in further quantifying the various roles that the tuned structure-chemistry interfacial layers may have in promoting stable cycling. Can enhanced electrochemical wetting be directly confirmed at all test conditions and after extended cycling? Site-specific cryo-stage transmission electron microscope (TEM) may be able to uniquely identify SSE heterogeneities that lead to preferential metal dendrite growth at these sites. Other scientific issues to be investigated are the role of localized Joule heating in dendrite and SEI formation, as well as the role of SSE, anode, and cathode in dissipating the heat.[269] SEI and cathode electrolyte interface (CEI) growth are associated with an increase in the interfacial resistance of the electrode, which manifests itself as an overpotential that increases with cycling. During cycling, this polarization is dissipated as localized heat. For the low melting Li, Na, and K metal and their SEI structures, there should be significant localized micro or even nanoscale thermal effects, which warrant further study. Both ion transfer and heat transfer across the SEI requires further modeling and experimental attention.

The mechanical-electrochemical coupling between the multiple SSE phases, as well as between the SSE and anode and cathode are important. More fundamental research is needed there, including the use of emerging nanomechanics methods such inert-atmosphere nanoindentation. These may be used to probe the elastic response, the flow strength, and the toughness and the creep deformation properties of those interfaces. Importantly, these parameters need to be understood not only in the as-synthesized state but also (more importantly and much more challenging) during various stages of lithiation, sodiation, or potassiation. It is expected that at different states of charge, the anode-SSE and cathode-SSE interface will have a distinct set of mechanical properties. This is especially true for the anode-SSE interface in cases, such as when anode-free configuration is employed, when the reservoir of metal is limited, and/or when there is a dynamic reaction layer that is formed at the SSE-anode interface. The community is still struggling to understand the role of creep deformation versus instantaneous toughness in establishing the integrity of the SSE-anode interface. These include the effects of charging rates, cycling temperature, and externally applied stress in both mechanical separation of the cell interfaces, and in the extrusion of dendrites through the SSE.

There appears to be a significant opportunity to incorporate polymers with electrochemical, chemical, and structural functionalities into the SSE architecture. There is work already in this area with ample additional opportunities in terms of novel Li, Na, and K SSE architectures, as well as analytical work to understand the polymers' complex role in improving performance. In a conventional liquid battery, ions move fast

through the cathode particles, which are immersed in the liquid electrolyte. The cathode electrode particles in all-solid-state batteries are separated into isolated individuals by the binder and carbon, which is not conducive to ion transport. The ion transport channels between the cathode particles could be reconstructed by introducing polymer with salt into the cathode architecture. A layer of soft polymer film between the rigid SSE and electrode may also, in parallel, buffer the cycling-induced stresses. Compared with the ceramic solid electrolytes, a flexible ceramic/polymer composite SSEs may be easier to fabricate into a thin membrane with a thickness less than 30 μm, an ideal thickness for practical SSE cells. The ceramic/polymer may also serve as an additional high ionic conductivity interface, potentially boosting the rate performance of the cell. However, it should be noted that a hybrid organic-inorganic SSE may offer compromised performance in terms of reaction stability, ionic flux uniformity, and even dendrite prevention. More work is needed to understand the performance and safety trade-offs in such hybrid systems.

Adding secondary organic-liquid or ionic-liquid electrolytes is another important way to address the electro-mechanical instability between the SSEs and the electrodes,[270] being most utilized for rigid oxide SSE, ceramic cathode interfaces. As summarized in Tables 2 and 5, quasi-solid-state batteries with liquid additives can reach high electrochemical performance, which is more attainable compared with "pure" ASSBs. Although liquid electrolytes can improve the contact between electrodes and solid electrolytes, they also bring additional deleterious interfacial reactions. The charge transfer resistance of the liquid electrolyte/solid electrolyte interface is significant.[270] In order to achieve promising electrochemical performance at variable temperatures, further research is needed on methodologies to reduce these charge transfer resistances. Another point is to reduce the total amount of liquid electrolyte in the ASSB cell so as to improve the overall device safety.

ACKNOWLEDGMENTS

X.F., N.W., J.N., and D.M. (conception of research, preparation of manuscript) were sponsored by Energy Storage Program, Office of Electricity, Department of Energy (grant numbers: DE-AC0500OR22725) USA. P.L. (manuscript co-preparation) was supported by the National Science Foundation, Division of Materials Research, award number 1938833. J.N. and P.J. acknowledge support from Battery Materials Program (BMR), Vehicle Technology Office, Energy Efficiency and Renewable Energy, Department of Energy. H.F. and P.J. (co-conception of research, co-preparation of manuscript) were supported by the U.S. Department of Energy, Office of Basic Energy Sciences, and Division of Materials Sciences and Engineering under award no. DE-FG02-96ER45579 and the U.S. Department of Energy under award no. DE-EE0008865. This research used resources of the National Energy Research Scientific Computing Center; a DOE Office of Science User Facility supported by the Office of Science of the U.S. Department of Energy under contract no. DE-AC02-05CH11231.

DECLARATION OF INTERESTS

The authors declare no competing interests.

REFERENCES

1. Luntz, A. (2015). Beyond lithium ion batteries. J. Phys. Chem. Lett. *6*, 300–301.

2. Nitta, N., Wu, F., Lee, J.T., and Yushin, G. (2015). Li-ion battery materials: present and future. Mater. Today *18*, 252–264.

3. Randau, S., Weber, D.A., Kötz, O., Koerver, R., Braun, P., Weber, A., Ivers-Tiffée, E., Adermann, T., Kulisch, J., Zeier, W.G., et al. (2020). Benchmarking the performance of all-solid-state lithium batteries. Nat. Energy *5*, 259–270.

4. Trahey, L., Brushett, F.R., Balsara, N.P., Ceder, G., Cheng, L., Chiang, Y.-M., Hahn, N.T., Ingram, B.J., Minteer, S.D., Moore, J.S., et al. (2020). Energy storage emerging: a perspective from the Joint Center for Energy Storage Research. Proc. Natl. Acad. Sci. USA *117*, 12550–12557.

5. Li, W., Zhu, J., Xia, Y., Gorji, M.B., and Wierzbicki, T. (2019). Data-driven safety envelope of lithium-ion batteries for electric vehicles. Joule *3*, 2703–2715.

6. Nanda, S., Bhargav, A., and Manthiram, A. (2020). Anode-free, lean-electrolyte lithium-sulfur batteries enabled by tellurium-stabilized lithium deposition. Joule *4*, 1121–1135.

7. Evans, A., Strezov, V., and Evans, T.J. (2012). Assessment of utility energy storage options for increased renewable energy penetration. Renew. Sustain. Energy Rev. *16*, 4141–4147.

8. Famprikis, T., Canepa, P., Dawson, J.A., Islam, M.S., and Masquelier, C. (2019). Fundamentals of inorganic solid-state electrolytes for batteries. Nat. Mater. *18*, 1278–1291.

9. Cano, Z.P., Banham, D., Ye, S., Hintennach, A., Lu, J., Fowler, M., and Chen, Z. (2018). Batteries and fuel cells for emerging electric vehicle markets. Nat. Energy *3*, 279–289.

10. Liu, Y., Zhu, Y., and Cui, Y. (2019). Challenges and opportunities towards fast-charging battery materials. Nat. Energy *4*, 540–550.

11. Schmuch, R., Wagner, R., Hörpel, G., Placke, T., and Winter, M. (2018). Performance and cost of materials for lithium-based rechargeable automotive batteries. Nat. Energy *3*, 267–278.

12. Choi, J.W., and Aurbach, D. (2016). Promise and reality of post-lithium-ion batteries with high energy densities. Nat. Rev. Mater. *1*, 16013.

13. Olivetti, E.A., Ceder, G., Gaustad, G.G., and Fu, X. (2017). Lithium-ion battery supply chain considerations: analysis of potential bottlenecks in critical metals. Joule *1*, 229–243.

14. Qiao, Y., Deng, H., He, P., and Zhou, H. (2020). A 500 Wh/kg lithium-metal cell based on anionic redox. Joule *4*, 1445–1458.

15. Yu, Z., Wang, H., Kong, X., Huang, W., Tsao, Y., Mackanic, D.G., Wang, K., Wang, X., Huang, W., Choudhury, S., et al. (2020). Molecular design for electrolyte solvents enabling energy-dense and long-cycling lithium metal batteries. Nat. Energy *5*, 526–533.

16. Kuhn, A., Kunze, M., Sreeraj, P., Wiemhöfer, H.-D., Thangadurai, V., Wilkening, M., and Heitjans, P. (2012). NMR relaxometry as a versatile tool to study Li ion dynamics in potential battery materials. Solid State Nucl. Magn. Reson. *42*, 2–8.

17. Liu, P., and Mitlin, D. (2020). Emerging potassium metal anodes: perspectives on control of the electrochemical interfaces. Acc. Chem. Res. *53*, 1161–1175.

18. Sun, B., Xiong, P., Maitra, U., Langsdorf, D., Yan, K., Wang, C., Janek, J., Schröder, D., and Wang, G. (2020). Design strategies to enable the efficient use of sodium metal anodes in high-energy batteries. Adv. Mater. *32*, 1903891.

19. Cheng, X.-B., Zhang, R., Zhao, C.-Z., and Zhang, Q. (2017). Toward safe lithium metal anode in rechargeable batteries: a review. Chem. Rev. *117*, 10403–10473.

20. Sun, H., Zhu, G., Xu, X., Liao, M., Li, Y.-Y., Angell, M., Gu, M., Zhu, Y., Hung, W.H., Li, J., et al. (2019). A safe and non-flammable sodium metal battery based on an ionic liquid electrolyte. Nat. Commun. *10*, 3302.

21. Casimir, A., Zhang, H., Ogoke, O., Amine, J.C., Lu, J., and Wu, G. (2016). Silicon-based anodes for lithium-ion batteries: effectiveness of materials synthesis and electrode preparation. Nano Energy *27*, 359–376.

22. Xu, J., Dou, Y., Wei, Z., Ma, J., Deng, Y., Li, Y., Liu, H., and Dou, S. (2017). Recent progress in graphite intercalation compounds for rechargeable metal (Li, Na, K, Al)-ion batteries. Adv. Sci. *4*, 1700146.

23. Ruther, R.E., Hays, K.A., An, S.J., Li, J., Wood, D.L., and Nanda, J. (2018). Chemical evolution in silicon–graphite composite anodes investigated by vibrational spectroscopy. ACS Appl. Mater. Interfaces *10*, 18641–18649.

24. Kumar, S.K., Ghosh, S., Malladi, S.K., Nanda, J., and Martha, S.K. (2018). Nanostructured silicon–carbon 3D electrode architectures for high-performance lithium-ion batteries. ACS Omega *3*, 9598–9606.

25. Kasemchainan, J., Zekoll, S., Spencer Jolly, D., Ning, Z., Hartley, G.O., Marrow, J., and Bruce, P.G. (2019). Critical stripping current leads to dendrite formation on plating in lithium anode solid electrolyte cells. Nat. Mater. *18*, 1105–1111.

26. Han, F., Westover, A.S., Yue, J., Fan, X., Wang, F., Chi, M., Leonard, D.N., Dudney, N.J., Wang, H., and Wang, C. (2019). High electronic conductivity as the origin of lithium dendrite formation within solid electrolytes. Nat. Energy *4*, 187–196.

27. Sun, Y.-K. (2020). Promising all-solid-state batteries for future electric vehicles. ACS Energy Lett. *5*, 3221–3223.

28. Cao, D., Sun, X., Li, Q., Natan, A., Xiang, P., and Zhu, H. (2020). Lithium dendrite in all-solid-state batteries: growth mechanisms, suppression strategies, and characterizations. Matter *3*, 57–94.

29. Kato, Y., Hori, S., Saito, T., Suzuki, K., Hirayama, M., Mitsui, A., Yonemura, M., Iba, H., and Kanno, R. (2016). High-power all-solid-state batteries using sulfide superionic conductors. Nat. Energy *1*, 16030.

30. Lee, Y.-G., Fujiki, S., Jung, C., Suzuki, N., Yashiro, N., Omoda, R., Ko, D.-S., Shiratsuchi, T., Sugimoto, T., Ryu, S., et al. (2020). High-energy long-cycling all-solid-state lithium metal batteries enabled by silver–carbon composite anodes. Nat. Energy *5*, 299–308.

31. Wang, Y., Richards, W.D., Ong, S.P., Miara, L.J., Kim, J.C., Mo, Y., and Ceder, G. (2015). Design principles for solid-state lithium superionic conductors. Nat. Mater. *14*, 1026–1031.

32. Krauskopf, T., Richter, F.H., Zeier, W.G., and Janek, J. (2020). Physicochemical concepts of the lithium metal anode in solid-state batteries. Chem. Rev. *120*, 7745–7794.

33. Gao, Y., Nolan, A.M., Du, P., Wu, Y., Yang, C., Chen, Q., Mo, Y., and Bo, S.-H. (2020). Classical and emerging characterization techniques for investigation of ion transport mechanisms in crystalline fast ionic conductors. Chem. Rev. *120*, 5954–6008.

34. Banerjee, A., Wang, X., Fang, C., Wu, E.A., and Meng, Y.S. (2020). Interfaces and interphases in all-solid-state batteries with inorganic solid electrolytes. Chem. Rev. *120*, 6878–6933.

35. Nolan, A.M., Zhu, Y., He, X., Bai, Q., and Mo, Y. (2018). Computation-accelerated design of materials and interfaces for all-solid-state lithium-ion batteries. Joule *2*, 2016–2046.

36. Bao, C., Wang, B., Liu, P., Wu, H., Zhou, Y., Wang, D., Liu, H., and Dou, S. (2020). Solid electrolyte interphases on sodium metal anodes. Adv. Funct. Mater. *30*, 2004891.

37. Cui, G. (2020). Reasonable design of high-energy-density solid-state lithium-metal batteries. Matter *2*, 805–815.

38. Kalaga, K., Rodrigues, M.-T.F., Gullapalli, H., Babu, G., Arava, L.M.R., and Ajayan, P.M. (2015). Quasi-solid electrolytes for high temperature lithium ion batteries. ACS Appl. Mater. Interfaces *7*, 25777–25783.

39. Jaumaux, P., Wu, J., Shanmukaraj, D., Wang, Y., Zhou, D., Sun, B., Kang, F., Li, B., Armand, M., and Wang, G. (2021). Non-flammable liquid and quasi-solid electrolytes toward highly-safe alkali metal-based batteries. Adv. Funct. Mater. *31*, 2008644.

40. Guo, X., Bae, J., Ding, Y., Zhang, X., and Yu, G. (2021). Liquid alloy enabled solid-state batteries for conformal electrode–electrolyte interfaces. Adv. Funct. Mater. *31*, 2010863.

41. Gao, X., Zheng, X., Wang, J., Zhang, Z., Xiao, X., Wan, J., Ye, Y., Chou, L.-Y., Lee, H.K., Wang, J., et al. (2020). Incorporating the nanoscale encapsulation concept from liquid electrolytes into solid-state lithium–sulfur batteries. Nano Lett. *20*, 5496–5503.

42. Wang, C., Fu, K., Kammampata, S.P., McOwen, D.W., Samson, A.J., Zhang, L., Hitz, G.T., Nolan, A.M., Wachsman, E.D., Mo, Y., et al. (2020). Garnet-type solid-state electrolytes: materials, interfaces, and batteries. Chem. Rev. *120*, 4257–4300.

43. Ding, Y.-L., Kopold, P., Hahn, K., van Aken, P.A., Maier, J., and Yu, Y. (2016). Facile solid-state growth of 3D well-interconnected nitrogen-rich carbon nanotube–graphene hybrid architectures for lithium–sulfur batteries. Adv. Funct. Mater. *26*, 1112–1119.

44. Pang, Y., Pan, J., Yang, J., Zheng, S., and Wang, C. (2021). Electrolyte/electrode interfaces in all-solid-state lithium batteries: a review. Electrochem. Energ. Rev. *4*, 169–193.

45. Bae, J., Zhang, X., Guo, X., and Yu, G. (2021). A general strategy of anion-rich high-concentration polymeric interlayer for high-voltage, all-solid-state batteries. Nano Lett. *21*, 1184–1191.

46. Yuan, H., Li, H., Zhang, T., Li, G., He, T., Du, F., and Feng, S. (2018). A $K_2Fe_4O_7$ superionic conductor for all-solid-state potassium metal batteries. J. Mater. Chem. A *6*, 8413–8418.

47. Fuchs, T., Culver, S.P., Till, P., and Zeier, W.G. (2020). Defect-mediated conductivity enhancements in $Na_{3-x}Pn_{1-x}W_xS_4$ (Pn = P, Sb) using aliovalent substitutions. ACS Energy Lett. *5*, 146–151.

48. Hayashi, A., Masuzawa, N., Yubuchi, S., Tsuji, F., Hotehama, C., Sakuda, A., and Tatsumisago, M. (2019). A sodium-ion sulfide solid electrolyte with unprecedented conductivity at room temperature. Nat. Commun. *10*, 5266.

49. Dollé, M., Sannier, L., Beaudoin, B., Trentin, M., and Tarascon, J.-M. (2002). Live scanning electron microscope observations of dendritic growth in lithium/polymer cells. Electrochem. Solid-State Lett. *5*, A286–A289.

50. Jung, W.D., Jeon, M., Shin, S.S., Kim, J.-S., Jung, H.-G., Kim, B.-K., Lee, J.-H., Chung, Y.-C., and Kim, H. (2020). Functionalized sulfide solid electrolyte with air-stable and chemical-resistant oxysulfide nanolayer for all-solid-state batteries. ACS Omega *5*, 26015–26022.

51. Wang, H., Chen, Y., Hood, Z.D., Sahu, G., Pandian, A.S., Keum, J.K., An, K., and Liang, C. (2016). An air-stable Na_3SbS_4 superionic conductor prepared by a rapid and economic synthetic procedure. Angew. Chem. *128*, 8693–8697.

52. Zhao, F., Alahakoon, S.H., Adair, K., Zhang, S., Xia, W., Li, W., Yu, C., Feng, R., Hu, Y., Liang, J., et al. (2021). An air-stable and Li-metal-compatible glass-ceramic electrolyte enabling high-performance all-solid-state Li metal batteries. Adv. Mater. *33*, 2006577.

53. Liang, J., Chen, N., Li, X., Li, X., Adair, K.R., Li, J., Wang, C., Yu, C., Norouzi Banis, M., Zhang, L., et al. (2020). $Li_{10}Ge(P_{1-x}Sb_x)_2S_{12}$ lithium-ion conductors with enhanced atmospheric stability. Chem. Mater. *32*, 2664–2672.

54. Karasulu, B., Emge, S.P., Groh, M.F., Grey, C.P., and Morris, A.J. (2020). Al/Ga-doped $Li_7La_3Zr_2O_{12}$ garnets as Li-ion solid-state battery electrolytes: atomistic insights into local coordination environments and their influence on ^{17}O, ^{27}Al, and ^{71}Ga NMR spectra. J. Am. Chem. Soc. *142*, 3132–3148.

55. Sheng, O., Jin, C., Ding, X., Liu, T., Wan, Y., Liu, Y., Nai, J., Wang, Y., Liu, C., and Tao, X. (2021). A decade of progress on solid-state electrolytes for secondary batteries: advances and contributions. Adv. Funct. Mater. *31*, 2100891.

56. Wang, C., Liang, J., Zhao, Y., Zheng, M., Li, X., and Sun, X. (2021). All-solid-state lithium batteries enabled by sulfide electrolytes: from fundamental research to practical engineering design. Energy Environ. Sci. *14*, 2577–2619.

57. Lu, Y., Zhao, C.-Z., Yuan, H., Cheng, X.-B., Huang, J.-Q., and Zhang, Q. (2021). Critical current density in solid-state lithium metal batteries: mechanism, influences, and strategies. Adv. Funct. Mater. *31*, 2009925.

58. Gao, W., Singh, N., Song, L., Liu, Z., Reddy, A.L.M., Ci, L., Vajtai, R., Zhang, Q., Wei, B., and Ajayan, P.M. (2011). Direct laser writing of micro-supercapacitors on hydrated graphite oxide films. Nat. Nanotechnol. *6*, 496–500.

59. Ashby, D.S., Choi, C.S., Edwards, M.A., Talin, A.A., White, H.S., and Dunn, B.S. (2020). High-performance solid-state lithium-ion battery with mixed 2D and 3D electrodes. ACS Appl. Energy Mater. *3*, 8402–8409.

60. Lang, J., Jin, Y., Liu, K., Long, Y., Zhang, H., Qi, L., Wu, H., and Cui, Y. (2020). High-purity electrolytic lithium obtained from low-purity sources using solid electrolyte. Nat. Sustain. *3*, 386–390.

61. Chen, C., Jiang, M., Zhou, T., Raijmakers, L., Vezhlev, E., Wu, B., Schülli, T.U., Danilov, D.L., Wei, Y., Eichel, R.-A., and Notten, P.H.L. (2021). Interface aspects in all-solid-state Li-based batteries reviewed. Adv. Energy Mater. *11*, 2003939.

62. Wang, H., Zhu, J., Su, Y., Gong, Z., and Yang, Y. (2021). Interfacial compatibility issues in rechargeable solid-state lithium metal batteries: a review. Sci. China Chem. *64*, 879–898.

63. Meng, N., Lian, F., and Cui, G. (2021). Macromolecular design of lithium conductive polymer as electrolyte for solid-state lithium batteries. Small *17*, 2005762.

64. Dwibedi, D., Araujo, R.B., Chakraborty, S., Shanbogh, P.P., Sundaram, N.G., Ahuja, R., and Barpanda, P. (2015). $Na_{2.44}Mn_{1.79}(SO_4)_3$: a new member of the alluaudite family of insertion compounds for sodium ion batteries. J. Mater. Chem. A *3*, 18564–18571.

65. Zhang, Z., Shao, Y., Lotsch, B., Hu, Y.-S., Li, H., Janek, J., Nazar, L.F., Nan, C.-W., Maier, J., Armand, M., and Chen, L. (2018). New horizons for inorganic solid state ion conductors. Energy Environ. Sci. *11*, 1945–1976.

66. Pervez, S.A., Kim, G., Vinayan, B.P., Cambaz, M.A., Kuenzel, M., Hekmatfar, M., Fichtner, M., and Passerini, S. (2020). Overcoming the interfacial limitations imposed by the solid–solid interface in solid-state batteries using ionic liquid-based interlayers. Small *16*, 2000279.

67. Zhou, D., Shanmukaraj, D., Tkacheva, A., Armand, M., and Wang, G. (2019). Polymer electrolytes for lithium-based batteries: advances and prospects. Chem *5*, 2326–2352.

68. Xia, S., Wu, X., Zhang, Z., Cui, Y., and Liu, W. (2019). Practical challenges and future perspectives of all-solid-state lithium-metal batteries. Chem *5*, 753–785.

69. Yang, C., Fu, K., Zhang, Y., Hitz, E., and Hu, L. (2017). Protected lithium-metal anodes in batteries: from liquid to solid. Adv. Mater. *29*, 1701169.

70. Zheng, F., Kotobuki, M., Song, S., Lai, M.O., and Lu, L. (2018). Review on solid electrolytes for all-solid-state lithium-ion batteries. J. Power Sources *389*, 198–213.

71. Zhao, W., Yi, J., He, P., and Zhou, H. (2019). Solid-state electrolytes for lithium-ion batteries: fundamentals, challenges and perspectives. Electrochem. Energ. Rev. *2*, 574–605.

72. Lau, J., DeBlock, R.H., Butts, D.M., Ashby, D.S., Choi, C.S., and Dunn, B.S. (2018). Sulfide solid electrolytes for lithium battery applications. Adv. Energy Mater. *8*, 1800933.

73. Zhang, Q., Cao, D., Ma, Y., Natan, A., Aurora, P., and Zhu, H. (2019). Sulfide-based solid-state electrolytes: synthesis, stability, and potential for all-solid-state batteries. Adv. Mater. *31*, 1901131.

74. Choi, C.S., Lau, J., Hur, J., Smith, L., Wang, C., and Dunn, B. (2018). Synthesis and properties of a photopatternable lithium-ion conducting solid electrolyte. Adv. Mater. *30*, 1703772.

75. Ma, J., Li, Y., Grundish, N.S., Goodenough, J.B., Chen, Y., Guo, L., Peng, Z., Qi, X., Yang, F., Qie, L., et al. (2021). The 2021 battery technology roadmap. J. Phys. D: Appl. Phys. *54*, 183001.

76. Wang, X., Kerr, R., Chen, F., Goujon, N., Pringle, J.M., Mecerreyes, D., Forsyth, M., and Howlett, P.C. (2020). Toward high-energy-density lithium metal batteries: opportunities and challenges for solid organic electrolytes. Adv. Mater. *32*, 1905219.

77. Dudney, N.J. (2005). Solid-state thin-film rechargeable batteries. Mater. Sci. Eng. B *116*, 245–249.

78. Qi, Y., Ban, C., and Harris, S.J. (2020). A new general paradigm for understanding and preventing Li metal penetration through solid electrolytes. Joule *4*, 2599–2608.

79. Zhao, Y., Zheng, K., and Sun, X. (2018). Addressing interfacial issues in liquid-based and solid-state batteries by atomic and molecular layer deposition. Joule *2*, 2583–2604.

80. Tan, D.H.S., Banerjee, A., Chen, Z., and Meng, Y.S. (2020). From nanoscale interface characterization to sustainable energy storage using all-solid-state batteries. Nat. Nanotechnol. *15*, 170–180.

81. Lou, S., Zhang, F., Fu, C., Chen, M., Ma, Y., Yin, G., and Wang, J. (2021). Interface issues and challenges in all-solid-state batteries: lithium, sodium, and beyond. Adv. Mater. *33*, 2000721.

82. Xu, L., Tang, S., Cheng, Y., Wang, K., Liang, J., Liu, C., Cao, Y.-C., Wei, F., and Mai, L. (2018). Interfaces in solid-state lithium batteries. Joule *2*, 1991–2015.

83. Huang, K.J., Ceder, G., and Olivetti, E.A. (2021). Manufacturing scalability implications of materials choice in inorganic solid-state batteries. Joule *5*, 564–580.

84. Judez, X., Eshetu, G.G., Li, C., Rodriguez-Martinez, L.M., Zhang, H., and Armand, M. (2018). Opportunities for rechargeable solid-state batteries based on Li-intercalation cathodes. Joule *2*, 2208–2224.

85. Duffner, F., Kronemeyer, N., Tübke, J., Leker, J., Winter, M., and Schmuch, R. (2021). Post-lithium-ion battery cell production and its compatibility with lithium-ion cell production infrastructure. Nat. Energy *6*, 123–134.

86. Balaish, M., Gonzalez-Rosillo, J.C., Kim, K.J., Zhu, Y., Hood, Z.D., and Rupp, J.L.M. (2021). Processing thin but robust electrolytes for solid-state batteries. Nat. Energy *6*, 227–239.

87. Zhao, N., Khokhar, W., Bi, Z., Shi, C., Guo, X., Fan, L.-Z., and Nan, C.-W. (2019). Solid garnet batteries. Joule *3*, 1190–1199.

88. Abakumov, A.M., Fedotov, S.S., Antipov, E.V., and Tarascon, J.-M. (2020). Solid state chemistry for developing better metal-ion batteries. Nat. Commun. *11*, 4976.

89. Shen, Y., Zhang, Y., Han, S., Wang, J., Peng, Z., and Chen, L. (2018). Unlocking the energy capabilities of lithium metal electrode with solid-state electrolytes. Joule *2*, 1674–1689.

90. Nanda, J., Wang, C., and Liu, P. (2018). Frontiers of solid-state batteries. MRS Bull. *43*, 740–745.

91. Albertus, P., Anandan, V., Ban, C., Balsara, N., Belharouak, I., Buettner-Garrett, J., Chen, Z., Daniel, C., Doeff, M., Dudney, N.J., et al. (2021). Challenges for and pathways toward Li-metal-based all-solid-state batteries. ACS Energy Lett. 1399–1404.

92. Eshetu, G.G., Elia, G.A., Armand, M., Forsyth, M., Komaba, S., Rojo, T., and Passerini, S. (2020). Electrolytes and interphases in sodium-based rechargeable batteries: recent advances and perspectives. Adv. Energy Mater. *10*, 2000093.

93. Wang, M.J., Kazyak, E., Dasgupta, N.P., and Sakamoto, J. (2021). Transitioning solid-state batteries from lab to market: linking electro-chemo-mechanics with practical considerations. Joule *5*, 1371–1390.

94. Jia, M., Zhao, N., Huo, H., and Guo, X. (2020). Comprehensive investigation into garnet electrolytes toward application-oriented solid lithium batteries. Electrochem. Energ. Rev. *3*, 656–689.

95. Yu, C., Zhao, F., Luo, J., Zhang, L., and Sun, X. (2021). Recent development of lithium argyrodite solid-state electrolytes for solid-state batteries: synthesis, structure, stability and dynamics. Nano Energy *83*, 105858.

96. N.J. Dudney, W.C. West, and J. Nanda, eds. (2015). In Handbook of Solid State Batteries, *6* (World Scientific).

97. Brahmbhatt, T., Yang, G., Self, E., and Nanda, J. (2020). Cathode–sulfide solid electrolyte interfacial instability: challenges and solutions. Front. Energy Res. *8*, 247.

98. Sacci, R.L., Bennett, T.H., Drews, A.R., Anandan, V., Kirkham, M.J., Daemen, L.L., and Nanda, J. (2021). Phase evolution during lithium–indium halide superionic conductor dehydration. J. Mater. Chem. A *9*, 990–996.

99. Ong, S.P., Mo, Y., Richards, W.D., Miara, L., Lee, H.S., and Ceder, G. (2013). Phase stability, electrochemical stability and ionic conductivity of the Li 10±1 MP_2 X12 (M = Ge, Si, Sn, Al or P, and X = O, S or Se) family of superionic conductors. Energy Environ. Sci. *6*, 148–156.

100. Zhao, Y., and Daemen, L.L. (2012). Superionic conductivity in lithium-rich anti-perovskites. J. Am. Chem. Soc. *134*, 15042–15047.

101. Fang, H., Wang, S., Liu, J., Sun, Q., and Jena, P. (2017). Superhalogen-based lithium superionic conductors. J. Mater. Chem. A *5*, 13373–13381.

102. Fang, H., and Jena, P. (2019). Sodium superionic conductors based on clusters. ACS Appl. Mater. Interfaces *11*, 963–972.

103. He, X., Zhu, Y., and Mo, Y. (2017). Origin of fast ion diffusion in super-ionic conductors. Nat. Commun. *8*, 15893.

104. Kozinsky, B. (2018). Transport in frustrated and disordered solid electrolytes. In Handbook of Materials Modeling, W. Andreoni and S. Yip, eds. (Springer International Publishing), pp. 1–20.

105. Fang, H., and Jena, P. (2017). Li-rich antiperovskite superionic conductors based on cluster ions. Proc. Natl. Acad. Sci. USA *114*, 11046–11051.

106. Zhang, Z., Li, H., Kaup, K., Zhou, L., Roy, P.-N., and Nazar, L.F. (2020). Targeting superionic conductivity by turning on anion rotation at room temperature in fast ion conductors. Matter *2*, 1667–1684.

107. Kweon, K.E., Varley, J.B., Shea, P., Adelstein, N., Mehta, P., Heo, T.W., Udovic, T.J., Stavila, V., and Wood, B.C. (2017). Structural, chemical, and dynamical frustration: origins of superionic conductivity in *closo* -borate solid electrolytes. Chem. Mater. *29*, 9142–9153.

108. Dove, M.T. (2003). Structure and dynamics – an atomic view of materials. Mater. Today *6*, 59.

109. Hull, S. (2004). Superionics: crystal structures and conduction processes. Rep. Prog. Phys. *67*, 1233–1314.

110. Schmitz, K.S. (2017). Solid state. In Physical Chemistry (Elsevier), pp. 261–290.

111. Chu, I.-H., Kompella, C.S., Nguyen, H., Zhu, Z., Hy, S., Deng, Z., Meng, Y.S., and Ong, S.P. (2016). Room-temperature all-solid-state rechargeable sodium-ion batteries with a Cl-doped Na3PS4 superionic conductor. Sci. Rep. *6*, 33733.

112. Wang, S., Ding, Y., Zhou, G., Yu, G., and Manthiram, A. (2016). Durability of the $Li_{1+x}Ti_{2-x}Al_x(PO_4)_3$ solid electrolyte in Li-S batteries. ACS Energy Lett. *1*, 1080–1085.

113. Mo, Y., Ong, S.P., and Ceder, G. (2012). First principles study of the Li $_{10}$ GeP $_2$ S $_{12}$ lithium super ionic conductor material. Chem. Mater. *24*, 15–17.

114. Famprikis, T., Dawson, J.A., Fauth, F., Clemens, O., Suard, E., Fleutot, B., Courty, M., Chotard, J.-N., Islam, M.S., and Masquelier, C. (2019). A new superionic plastic polymorph of the Na+ conductor Na3PS4. ACS Materials Lett. *1*, 641–646.

115. Kong, S.-T., Deiseroth, H.-J., Reiner, C., Gün, O., Neumann, E., Ritter, C., and Zahn, D. (2010). Lithium argyrodites with phosphorus and arsenic: order and disorder of lithium atoms, crystal chemistry, and phase transitions. Chemistry *16*, 2198–2206.

116. Deiseroth, H.-J., Kong, S.-T., Eckert, H., Vannahme, J., Reiner, C., Zaiss, T., and Schlosser, M. (2008). Li6PS5X: a class of crystalline Li-rich solids With an unusually high Li^+ mobility. Angew. Chem. Int. Ed. Engl. *47*, 755–758.

117. Zhang, Z., Sun, Y., Duan, X., Peng, L., Jia, H., Zhang, Y., Shan, B., and Xie, J. (2019). Design and synthesis of room temperature stable Li-argyrodite superionic conductors *via* cation doping. J. Mater. Chem. A *7*, 2717–2722.

118. von Alpen, U., Bell, M.F., and Wichelhaus, W. (1979). Phase transition in NASICON ($Na_3Zr_2Si_2PO_{12}$). Mater. Res. Bull. *14*, 1317–1322.

119. Ma, Q., Tsai, C.-L., Wei, X.-K., Heggen, M., Tietz, F., and Irvine, J.T.S. (2019). Room temperature demonstration of a sodium superionic conductor with grain conductivity in excess of 0.01 S cm^{-1} and its primary applications in symmetric battery cells. J. Mater. Chem. A *7*, 7766–7776.

120. Goodenough, J.B., Hong, H.Y.-P., and Kafalas, J.A. (1976). Fast Na+-ion transport in skeleton structures. Mater. Res. Bull. *11*, 203–220.

121. Jolley, A.G., Taylor, D.D., Schreiber, N.J., and Wachsman, E.D. (2015). Structural investigation of monoclinic-rhombohedral phase transition in $Na_3Zr_2Si_2PO_{12}$ and doped NASICON. J. Am. Ceram. Soc. *98*, 2902–2907.

122. Maekawa, H., Matsuo, M., Takamura, H., Ando, M., Noda, Y., Karahashi, T., and Orimo, S. (2009). Halide-stabilized $LiBH_4$, a room-temperature lithium fast-ion conductor. J. Am. Chem. Soc. *131*, 894–895.

123. Filinchuk, Y., Chernyshov, D., and Cerny, R. (2008). Lightest borohydride probed by synchrotron X-ray diffraction: experiment calls for a new theoretical revision. J. Phys. Chem. C *112*, 10579–10584.

124. Jansen, M., and Henseler, U. (1992). Synthesis, structure determination, and ionic conductivity of sodium tetrathiophosphate. J. Solid State Chem. *99*, 110–119.

125. Nishimura, S., Tanibata, N., Hayashi, A., Tatsumisago, M., and Yamada, A. (2017). The crystal structure and sodium disorder of high-temperature polymorph β-Na3PS4. J. Mater. Chem. A *5*, 25025–25030.

126. Zhang, Q., Zhang, C., Hood, Z.D., Chi, M., Liang, C., Jalarvo, N.H., Yu, M., and Wang, H. (2020). Abnormally low activation energy in cubic Na3SbS4 superionic conductors. Chem. Mater. *32*, 2264–2271.

127. Zhang, L., Yang, K., Mi, J., Lu, L., Zhao, L., Wang, L., Li, Y., and Zeng, H. (2015). Na3PSe4: a novel chalcogenide solid electrolyte with high ionic conductivity. Adv. Energy Mater. *5*, 1501294.

128. Song, A.-Y., Xiao, Y., Turcheniuk, K., Upadhya, P., Ramanujapuram, A., Benson, J., Magasinski, A., Olguin, M., Meda, L., Borodin, O., and Yushin, G. (2018). Protons enhance conductivities in lithium halide hydroxide/lithium oxyhalide solid electrolytes by forming rotating hydroxy groups. Adv. Energy Mater. *8*, 1700971.

129. Adams, S., and Rao, R.P. (2012). Ion transport and phase transition in $Li_{7-x}La_3(Zr_{2-x}M_x)O_{12}$ (M = Ta^{5+}, Nb^{5+}, x = 0, 0.25). J. Mater. Chem. *22*, 1426–1434.

130. Awaka, J., Kijima, N., Hayakawa, H., and Akimoto, J. (2009). Synthesis and structure analysis of tetragonal $Li_7La_3Zr_2O_{12}$ with the garnet-related type structure. J. Solid State Chem. *182*, 2046–2052.

131. Geiger, C.A., Alekseev, E., Lazic, B., Fisch, M., Armbruster, T., Langner, R., Fechtelkord, M., Kim, N., Pettke, T., and Weppner, W. (2011).

Crystal chemistry and stability of "$Li_7La_3Zr_2O_{12}$" garnet: a fast lithium-ion conductor. Inorg. Chem. *50*, 1089–1097.

132. Kamaya, N., Homma, K., Yamakawa, Y., Hirayama, M., Kanno, R., Yonemura, M., Kamiyama, T., Kato, Y., Hama, S., Kawamoto, K., and Mitsui, A. (2011). A lithium superionic conductor. Nat. Mater. *10*, 682–686.

133. Chamorro, J.R., and McQueen, T.M. (2018). Progress toward solid state synthesis by design. Acc. Chem. Res. *51*, 2918–2925.

134. Makiura, R., Yonemura, T., Yamada, T., Yamauchi, M., Ikeda, R., Kitagawa, H., Kato, K., and Takata, M. (2009). Size-controlled stabilization of the superionic phase to room temperature in polymer-coated AgI nanoparticles. Nat. Mater. *8*, 476–480.

135. Blanchard, D., Nale, A., Sveinbjörnsson, D., Eggenhuisen, T.M., Verkuijlen, M.H.W., Suwarno, V., Vegge, T., Kentgens, A.P.M., and de Jongh, P.E. (2015). Nanoconfined $LiBH_4$ as a fast lithium ion conductor. Adv. Funct. Mater. *25*, 184–192.

136. Ngene, P., Lambregts, S.F.H., Blanchard, D., Vegge, T., Sharma, M., Hagemann, H., and de Jongh, P.E. (2019). The influence of silica surface groups on the Li-ion conductivity of $LiBH_4/SiO_2$ nanocomposites. Phys. Chem. Chem. Phys. *21*, 22456–22466.

137. Liu, Z., Fu, W., Payzant, E.A., Yu, X., Wu, Z., Dudney, N.J., Kiggans, J., Hong, K., Rondinone, A.J., and Liang, C. (2013). Anomalous high ionic conductivity of nanoporous β-Li_3PS_4. J. Am. Chem. Soc. *135*, 975–978.

138. Choi, Y.S., Lee, Y.-S., Oh, K.H., and Cho, Y.W. (2016). Interface-enhanced Li ion conduction in a LiBH4–SiO_2 solid electrolyte. Phys. Chem. Chem. Phys. *18*, 22540–22547.

139. Kwon, O., Hirayama, M., Suzuki, K., Kato, Y., Saito, T., Yonemura, M., Kamiyama, T., and Kanno, R. (2015). Synthesis, structure, and conduction mechanism of the lithium superionic conductor $Li_{10+\delta}Ge_{1+\delta}P_{2-\delta}S_{12}$. J. Mater. Chem. A *3*, 438–446.

140. Sakuda, A., Hayashi, A., and Tatsumisago, M. (2013). Sulfide solid electrolyte with favorable mechanical property for all-solid-state lithium battery. Sci. Rep. *3*, 2261.

141. Dawson, J.A., Canepa, P., Famprikis, T., Masquelier, C., and Islam, M.S. (2018). Atomic-scale influence of grain boundaries on Li-ion conduction in solid electrolytes for all-solid-state batteries. J. Am. Chem. Soc. *140*, 362–368.

142. Monroe, C., and Newman, J. (2005). The impact of elastic deformation on deposition kinetics at lithium/polymer interfaces. J. Electrochem. Soc. *152*, A396.

143. Tang, H., Deng, Z., Lin, Z., Wang, Z., Chu, I.-H., Chen, C., Zhu, Z., Zheng, C., and Ong, S.P. (2018). Probing solid–solid interfacial reactions in all-solid-state sodium-ion batteries with first-principles calculations. Chem. Mater. *30*, 163–173.

144. Persson, K.. Department of Materials Science and Engineering, University of California at Berkeley. https://materialsproject.org/.

145. Zhu, Y., He, X., and Mo, Y. (2015). Origin of outstanding stability in the lithium solid electrolyte materials: insights from thermodynamic analyses based on first-principles calculations. ACS Appl. Mater. Interfaces *7*, 23685–23693.

146. Ma, C., Cheng, Y., Yin, K., Luo, J., Sharafi, A., Sakamoto, J., Li, J., More, K.L., Dudney, N.J., and Chi, M. (2016). Interfacial stability of Li metal–solid electrolyte elucidated via in situ electron microscopy. Nano Lett. *16*, 7030–7036.

147. Han, F., Yue, J., Chen, C., Zhao, N., Fan, X., Ma, Z., Gao, T., Wang, F., Guo, X., and Wang, C. (2018). Interphase engineering enabled all-ceramic lithium battery. Joule *2*, 497–508.

148. Sharafi, A., Meyer, H.M., Nanda, J., Wolfenstine, J., and Sakamoto, J. (2016). Characterizing the Li–$Li_7La_3Zr_2O_{12}$ interface stability and kinetics as a function of temperature and current density. J. Power Sources *302*, 135–139.

149. Sharafi, A., Yu, S., Naguib, M., Lee, M., Ma, C., Meyer, H.M., Nanda, J., Chi, M., Siegel, D.J., and Sakamoto, J. (2017). Impact of air exposure and surface chemistry on Li–$Li_7La_3Zr_2O_{12}$ interfacial resistance. J. Mater. Chem. A *5*, 13475–13487.

150. Naguib, M., Sharafi, A., Self, E.C., Meyer, H.M., Sakamoto, J., and Nanda, J. (2019). Interfacial reactions and performance of $Li_7La_3Zr_2O_{12}$-stabilized Li–sulfur hybrid cell. ACS Appl. Mater. Interfaces *11*, 42042–42048.

151. Awaka, J., Takashima, A., Kataoka, K., Kijima, N., Idemoto, Y., and Akimoto, J. (2011). Crystal structure of fast lithium-ion-conducting cubic $Li_7La_3Zr_2O_{12}$. Chem. Lett. *40*, 60–62.

152. Wang, D., Zhong, G., Pang, W.K., Guo, Z., Li, Y., McDonald, M.J., Fu, R., Mi, J.-X., and Yang, Y. (2015). Toward understanding the lithium transport mechanism in garnet-type solid electrolytes: Li^+ ion exchanges and their mobility at octahedral/tetrahedral sites. Chem. Mater. *27*, 6650–6659.

153. Bernstein, N., Johannes, M.D., and Hoang, K. (2012). Origin of the structural phase transition in $Li_7La_3Zr_2O_{12}$. Phys. Rev. Lett. *109*, 205702.

154. Liu, C., Rui, K., Shen, C., Badding, M.E., Zhang, G., and Wen, Z. (2015). Reversible ion exchange and structural stability of garnet-type Nb-doped $Li_7La_3Zr_2O_{12}$ in water for applications in lithium batteries. J. Power Sources *282*, 286–293.

155. Thompson, T., Wolfenstine, J., Allen, J.L., Johannes, M., Huq, A., David, I.N., and Sakamoto, J. (2014). Tetragonal vs. cubic phase stability in Al – free Ta doped $Li_7La_3Zr_2O_{12}$ (LLZO). J. Mater. Chem. A *2*, 13431–13436.

156. Liu, X., Chen, Y., Hood, Z.D., Ma, C., Yu, S., Sharafi, A., Wang, H., An, K., Sakamoto, J., Siegel, D.J., and Cheng, Y. (2019). Elucidating the mobility of H+ and Li+ ions in (Li6.25−x HxAl0.25) La3Zr2O12 via correlative neutron and electron spectroscopy. Energy Environ. Sci. *12*, 945–951.

157. Huo, H., Luo, J., Thangadurai, V., Guo, X., Nan, C.-W., and Sun, X. (2020). Li_2CO_3 : a critical issue for developing solid garnet batteries. ACS Energy Lett. *5*, 252–262.

158. Cheng, D., Wynn, T.A., Wang, X., Wang, S., Zhang, M., Shimizu, R., Bai, S., Nguyen, H., Fang, C., Kim, M., et al. (2020). Unveiling the stable nature of the solid electrolyte interphase between lithium metal and LiPON via cryogenic electron microscopy. Joule *4*, 2484–2500.

159. Sharafi, A., Kazyak, E., Davis, A.L., Yu, S., Thompson, T., Siegel, D.J., Dasgupta, N.P., and Sakamoto, J. (2017). Surface chemistry mechanism of ultra-low interfacial resistance in the solid-state electrolyte $Li_7La_3Zr_2O_{12}$. Chem. Mater. *29*, 7961–7968.

160. Gupta, A., and Sakamoto, J. (2019). Controlling ionic transport through the PEO-LiTFSI/LLZTO interface. Electrochem. Soc. Interface *28*, 63–69.

161. Zhu, Y., Connell, J.G., Tepavcevic, S., Zapol, P., Garcia-Mendez, R., Taylor, N.J., Sakamoto, J., Ingram, B.J., Curtiss, L.A., Freeland, J.W., and Fong, D.D. (2019). Dopant-dependent stability of garnet solid electrolyte interfaces with lithium metal. Adv. Energy Mater. *9*, 1803440.

162. Han, F., Zhu, Y., He, X., Mo, Y., and Wang, C. (2016). Electrochemical stability of $Li_{10}GeP_2S_{12}$ and $Li_7La_3Zr_2O_{12}$ solid electrolytes. Adv. Energy Mater. *6*, 1501590.

163. Cheng, E.J., Sharafi, A., and Sakamoto, J. (2017). Intergranular Li metal propagation through polycrystalline $Li_{6.25}Al_{0.25}La_3Zr_2O_{12}$ ceramic electrolyte. Electrochim. Acta *223*, 85–91.

164. Song, Y., Yang, L., Zhao, W., Wang, Z., Zhao, Y., Wang, Z., Zhao, Q., Liu, H., and Pan, F. (2019). Revealing the short-circuiting mechanism of garnet-based solid-state electrolyte. Adv. Energy Mater. *9*, 1900671.

165. Han, X., Gong, Y., Fu, K.K., He, X., Hitz, G.T., Dai, J., Pearse, A., Liu, B., Wang, H., Rubloff, G., et al. (2017). Negating interfacial impedance in garnet-based solid-state Li metal batteries. Nat. Mater. *16*, 572–579.

166. Wang, M.J., Choudhury, R., and Sakamoto, J. (2019). Characterizing the Li-solid-electrolyte interface dynamics as a function of stack pressure and current density. Joule *3*, 2165–2178.

167. Dixit, M.B., Zaman, W., Hortance, N., Vujic, S., Harkey, B., Shen, F., Tsai, W.-Y., De Andrade, V., Chen, X.C., Balke, N., and Hatzell, K.B. (2020). Nanoscale mapping of extrinsic interfaces in hybrid solid electrolytes. Joule *4*, 207–221.

168. Zhou, W., Wang, S., Li, Y., Xin, S., Manthiram, A., and Goodenough, J.B. (2016). Plating a dendrite-free lithium anode with a polymer/ceramic/polymer sandwich electrolyte. J. Am. Chem. Soc. *138*, 9385–9388.

169. Raj, R., and Wolfenstine, J. (2017). Current limit diagrams for dendrite formation in solid-state electrolytes for Li-ion batteries. J. Power Sources *343*, 119–126.

170. Yu, S., and Siegel, D.J. (2017). Grain boundary contributions to Li-ion transport in the solid electrolyte $Li_7La_3Zr_2O_{12}$ (LLZO). Chem. Mater. *29*, 9639–9647.

171. Cheng, L., Crumlin, E.J., Chen, W., Qiao, R., Hou, H., Franz Lux, S., Zorba, V., Russo, R., Kostecki, R., Liu, Z., et al. (2014). The origin of high electrolyte–electrode interfacial resistances in lithium cells containing garnet type solid electrolytes. Phys. Chem. Chem. Phys. *16*, 18294–18300.

172. Tian, H.-K., Liu, Z., Ji, Y., Chen, L.-Q., and Qi, Y. (2019). Interfacial electronic properties dictate Li dendrite growth in solid electrolytes. Chem. Mater. *31*, 7351–7359.

173. Cheng, Z., Liu, M., Ganapathy, S., Li, C., Li, Z., Zhang, X., He, P., Zhou, H., and Wagemaker, M. (2020). Revealing the impact of space-charge layers on the Li-ion transport in all-solid-state batteries. Joule *4*, 1311–1323.

174. Krauskopf, T., Dippel, R., Hartmann, H., Peppler, K., Mogwitz, B., Richter, F.H., Zeier, W.G., and Janek, J. (2019). Lithium-metal growth kinetics on LLZO garnet-type solid electrolytes. Joule *3*, 2030–2049.

175. Cheng, Q., Li, A., Li, N., Li, S., Zangiabadi, A., Li, T.-D., Huang, W., Li, A.C., Jin, T., Song, Q., et al. (2019). Stabilizing solid electrolyte-anode interface in Li-metal batteries by boron nitride-based nanocomposite coating. Joule *3*, 1510–1522.

176. Tian, H.-K., Xu, B., and Qi, Y. (2018). Computational study of lithium nucleation tendency in $Li_7La_3Zr_2O_{12}$ (LLZO) and rational design of interlayer materials to prevent lithium dendrites. J. Power Sources *392*, 79–86.

177. Le Van-Jodin, L., Ducroquet, F., Sabary, F., and Chevalier, I. (2013). Dielectric properties, conductivity and Li^+ ion motion in LiPON thin films. Solid State Ionics *253*, 151–156.

178. Ni, J.E., Case, E.D., Sakamoto, J.S., Rangasamy, E., and Wolfenstine, J.B. (2012). Room temperature elastic moduli and Vickers hardness of hot-pressed LLZO cubic garnet. J. Mater. Sci. *47*, 7978–7985.

179. Baranowski, L.L., Heveran, C.M., Ferguson, V.L., and Stoldt, C.R. (2016). Multi-scale mechanical behavior of the Li_3PS_4 solid-phase electrolyte. ACS Appl. Mater. Interfaces *8*, 29573–29579.

180. Kataoka, K., Nagata, H., and Akimoto, J. (2018). Lithium-ion conducting oxide single crystal as solid electrolyte for advanced lithium battery application. Sci. Rep. *8*, 9965.

181. Jin, Y., and McGinn, P.J. (2013). Bulk solid state rechargeable lithium ion battery fabrication with Al-doped $Li_7La_3Zr_2O_{12}$ electrolyte and $Cu_{0.1}V_2O_5$ cathode. Electrochim. Acta *89*, 407–412.

182. Xiao, Y., Miara, L.J., Wang, Y., and Ceder, G. (2019). Computational screening of cathode coatings for solid-state batteries. Joule *3*, 1252–1275.

183. Fu, K., Kelvin), Gong, Y., Liu, B., Zhu, Y., Xu, S., Yao, Y., Luo, W., Wang, C., Lacey, S.D., Dai, J., et al. (2017). Toward garnet electrolyte–based Li metal batteries: an ultrathin, highly effective, artificial solid-state electrolyte/metallic Li interface. Sci. Adv. *3*, e1601659.

184. Li, Y., Chen, X., Dolocan, A., Cui, Z., Xin, S., Xue, L., Xu, H., Park, K., and Goodenough, J.B. (2018). Garnet electrolyte with an ultralow interfacial resistance for Li-metal batteries. J. Am. Chem. Soc. *140*, 6448–6455.

185. Luo, W., Gong, Y., Zhu, Y., Li, Y., Yao, Y., Zhang, Y., Fu, K., Kelvin), Pastel, G., Lin, C., Mo, Y., et al. (2017). Reducing interfacial resistance between garnet-structured solid-state electrolyte and Li-metal anode by a germanium layer. Adv. Mater. *29*, 1606042.

186. Kotobuki, M., Munakata, H., Kanamura, K., Sato, Y., and Yoshida, T. (2010). Compatibility of $Li_7La_3Zr_2O_{12}$ solid electrolyte to all-solid-state battery using Li metal anode. J. Electrochem. Soc. *157*, A1076.

187. Vardar, G., Bowman, W.J., Lu, Q., Wang, J., Chater, R.J., Aguadero, A., Seibert, R., Terry, J., Hunt, A., Waluyo, I., et al. (2018). Structure, chemistry, and charge transfer resistance of the interface between $Li_7La_3Zr_2O_{12}$ electrolyte and $LiCoO_2$ cathode. Chem. Mater. *30*, 6259–6276.

188. Aurbach, D., Markovsky, B., Rodkin, A., Cojocaru, M., Levi, E., and Kim, H.-J. (2002). An analysis of rechargeable lithium-ion batteries after prolonged cycling. Electrochim. Acta *47*, 1899–1911.

189. Ohta, S., Kobayashi, T., Seki, J., and Asaoka, T. (2012). Electrochemical performance of an all-solid-state lithium ion battery with garnet-type oxide electrolyte. J. Power Sources *202*, 332–335.

190. Wang, M.J., Carmona, E., Gupta, A., Albertus, P., and Sakamoto, J. (2020). Enabling "lithium-free" manufacturing of pure lithium metal solid-state batteries through in situ plating. Nat. Commun. *11*, 5201.

191. Fu, K., Kelvin), Gong, Y., Hitz, G.T., McOwen, D.W., Li, Y., Xu, S., Wen, Y., Zhang, L., Wang, C., Pastel, G., et al. (2017). Three-dimensional bilayer garnet solid electrolyte based high energy density lithium metal–sulfur batteries. Energy Environ. Sci. *10*, 1568–1575.

192. Liu, B., Fu, K., Gong, Y., Yang, C., Yao, Y., Wang, Y., Wang, C., Kuang, Y., Pastel, G., Xie, H., et al. (2017). Rapid thermal annealing of cathode-garnet interface toward high-temperature solid state batteries. Nano Lett. *17*, 4917–4923.

193. Shao, Y., Wang, H., Gong, Z., Wang, D., Zheng, B., Zhu, J., Lu, Y., Hu, Y.-S., Guo, X., Li, H., et al. (2018). Drawing a soft interface: an effective interfacial modification strategy for garnet-type solid-state Li batteries. ACS Energy Lett. *3*, 1212–1218.

194. Huo, H., Chen, Y., Zhao, N., Lin, X., Luo, J., Yang, X., Liu, Y., Guo, X., and Sun, X. (2019). In-situ formed Li_2CO_3-free garnet/Li interface by rapid acid treatment for dendrite-free solid-state batteries. Nano Energy *61*, 119–125.

195. Gong, Y., Fu, K., Xu, S., Dai, J., Hamann, T.R., Zhang, L., Hitz, G.T., Fu, Z., Ma, Z., McOwen, D.W., et al. (2018). Lithium-ion conductive ceramic textile: a new architecture for flexible solid-state lithium metal batteries. Mater. Today *21*, 594–601.

196. Shen, F., Dixit, M.B., Xiao, X., and Hatzell, K.B. (2018). Effect of pore connectivity on Li dendrite propagation within LLZO electrolytes observed with synchrotron X-ray tomography. ACS Energy Lett. *3*, 1056–1061.

197. Yi, E., Shen, H., Heywood, S., Alvarado, J., Parkinson, D.Y., Chen, G., Sofie, S.W., and Doeff, M.M. (2020). All-solid-state batteries using rationally designed garnet electrolyte frameworks. ACS Appl. Energy Mater. *3*, 170–175.

198. Jiang, Z., Wang, S., Chen, X., Yang, W., Yao, X., Hu, X., Han, Q., and Wang, H. (2020). Tape-casting $Li_{0.34}La_{0.56}TiO_3$ ceramic electrolyte films permit high energy density of lithium-metal batteries. Adv. Mater. *32*, 1906221.

199. Feng, X., Chien, P.-H., Wang, Y., Patel, S., Wang, P., Liu, H., Immediato-Scuotto, M., and Hu, Y.-Y. (2020). Enhanced ion conduction by enforcing structural disorder in Li-deficient argyrodites $Li_{6-x}PS_{5-x}Cl_{1+x}$. Energy Storage Mater. *30*, 67–73.

200. Adeli, P., Bazak, J.D., Park, K.-H., Kochetkov, I., Huq, A., Goward, G., and Nazar, L. (2019). Boosting solid-state diffusivity and conductivity in lithium superionic argyrodites by halide substitution. Angew. Chem. Int. Ed. *131*, 8773.

201. Kraft, M.A., Ohno, S., Zinkevich, T., Koerver, R., Culver, S.P., Fuchs, T., Senyshyn, A., Indris, S., Morgan, B.J., and Zeier, W.G. (2018). Inducing high ionic conductivity in the lithium superionic argyrodites $Li_{6+x}P_{1-x}Ge_xS_5I$ for all-solid-state batteries. J. Am. Chem. Soc. *140*, 16330–16339.

202. Zhou, L., Assoud, A., Zhang, Q., Wu, X., and Nazar, L.F. (2019). New family of argyrodite thioantimonate lithium superionic conductors. J. Am. Chem. Soc. *141*, 19002–19013.

203. Patel, S.V., Banerjee, S., Liu, H., Wang, P., Chien, P.-H., Feng, X., Liu, J., Ong, S.P., and Hu, Y.-Y. (2021). Tunable lithium-ion transport in mixed-halide argyrodites $Li_{6-x}PS_{5-x}ClBr_x$: an unusual compositional space. Chem. Mater. *33*, 1435–1443.

204. Deiseroth, H.-J., Maier, J., Weichert, K., Nickel, V., Kong, S.-T., and Reiner, C. (2011). Li_7PS_6 and Li_6PS_5X (X: Cl, Br, I): possible three-dimensional diffusion pathways for lithium ions and temperature dependence of the ionic conductivity by impedance measurements. Z. Anorg. Allg. Chem. *637*, 1287–1294.

205. Peng, L., Ren, H., Zhang, J., Chen, S., Yu, C., Miao, X., Zhang, Z., He, Z., Yu, M., Zhang, L., et al. (2021). $LiNbO_3$-coated $LiNi_{0.7}Co_{0.1}Mn_{0.2}O_2$ and chlorine-rich argyrodite enabling high-performance solid-state batteries under different temperatures. Energy Storage Mater. *43*, 53–61.

206. Kraft, M.A., Culver, S.P., Calderon, M., Böcher, F., Krauskopf, T., Senyshyn, A., Dietrich, C., Zevalkink, A., Janek, J., and Zeier, W.G. (2017). Influence of lattice polarizability on the ionic conductivity in the lithium superionic argyrodites Li_6PS_5X (X = Cl, Br, I). J. Am. Chem. Soc. *139*, 10909–10918.

207. Self, E.C., Hood, Z.D., Brahmbhatt, T., Delnick, F.M., Meyer, H.M., Yang, G., Rupp, J.L.M., and Nanda, J. (2020). Solvent-mediated synthesis of amorphous Li_3PS_4/polyethylene oxide composite solid electrolytes with high Li+ conductivity. Chem. Mater. *32*, 8789–8797.

208. Yu, C., Ganapathy, S., Hageman, J., van Eijck, L., van Eck, E.R.H., Zhang, L., Schwietert, T., Basak, S., Kelder, E.M., and Wagemaker, M. (2018). Facile synthesis toward the optimal structure-conductivity characteristics of the argyrodite Li_6PS_5Cl solid-state electrolyte. ACS Appl. Mater. Interfaces *10*, 33296–33306.

209. Bloembergen, N., Purcell, E.M., and Pound, R.V. (1948). Relaxation effects in nuclear magnetic resonance absorption. Phys. Rev. *73*, 679–712.

210. Doux, J., Nguyen, H., Tan, D.H.S., Banerjee, A., Wang, X., Wu, E.A., Jo, C., Yang, H., and Meng, Y.S. (2020). Stack pressure considerations for room-temperature all-solid-state lithium metal batteries. Adv. Energy Mater. *10*, 1903253.

211. Auvergniot, J., Cassel, A., Ledeuil, J.-B., Viallet, V., Seznec, V., and Dedryvère, R. (2017). Interface stability of argyrodite Li_6PS_5Cl toward $LiCoO_2$, $LiNi_{1/3}Co_{1/3}Mn_{1/3}O_2$, and $LiMn_2O_4$ in bulk all-solid-state batteries. Chem. Mater. *29*, 3883–3890.

212. Yu, C., Li, Y., Willans, M., Zhao, Y., Adair, K.R., Zhao, F., Li, W., Deng, S., Liang, J., Banis, M.N., et al. (2020). Superionic conductivity in lithium argyrodite solid-state electrolyte by controlled Cl-doping. Nano Energy *69*, 104396.

213. Yu, C., Ganapathy, S., de Klerk, N.J.J., Roslon, I., van Eck, E.R.H., Kentgens, A.P.M., and Wagemaker, M. (2016). Unravelling Li-ion transport from picoseconds to seconds: bulk versus interfaces in an argyrodite Li_6PS_5Cl–Li_2S all-solid-state Li-ion battery. J. Am. Chem. Soc. *138*, 11192–11201.

214. Ohno, S., Koerver, R., Dewald, G., Rosenbach, C., Titscher, P., Steckermeier, D., Kwade, A., Janek, J., and Zeier, W.G. (2019). Observation of chemomechanical failure and the influence of cutoff potentials in all-solid-state Li–S batteries. Chem. Mater. *31*, 2930–2940.

215. Zhao, F., Sun, Q., Yu, C., Zhang, S., Adair, K., Wang, S., Liu, Y., Zhao, Y., Liang, J., Wang, C., et al. (2020). Ultrastable anode interface achieved by fluorinating electrolytes for all-solid-state Li metal batteries. ACS Energy Lett. *5*, 1035–1043.

216. Xiao, W., Xu, H., Xuan, M., Wu, Z., Zhang, Y., Zhang, X., Zhang, S., Shen, Y., and Shao, G. (2021). Stable all-solid-state battery enabled with $Li_{6.25}PS_{5.25}Cl_{0.75}$ as fast ion-conducting electrolyte. J. Energy Chem. *53*, 147–154.

217. Wang, L., Xie, R., Chen, B., Yu, X., Ma, J., Li, C., Hu, Z., Sun, X., Xu, C., Dong, S., et al. (2020). In-situ visualization of the space-charge-layer effect on interfacial lithium-ion transport in all-solid-state batteries. Nat. Commun. *11*, 5889.

218. Kim, D.H., Lee, Y.-H., Song, Y.B., Kwak, H., Lee, S.-Y., and Jung, Y.S. (2020). Thin and flexible solid electrolyte membranes with ultrahigh thermal stability derived from solution-processable Li argyrodites for all-solid-state Li-ion batteries. ACS Energy Lett. *5*, 718–727.

219. Zhang, J., Zhong, H., Zheng, C., Xia, Y., Liang, C., Huang, H., Gan, Y., Tao, X., and Zhang, W. (2018). All-solid-state batteries with slurry coated $LiNi_{0.8}Co_{0.1}Mn_{0.1}O_2$ composite cathode and Li6PS5Cl electrolyte: effect of binder content. J. Power Sources *391*, 73–79.

220. Delnick, F.M., Yang, G., Self, E.C., Meyer, H.M., and Nanda, J. (2020). Investigation of complex intermediates in solvent-mediated synthesis of thiophosphate solid-state electrolytes. J. Phys. Chem. C *124*, 27396–27402.

221. Ates, T., Keller, M., Kulisch, J., Adermann, T., and Passerini, S. (2019). Development of an all-solid-state lithium battery by slurry-coating procedures using a sulfidic electrolyte. Energy Storage Mater. *17*, 204–210.

222. Kim, D.H., Oh, D.Y., Park, K.H., Choi, Y.E., Nam, Y.J., Lee, H.A., Lee, S.-M., and Jung, Y.S. (2017). Infiltration of solution-processable solid electrolytes into conventional Li-ion-battery electrodes for all-solid-state Li-ion batteries. Nano Lett. *17*, 3013–3020.

223. Yu, C., Ganapathy, S., Eck, E.R.H.V. van, Wang, H., Basak, S., Li, Z., and Wagemaker, M. (2017). Accessing the bottleneck in all-solid state batteries, lithium-ion transport over the solid-electrolyte-electrode interface. Nat. Commun. *8*, 1086.

224. Moon, C.K., Lee, H.-J., Park, K.H., Kwak, H., Heo, J.W., Choi, K., Yang, H., Kim, M.-S., Hong, S.-T., Lee, J.H., et al. (2018). Vacancy-driven Na^+ superionic conduction in new Ca-doped Na_3PS_4 for all-solid-state Na-ion batteries. ACS Energy Lett. *3*, 2504–2512.

225. Feng, X., Chien, P.-H., Zhu, Z., Chu, I.-H., Wang, P., Immediato-Scuotto, M., Arabzadeh, H., Ong, S.P., and Hu, Y.-Y. (2019). Studies of functional defects for fast Na-ion conduction in $Na_{3-y}PS_{4-x}Cl_x$ with a combined experimental and computational approach. Adv. Funct. Mater. *29*, 1807951.

226. Yu, Z., Shang, S.-L., Seo, J.-H., Wang, D., Luo, X., Huang, Q., Chen, S., Lu, J., Li, X., Liu, Z.-K., and Wang, D. (2017). Exceptionally high ionic conductivity in $Na_3P_{0.62}As_{0.38}S_4$ with improved moisture stability for solid-state sodium-ion batteries. Adv. Mater. *29*, 1605561.

227. Banerjee, A., Park, K.H., Heo, J.W., Nam, Y.J., Moon, C.K., Oh, S.M., Hong, S.-T., and Jung, Y.S. (2016). Na3SbS4: a solution processable sodium superionic conductor for all-solid-state sodium-ion batteries. Angew. Chem. Int. Ed. *55*, 9634–9638.

228. Hayashi, A., Noi, K., Sakuda, A., and Tatsumisago, M. (2012). Superionic glass-ceramic electrolytes for room-temperature rechargeable sodium batteries. Nat. Commun. *3*, 856.

229. Jalem, R., Hayashi, A., Tsuji, F., Sakuda, A., and Tateyama, Y. (2020). First-principles calculation study of Na^+ superionic conduction mechanism in W- and Mo-doped Na_3SbS_4 solid electrolytes. Chem. Mater. *32*, 8373–8381.

230. Lu, Y., Alonso, J.A., Yi, Q., Lu, L., Wang, Z.L., and Sun, C. (2019). A high-performance monolithic solid-state sodium battery with Ca^{2+} doped $Na_3Zr_2Si_2PO_{12}$ electrolyte. Adv. Energy Mater. *9*, 1901205.

231. Zhang, L., Zhang, D., Yang, K., Yan, X., Wang, L., Mi, J., Xu, B., and Li, Y. (2016). Vacancy-contained tetragonal Na_3SbS_4 superionic conductor. Adv. Sci. (Weinh) *3*, 1600089.

232. de Klerk, N.J.J., and Wagemaker, M. (2016). Diffusion mechanism of the sodium-ion solid electrolyte Na_3PS_4 and potential improvements of halogen doping. Chem. Mater. *28*, 3122–3130.

233. Tanibata, N., Noi, K., Hayashi, A., and Tatsumisago, M. (2014). Preparation and characterization of highly sodium ion conducting Na_3PS_4–Na_4SiS_4 solid electrolytes. RSC Adv. *4*, 17120–17123.

234. Zhu, Z., Chu, I.-H., Deng, Z., and Ong, S.P. (2015). Role of Na+ interstitials and dopants in enhancing the Na+ conductivity of the cubic Na_3PS_4 superionic conductor. Chem. Mater. *27*, 8318–8325.

235. Krauskopf, T., Culver, S.P., and Zeier, W.G. (2018). Local tetragonal structure of the cubic superionic conductor Na_3PS_4. Inorg. Chem. *57*, 4739–4744.

236. Zhang, D., Cao, X., Xu, D., Wang, N., Yu, C., Hu, W., Yan, X., Mi, J., Wen, B., Wang, L., and Zhang, L. (2018). Synthesis of cubic Na_3SbS_4 solid electrolyte with enhanced ion transport for all-solid-state sodium-ion batteries. Electrochim. Acta *259*, 100–109.

237. Wu, E.A., Kompella, C.S., Zhu, Z., Lee, J.Z., Lee, S.C., Chu, I.-H., Nguyen, H., Ong, S.P., Banerjee, A., and Meng, Y.S. (2018). New insights into the interphase between the Na metal anode and sulfide solid-state electrolytes: a joint experimental and computational study. ACS Appl. Mater. Interfaces *10*, 10076–10086.

238. Lu, Y., Li, L., Zhang, Q., Niu, Z., and Chen, J. (2018). Electrolyte and interface engineering for solid-state sodium batteries. Joule *2*, 1747–1770.

239. Tian, Y., Shi, T., Richards, W.D., Li, J., Kim, J.C., Bo, S.-H., and Ceder, G. (2017). Compatibility issues between electrodes and electrolytes in solid-state batteries. Energy Environ. Sci. *10*, 1150–1166.

240. Tian, Y., Sun, Y., Hannah, D.C., Xiao, Y., Liu, H., Chapman, K.W., Bo, S.-H., and Ceder, G. (2019). Reactivity-guided interface design in Na metal solid-state batteries. Joule *3*, 1037–1050.

241. Tanibata, N., Deguchi, M., Hayashi, A., and Tatsumisago, M. (2017). All-solid-state Na/S batteries with a Na_3PS_4 electrolyte operating at room temperature. Chem. Mater. *29*, 5232–5238.

242. Zhang, S., Zhao, Y., Zhao, F., Zhang, L., Wang, C., Li, X., Liang, J., Li, W., Sun, Q., Yu, C., et al. (2020). Gradiently sodiated Alucone as an interfacial stabilizing strategy for solid-state Na metal batteries. Adv. Funct. Mater. *30*, 2001118.

243. Zhang, Z., Cao, H., Yang, M., Yan, X., Yu, C., Liu, D., and Zhang, L. (2020). High performance room temperature all-solid-state Na-Se S battery with Na3SbS4–coated cathode via aqueous solution. J. Energy Chem. *48*, 250–258.

244. Xu, X., Li, Y., Cheng, J., Hou, G., Nie, X., Ai, Q., Dai, L., Feng, J., and Ci, L. (2020). Composite solid electrolyte of Na_3PS_4-PEO for all-solid-state SnS_2/Na batteries with excellent interfacial compatibility between electrolyte and Na metal. J. Energy Chem. *41*, 73–78.

245. Nguyen, H., Banerjee, A., Wang, X., Tan, D., Wu, E.A., Doux, J.-M., Stephens, R., Verbist, G., and Meng, Y.S. (2019). Single-step synthesis of highly conductive Na_3PS_4 solid electrolyte for sodium all solid-state batteries. J. Power Sources *435*, 126623.

246. Oh, J.A.S., He, L., Plewa, A., Morita, M., Zhao, Y., Sakamoto, T., Song, X., Zhai, W., Zeng, K., and Lu, L. (2019). Composite NASICON ($Na_3Zr_2Si_2PO_{12}$) solid-state electrolyte with enhanced Na+ ionic conductivity: effect of liquid phase sintering. ACS Appl. Mater. Interfaces *11*, 40125–40133.

247. Schmid, H., Dejonghe, L., and Cameron, C. (1982). Chemical stability of NASICON. Solid State Ionics *6*, 57–63.

248. Park, H., Jung, K., Nezafati, M., Kim, C.-S., and Kang, B. (2016). Sodium ion diffusion in Nasicon ($Na_3Zr_2Si_2PO_{12}$) solid electrolytes: effects of excess sodium. ACS Appl. Mater. Interfaces *8*, 27814–27824.

249. Deng, Y., Eames, C., Nguyen, L.H.B., Pecher, O., Griffith, K.J., Courty, M., Fleutot, B., Chotard, J.-N., Grey, C.P., Islam, M.S., et al. (2018). Crystal structures, local atomic environments, and ion diffusion mechanisms of scandium-substituted sodium superionic conductor (NASICON) solid electrolytes. Chem. Mater. *30*, 2618–2630.

250. Boilot, J.P., Collin, G., and Colomban, P.H. (1988). Ion conduction in the NASICON. J. Solid State Chem. *73*, 160–171.

251. Noguchi, Y., Kobayashi, E., Plashnitsa, L.S., Okada, S., and Yamaki, J. (2013). Fabrication and performances of all solid-state symmetric sodium battery based on NASICON-related compounds. Electrochim. Acta *101*, 59–65.

252. Samiee, M., Radhakrishnan, B., Rice, Z., Deng, Z., Meng, Y.S., Ong, S.P., and Luo, J. (2017). Divalent-doped $Na_3Zr_2Si_2PO_{12}$ natrium superionic conductor: improving the ionic conductivity via simultaneously optimizing the phase and chemistry of the primary and secondary phases. J. Power Sources *347*, 229–237.

253. Feng, X., Chien, P.-H., Patel, S., Wang, Y., and Hu, Y.-Y. (2020). Enhanced ion conduction in $Li_{2.5}Zn_{0.25}PS_4$ via anion doping. Chem. Mater. *32*, 3036–3042.

254. Lacivita, V., Wang, Y., Bo, S.-H., and Ceder, G. (2019). *Ab initio* investigation of the stability of electrolyte/electrode interfaces in all-solid-state Na batteries. J. Mater. Chem. A *7*, 8144–8155.

255. Gao, H., Xin, S., Xue, L., and Goodenough, J.B. (2018). Stabilizing a high-energy-density rechargeable sodium battery with a solid electrolyte. Chem *4*, 833–844.

256. Zhou, W., Li, Y., Xin, S., and Goodenough, J.B. (2017). Rechargeable sodium all-solid-state battery. ACS Cent. Sci. *3*, 52–57.

257. Yu, X., Xue, L., Goodenough, J.B., and Manthiram, A. (2019). A high-performance all-solid-state sodium battery with a poly(ethylene oxide)–$Na_3Zr_2Si_2PO_{12}$ composite electrolyte. ACS Materials Lett. *1*, 132–138.

258. Zhao, Y., Wang, C., Dai, Y., and Jin, H. (2021). Homogeneous Na+ transfer dynamic at Na/$Na_3Zr_2Si_2PO_{12}$ interface for all solid-state sodium metal batteries. Nano Energy *88*, 106293.

259. Wang, X., Liu, Z., Tang, Y., Chen, J., Wang, D., and Mao, Z. (2021). Low temperature and rapid microwave sintering of $Na_3Zr_2Si_2PO_{12}$ solid electrolytes for Na-ion batteries. J. Power Sources *481*, 228924.

260. Yang, J., Liu, G., Avdeev, M., Wan, H., Han, F., Shen, L., Zou, Z., Shi, S., Hu, Y.-S., Wang, C., and Yao, X. (2020). Ultrastable all-solid-state sodium rechargeable batteries. ACS Energy Lett. *5*, 2835–2841.

261. Zuo, X., Chang, K., Zhao, J., Xie, Z., Tang, H., Li, B., and Chang, Z. (2016). Bubble-template-assisted synthesis of hollow fullerene-like MoS_2 nanocages as a lithium ion battery anode material. J. Mater. Chem. A *4*, 51–58.

262. Evstigneeva, M.A., Nalbandyan, V.B., Petrenko, A.A., Medvedev, B.S., and Kataev, A.A. (2011). A new family of fast sodium ion conductors: $Na_2M_2TeO_6$ (M = Ni, Co, Zn, Mg). Chem. Mater. *23*, 1174–1181.

263. Feng, T., Li, L., Lv, Z., Li, B., Zhang, Y., and Li, G. (2019). Temperature-dependent electrical transport behavior and structural evolution in hollandite-type titanium-based oxide. J. Am. Ceram. Soc. *102*, 6741–6750.

264. Udovic, T.J., Matsuo, M., Tang, W.S., Wu, H., Stavila, V., Soloninin, A.V., Skoryunov, R.V., Babanova, O.A., Skripov, A.V., Rush, J.J., et al. (2014). Exceptional Superionic Conductivity in Disordered Sodium decahydro- *closo* -decaborate. Adv. Mater. *26*, 7622–7626.

265. Choi, B.-K. (2019). Ionic conductivities and melting transition studies of $NaBH_4$, KBH_4, and their mixtures. ASCT *28*, 169–172.

266. Duchêne, L., Kühnel, R.-S., Rentsch, D., Remhof, A., Hagemann, H., and Battaglia, C. (2017). A highly stable sodium solid-state electrolyte based on a dodeca/deca-borate equimolar mixture. Chem. Commun. (Camb.) *53*, 4195–4198.

267. Andersen, N., Bandaranayake, P., Careem, M., Dissanayake, M., Wijayasekera, C., Kaber, R., Lunden, A., Mellander, B., Nilsson, L., and Thomas, J. (1992). Paddle-wheel versus percolation mechanism for cation transport in some sulphate phases. Solid State Ionics *57*, 203–209.

268. Zhong, Y., Shi, Q., Zhu, C., Zhang, Y., Li, M., Francisco, J.S., and Wang, H. (2021). Mechanistic insights into fast charging and discharging of the sodium metal battery anode: a comparison with lithium. J. Am. Chem. Soc. *143*, 13929–13936.

269. Chen, R., Nolan, A.M., Lu, J., Wang, J., Yu, X., Mo, Y., Chen, L., Huang, X., and Li, H. (2020). The thermal stability of lithium solid electrolytes with metallic lithium. Joule *4*, 812–821.

270. Weiss, M., Simon, F.J., Busche, M.R., Nakamura, T., Schröder, D., Richter, F.H., and Janek, J. (2020). From liquid- to solid-state batteries: ion transfer kinetics of heteroionic interfaces. Electrochem. Energ. Rev. *3*, 221–238.